ABSTRACT

| | |
|---|---|
| Title of Dissertation: | LATTICE MODIFICATIONS OF SOLID STATE ELECTROLYTES FOR THE OPTIMIZATION OF ION TRANSPORT |
| | Adam Garrett Jolley, Doctor of Philosophy, 2018 |
| Dissertation directed by: | Professor, Eric D. Wachsman, Materials Science and Engineering |

A solid state electrolyte is one of the primary components of both a solid oxide fuel cells (SOFC) and an all-solid-state sodium battery. In both cases, the ionic conductivity of the electrolyte has a major impact on the performance of the electrochemical cell. For SOFCs, the conductivity of traditional electrolytes is not high enough for sufficient performance at intermediate and low temperature operation. Therefore, novel bismuth oxide compositions were developed to achieve higher conductivity. The conductivity of $Bi_2O_3$ was improved by reducing the total dopant concentration required to stabilize the highly conductive cubic phase. This strategy lead to the development of a $Bi_2O_3$ electrolyte (La7Zr3) with the highest oxygen ion conductivity to date. Unfortunately, at temperatures below 600°C the conductivity of the cubic phase was unstable. Therefore, rhombohedral bismuth oxide was investigated for low temperature SOFC operation due to its stability. For the first time, a dopant concentration less than 10% was used to stabilize the rhombohedral phase of $Bi_2O_3$. Furthermore, a novel phase

diagram was constructed for the low dopant regime of the rhombohedral phase. Ultimately, the double doped bismuth oxide material (La5.1Y1.4) developed here was among the highest and most stable oxygen ion conductors below 600°C. Performance of an SOFC with a La5.1Y1.4 electrolyte verified that it is a promising material for low temperature SOFCs. A similar strategy of doping an electrolyte material to increase ionic conductivity was carried out on NASICON ($Na_3Zr_2Si_2PO_{12}$). NASICON is a promising electrolyte for room temperature sodium batteries, but traditionally it does not exhibit high enough conductivity to garner high performance. For the first time, the mechanism driving the phase transition in NASICON was determined and mapped out. Mitigation of the phase transition in the material was established to lower the activation energy barrier for sodium ion transport. Additionally, divalent cations were substituted into the NASICON lattice to generate an increase in sodium ion conductivity. Ultimately the phase and dopant concentration was optimized to deliver a material that is among the best sodium ion conducting ceramics to date (20% Zn-doped NASICON).

# LATTICE MODIFICATIONS ON SOLID STATE ELECTROLYTES FOR THE OPTIMIZATION OF ION TRANSPORT

by

Adam Garrett Jolley

Dissertation submitted to the Faculty of the Graduate School of the
University of Maryland, College Park, in partial fulfillment
of the requirements for the degree of
Doctor of Philosophy
2018

Advisory Committee:
Professor Eric D. Wachsman, Chair
Professor Liangbing Hu
Professor Bryan Eichhorn
Professor Isabel K. Lloyd
Professor Yifei Mo

# Acknowledgements

First, I would like to thank my advisor Dr. Eric Wachsman for all his guidance, knowledge and support. You have helped me enjoy my time as a graduate student and succeed in a research environment.

Next, I would to thank all the members of the Wachsman lab for the comradery and intellectual discussions they provided. The members of the lab really made me feel at home and have a great time in the graduate program. Specifically, I would like to thank Dr. Mohammed Hussain for his help constructing and testing a full SOFC, as well as his general SOFC expertise. Ian Robinson for his help with SEM imaging. Tom Hays for his general advice and know how. Chris Pellegrinelli for his help with all electronic things in the lab, as well as his assistance on ionic transference number measurement and calculations. Yi-Lin Huang for his knowledge of composite cathodes and synthesis abilities. Finally, Greg Hitz for originally bringing me up to speed in the lab and helping me make sense of the NASICON materials.

I want to acknowledge Dr. Peter Zavalij for his expertise in X-ray diffraction, as well as Dan Taylor and Rishvi Jayathilake for their help in obtaining and fitting X-ray diffraction patterns.

Also, I would like to acknowledge all my financial support. The US Department of Energy's Office of Electricity Delivery & Energy Reliability and Sandia National Laboratories, contract # 1161548. Also, Redox Power Systems and funding from the U.S. Department of Energy, Advanced Research Projects Agency - Energy (ARPA-E) contract number DE-AR0000494

Finally, I would also like to thank my friends and family, for their love and support. Without you I would not be where I am today.

# Table of Contents

# List of Tables

# List of Figures

# List of Abbreviations

| | |
|---|---|
| AC | alternating current |
| AFL | anode functional layer |
| ASL | anode support layer |
| ASR | area specific resistance |
| BBP | butyl benzyl phthalate |
| BCC | body centered cubic |
| DSC | differential scanning calorimetry |
| DWSB | 8% Dy-doped 4% Dy-doped $Bi_2O_3$ |
| EIS | Electrochemical Impedance Spectroscopy |
| ESB | 20% Er-doped $Bi_2O_3$ |
| FCC | face centered cubic |
| FRA | frequency response analyzer |
| GDC | 10% Gd-doped Ceria |
| LSM | $La_{0.8}Sr_{0.2}MnO_3$ |
| MD | molecular dynamics |
| OCP | open circuit potential |
| OCV | open circuit voltage |
| PVB | polyvinyl butyral |
| SCCM | standard cubic centimeters per second |
| SEM | scanning electron microscope |
| SOFC | solid oxide fuel cell |
| $T_c$ | critical temperature |
| TZP | tetragonal polycrystalline zirconia |
| WDS | wavelength-dispersive spectroscopy |
| YSZ | yttria stabilized zirconia |
| XRD | X-ray diffraction |

# Chapter 1: Introduction

## *1.1 General Electrochemistry Introduction*

While there is still a dependence on fossil fuels for global energy requirements, a shift in recent years has increased the demand for alternative energy sources. With this transition, electrochemical devices have carved out a vital role in the changing energy landscape. In particular, rechargeable batteries have become a viable option for grid-scale storage and this promotes the practicality of both wind and solar energy. Additionally, solid oxide fuel cells (SOFCs) present a path toward clean hydrogen energy, while still retaining functionality with traditional fossil fuels such as natural gas. Advances in SOFC and battery technology will be very significant as the energy landscape continues to evolve and grow.

Even though different mechanisms drive the operation of batteries and SOFCs, there are key fundamentals between the two electrochemical devices that are the same. The oxidation reaction occurs at the anode and provides electrons for the external circuit, ions travel across the electron blocking electrolyte between electrodes, and the electrons reconvene at the cathode where the reduction reaction occurs. An SOFC operates fundamentally different than a battery because it does not act as an energy storage device, but rather converts incoming fuel directly into electrical power. Also for an SOFC to function it must operate at high temperatures, whereas many batteries operate at room temperature. The other key difference between the two electrochemical devices is that gaseous fuel is used to generate power in an SOFC, while a battery relies

on the oxidation of a self-contained anode to provide electoral output. Ultimately both the cathode and anode of an SOFC must have the ability to catalyze an incoming gas into its component ions and oxygen ions are conducted through the solid electrolyte to balance the electrons traveling through the external circuit. Battery electrodes however, provide all of the power within the packaging and don't need to rely on gas catalysis or incoming fuel. Furthermore, there are a host of battery chemistries and designs that prevail, as well as both liquid and solid electrolytes.

## *1.2 Fundamentals of Solid Oxide Fuel Cells*

SOFCs are a promising technology that provide high energy density and a low overall environmental impact[16–18]. Furthermore high temperature SOFCs provide higher operating efficiencies than combustion engines[19,20]. A solid oxide fuel cell is comprised of three main components. The anode catalyzes the incoming hydrogen gas and the oxidation reaction involves the formation of water and release of electrons as described in Eq. 1.2.1

$$H_2 + O^{-2} \rightarrow H_2O + 2e' \quad \text{(Eq. 1.2.1)}$$

The cathode is the site of oxygen reduction and is described by Eq. 1.2.2

$$\tfrac{1}{2}\, O_2 + 2e' \rightarrow O^{-2} \quad \text{(Eq. 1.2.2)}$$

The last main component of a solid oxide fuel cells is the electrolyte. The electrolyte transports the oxygen ions from the cathode to the anode where they combine with hydrogen to form water. Electrons flow from anode to cathode along an external circuit. The whole cell can be described by Eq. 1.2.3

$$H_2 + \tfrac{1}{2}\, O_2 \rightarrow H_2O \quad \text{(Eq. 1.2.3)}$$

The diagram detailing a working SOFC is illustrated in **Fig. 1.2.1**.

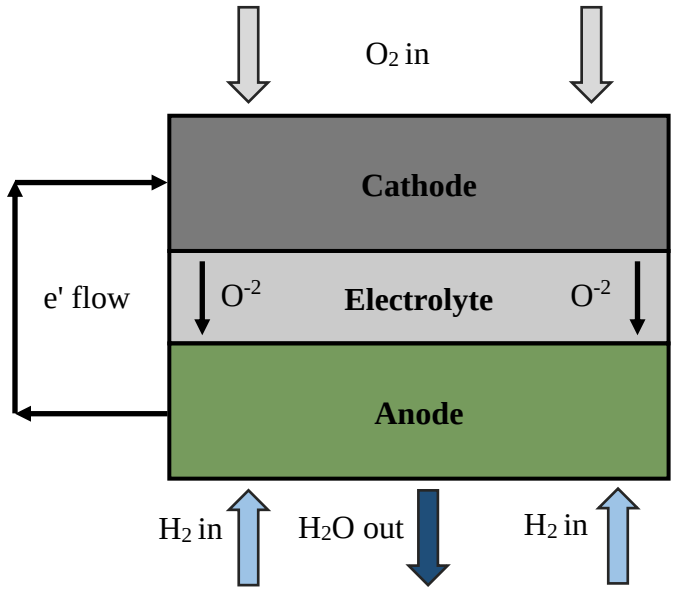


**Fig. 1.2.1**. Diagram detailing the operation of a solid oxide fuel cell with gas and components labeled.

The fundamental performance of a solid oxide fuel cell is also dependent on the open circuit voltage (OCV) achieved by the cell. The maximum theoretical OCV is determined by the Nernst equation, which is expressed in Eq. 1.2.4

$$E = E° - \frac{RT}{2F} \ln\left(\frac{(P_{H_2O})}{(P_{H_2}) \bullet (P_{O_2})^{\frac{1}{2}}}\right) \qquad \text{(Eq. 1.2.4)}$$

E° is the standard cell potential, R is the gas constant, T is the temperature, F is faradays constant, $P_{H_2O}$ is the partial pressure of water vapor on the anode side, $P_{H_2}$ is the partial pressure of hydrogen on the anode side, and $P_{O_2}$ is the partial pressure of oxygen on the cathode side. Although it is possible to reach the theoretical voltage when the cell is not operating under a load, the actual performance of the cell is dictated by polarization losses. The three main overpotential losses are defined as activation polarization, ohmic

polarization and concentration polarization. Activation polarization is related to the electrode response and is a result of decreased charge transfer. Ohmic polarization is mainly caused by resistive loses in the electrolyte layer, but is also caused by contact resistance and resistances in the electrodes. Finally, concentration polarization is related to a reduced transport of gaseous elements through the porous electrodes. Overall the actual voltage of an operating cell is detailed in Eq. 1.2.5.

$$V = V_o - \eta_{activation} - \eta_{ohmic} - \eta_{concentration} \quad \text{(Eq. 1.2.5)}$$

$V_o$ is the theoretical voltage, $\eta_{activation}$ is the activation polarization, $\eta_{ohmic}$ is the ohmic polarization, and $\eta_{concentration}$ is the concentration polarization.

While SOFCs are a promising technology, there are still issues with the system that hold it back from being a mainstream energy conversion device. One of the main limitations associated with traditional SOFCs is the high temperature of operation. Lowering the operation temperature to approximately 600°C would help reduce costs and improve overall efficiency[10,21]. Ceramic interconnects and insulation is needed for elevated temperatures, which greatly increases the cost over interconnects made of stainless steel[18,22]. Decreasing the operating temperature of solid oxide fuels hinges on electrolyte materials with higher conductivity. Yttria stabilized zirconia (YSZ) is a traditional electrolyte material that does not provide high enough ionic conductivity at intermediate temperature to allow for high performance in SOFC[23–25]. It is possible to reduce the thickness of the YSZ layer, but processing temperatures and lower economy of scale manufacturing techniques are required. Ultimately electrolyte materials with higher ionic conductivity are necessary for lowering the operating temperature of SOFCs.

*1.3 Bismuth Oxide as an SOFC Electrolyte*

At elevated temperatures, $Bi_2O_3$ exhibits the highest known oxygen ion conductivity of any material[3,26]. From approximately 730°C up to its melting point, bismuth oxide exists in the δ-cubic phase. The δ-cubic phase of $Bi_2O_3$ has a defect fluorite structure with 25% of its oxygen sites are vacant. The unit cell of δ-cubic $Bi_2O_3$ is face centered cubic (FCC) with cations at the FCC sites and anions at the tetrahedral positions. The intrinsic vacancies of the material, the loose bonding of bismuth with oxygen, and the overall disorder of the structure allows for high oxygen ion mobility. Below 730°C pure $Bi_2O_3$ exists as the monoclinic α-phase. Cooling the δ-cubic $Bi_2O_3$ below 730°C can cause a transition to the metastable tetragonal β-phase or body centered cubic (BCC) γ-phase. The monoclinic phase, tetragonal phase, and BCC phase all have much lower conductivity than the δ-cubic phase of $Bi_2O_3$ as illustrated in **Fig. 1.3.1a**. The δ-cubic lattice is presented in **Fig. 1.3.1b**.

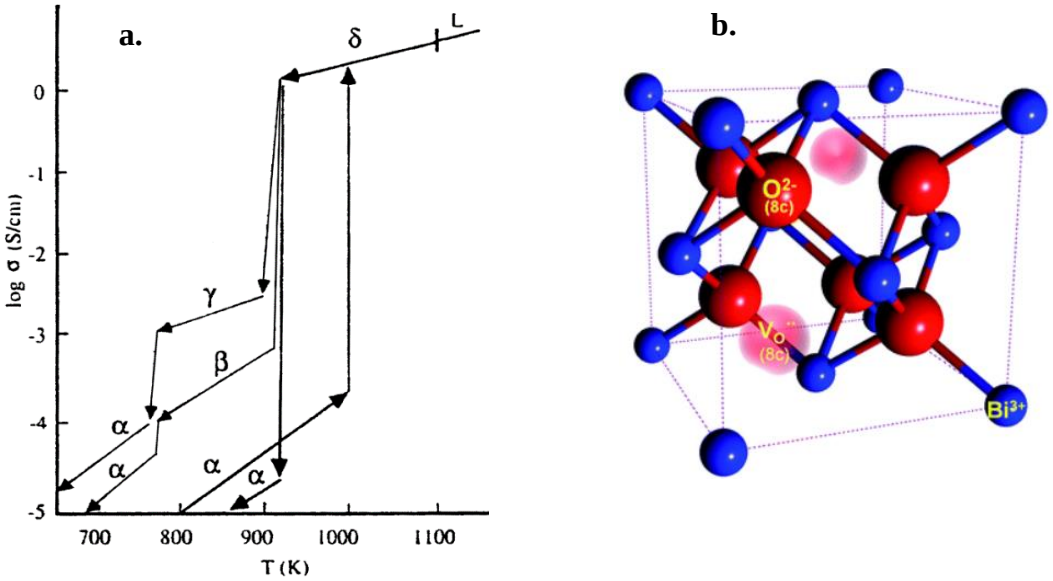


**Fig 1.3.1 a**. Phase diagram and conductivity of pure $Bi_2O_3$ as a function of temperature. Fig. is taken from[3]. **b**. The δ-cubic $Bi_2O_3$ lattice with the cations, anions, and vacancies labeled on the diagram. Fig is taken from[4].

Although δ-cubic $Bi_2O_3$ exhibits exceptional conductivity at elevated temperature, the transition to lower symmetry phases makes pure bismuth oxide unsuitable for use as a solid electrolyte. The conductivity of the monoclinic, tetragonal, and BCC phase of bismuth oxide is too low to achieve high performance in an SOFC. Thus stabilizing the highly conductive δ-cubic $Bi_2O_3$ to lower temperatures has been a priority for many researchers. It has been found that doping the bismuth oxide lattice with a sufficient amount of lanthanide cations actually preserves the cubic phase down to room temperature[5,6,27]. Ultimately it was found that the highest conductivity of doped bismuth oxide corresponded to the minimum required cation substitution for stabilizing the highly conductive FCC phase. The relationship between minimum required doping and the conductivity of doped bismuth oxide is presented in **Fig 1.3.2 a**. and **b**.

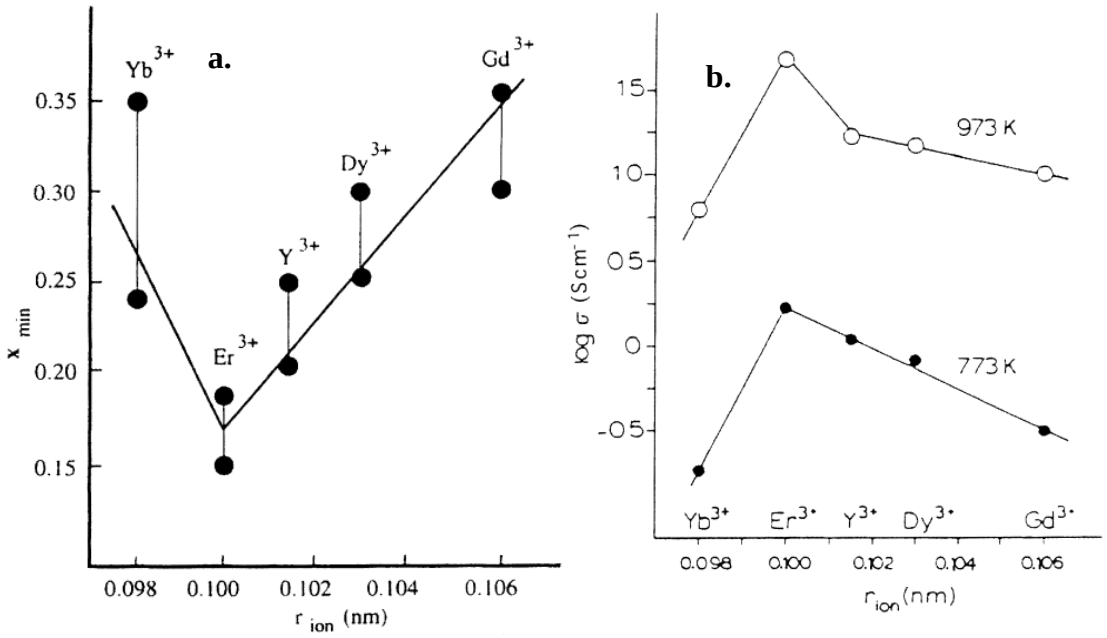


**Fig 1.3.2 a**. Minimum dopant required to stabilize the FCC phase of $Bi_2O_3$ vs. the ionic radius of the dopant. Fig. is taken from[5]. **b**. Conductivity of cubic $Bi_2O_3$ as a function of dopant and ionic radius. Fig. is taken from[6].

Overall $Er^{+3}$ provided the minimum necessary dopant concentration at 20% to stabilize the cubic phase of $Bi_2O_3$, and consequently exhibited the highest conductivity. As the dopant ionic radius diverged from approximately 1 Å, the amount of cation substitution required to stabilize the cubic phase increased. Furthermore, as the amount of dopant concentration increased the resulting conductivity of the bismuth oxide material decreased. Ultimately a reduction in the dopant concentration in bismuth oxide leads to less defect association within the lattice as well as a higher lattice polarizability, ultimately generating higher oxygen ion mobility.

While 20% Er-doped $Bi_2O_3$ (ESB) exhibited the highest conductivity of singly doped bismuth oxide, recent strategies have been employed to increase the conductivity even further. It has been found that doping the $Bi_2O_3$ lattice with two different cations provides a synergistic effect that allows for a lower overall dopant concentration to effectively stabilize the cubic phase[8,28]. By incorporating two different dopants into the lattice, the entropy of the system increases due to an increase in entropy from mixing. Wachsman et al. successfully stabilized the cubic phase of bismuth oxide with a total of 12% cation substitution, thereby creating a material with the highest oxygen ion conductivity to date[8,28]. The highly conductive material, 8% Dy-doped and 4% W-doped $Bi_2O_3$ (DWSB), is shown on an Arrhenius plot versus other electrolyte materials in **Fig. 1.3.3**. The higher conductivity of double doped DWSB over singly doped ESB is an outcome of the decreased amount of dopant. Overall, reducing the cation substitution in $Bi_2O_3$ will bring the lattice closer to the pure δ-cubic phase and improve the ionic conductivity.

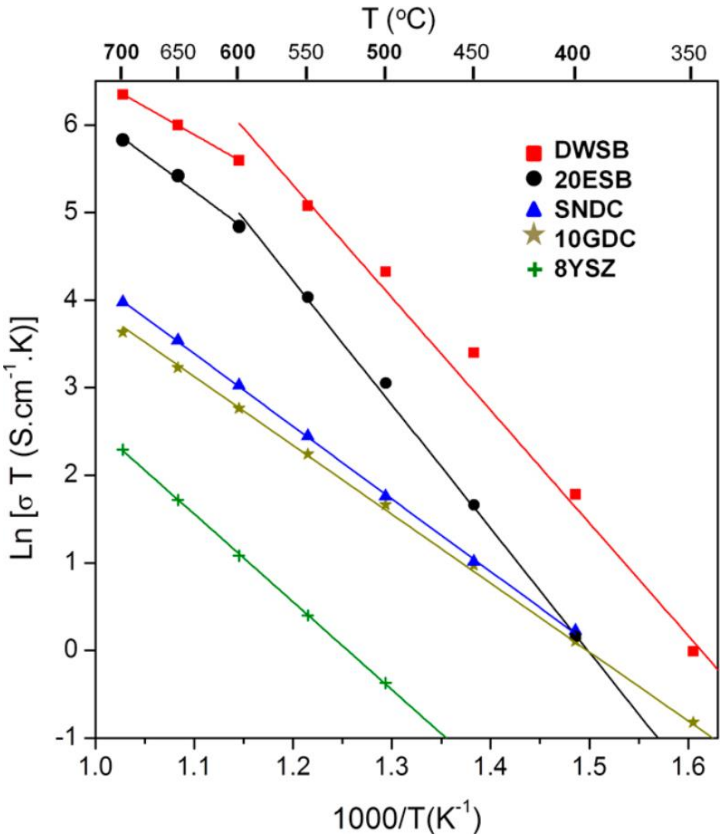


**Fig. 1.3.3**. Arrhenius plot of multiple oxygen ion conducting electrolytes. Fig. is taken from[20].

While the FCC cubic phase can be stabilized and conductivity maximized in both single doped and double doped bismuth oxide systems, there is still issues with these materials at intermediate temperatures. When aged below approximately 600°C the cubic bismuth oxide undergoes a process of conductivity degradation. The degradation is general caused by two separate mechanisms. One cause of conductivity decay in cubic Bi2O3 is a result of a phase transition from the cubic phase to the rhombohedral phase. It has been observed that yttria stabilized δ-cubic Bi2O3 as well as other rare earth stabilized Bi2O2 undergo a phase transformation to the rhombohedral phase when annealed for a period of time below 700°C[29,30]. The transformation from the highly conductive δ-cubic phase to the rhombohedral phase

results in a drop in conductivity. Therefore, some compositions of cubic bismuth oxide are only metastable below approximately 700°C.

Another cause of conductivity degradation in δ-cubic phase of Bi2O3 below approximately 600°C is an ordering phenomenon in the oxygen ion sublattice. Many methods of characterization, including X-ray diffraction (XRD) and neutron diffraction have indicated that there is long range ordering of the oxygen vacancies[1,31,32]. In particular the oxygen vacancies align along the <111> direction with a displacement of the oxygen ions from the normal 8c position to the 32f sites. This long-range ordering of the oxygen vacancies causes a large drop in conductivity as a result of fewer jump directions for the oxygen ions. **Table 1.3.1** describes the difference between oxygen ions in the ordered and disordered cubic Bi2O3 structure in terms of the pre-exponential factor in the conductivity equation.

| **Pre-exponential Factor Contributions** | **Disordered $Bi_2O_3$** | **Ordered $Bi_2O_3$** |
|---|---|---|
| n | 6 | 1 |
| ze | 1.5e | 2e |
| $c_i$ | 1 | 0.33 |

**Table 1.3.1**. Key pre-exponential factor contributions for the temperature dependence of conductivity on disordered and ordered cubic $Bi_2O_3$. Table Adapted from[1].

The number of equivalent jump directions (n) is much less for the ordered structure than the disordered structure, which greatly reduces the contribution of pre-exponential factor in the conductivity equation. The equation governing the pre-exponential factor is detailed in Eq. 1.3.1

$$A = n\lambda^2 (ze)^2 \frac{vc_i}{6vk} \quad \text{(Eq. 1.3.1)}$$

For this equation, n is equivalent jump directions for mobility, λ is jump distance, ze is effective charge of the charge carrier, $c_i$ is concentration of charge carriers, and v is the volume of the unit cell. The pre-exponential factor fits into the temperature dependent conductivity equation as expressed in Eq. 1.3.2

$$\sigma T = A \exp\left(-\frac{E_A}{kT}\right) \quad \text{(Eq.1.3.2)}$$

For this equation, σ is conductivity, T is temperature, A is the pre-exponential factor, $E_a$ is activation energy, and k is the Boltzmann constant.

Although the ordering phenomena can result in over an order of magnitude of conductivity degradation in the cubic bismuth oxide system, there have been techniques for decreasing the degree of degradation. For example, increasing the dopant concentration in bismuth oxide improves the stability of conductivity. The ordering phenomena that is responsible for the degradation is suppressed in higher dopant regimes. **Fig. 1.3.4** illustrates the aging properties of a range of bismuth oxide samples at 500°C. From the figure it is clear that the Bi2O3 sample with greater substitution displayed less overall degradation. The sample with 21% cation substitution (14D7WSB) had approximately an order of magnitude decrease in conductivity while the 12% cation substitution sample (8W4WSB) underwent a decay of almost two orders of magnitude. While increasing the dopant concentration suppresses the conductivity decay, it ultimately drops the overall conductivity. The benefit of δ-cubic Bi2O3 is the superior conductivity to other materials, and thus maintaining high conductivity should be paramount.

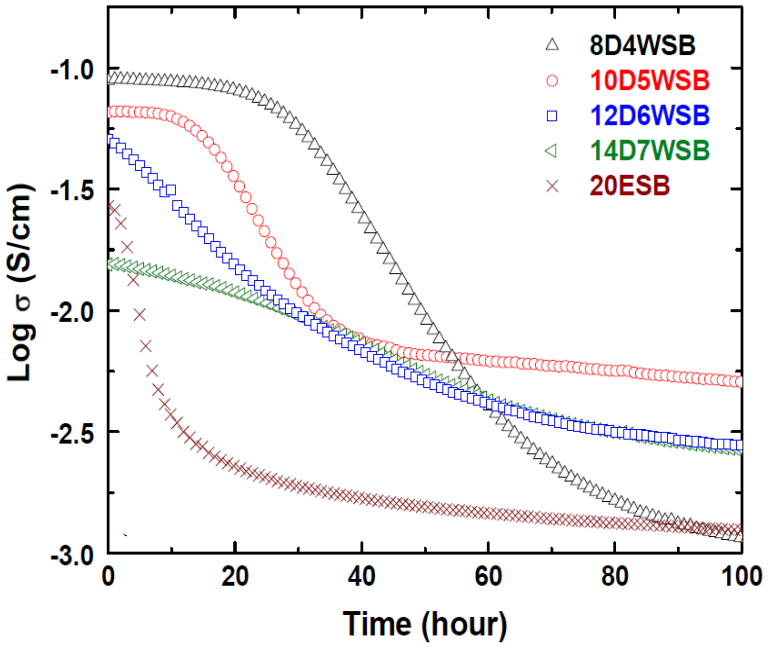


**Fig. 1.3.4**. Conductivity as a function of time for multiple bismuth oxide samples at 500°C. The number represents the amount of cation substitution where D is Dysprosium, W is tungsten, and E is erbium. Fig. is taken from[8].

As discussed earlier, the tetragonal phase, BCC, and monoclinic phase are all natural polymorphs of pure bismuth oxide that exhibit much lower conductivity than the FCC cubic phase. The rhombohedral phase was not presented in this list because only doped bismuth oxide forms this phase. In general, there has not been extensive research into the rhombohedral phase. The lack of investigation into rhombohedral Bi2O3 is most likely as a result of its lower conductivity when compared to the cubic phase. Comparatively the rhombohedral phase is about ten times less conductive than the δ-cubic phase of bismuth oxide[5]. **Fig. 1.3.5** illustrates the higher conductivity of the cubic phase compared to the rhombohedral phase for the same sample.

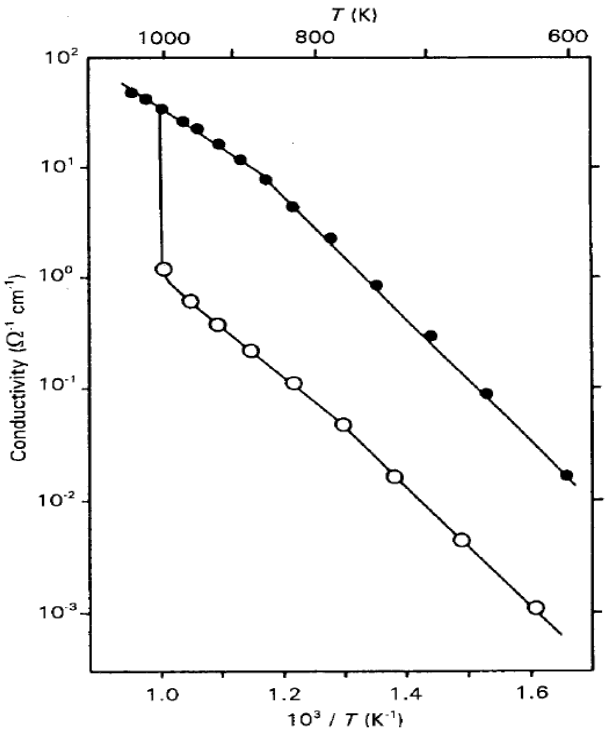


**Fig. 1.3.5**. Conductivity vs temperature for 25% Dy-doped $Bi_2O_3$. The cubic phase is represented by the closed circles and the rhombohedral phase is the open circles. Fig. taken from[5].

Besides having a distinct lattice, the rhombohedral phase is also different from the cubic phase in how it is produced. In general, the rhombohedral phase of bismuth oxide is created by doping the $Bi_2O_3$ lattice with large trivalent cations such as Nd, and La, while the cubic phase is made by doping the lattice with smaller cations such Er and Y. The rhombohedral phase of $Bi_2O_3$ has been mapped out by previous authors, but has generally been limited to larger dopant radii[33–35]. Investigations into the lower dopant regime could improve the conductivity of rhombohedral bismuth oxide and make it viable electrolyte for SOFCs at intermediate temperatures.

Although the cubic phase has higher conductivity than other polymorphs of bismuth oxide, the conductivity of $Bi_2O_3$ decreases with increasing cation substitution. Since the cubic phase can only be stabilized by doping the bismuth site, it is important

to understand the role that the dopant plays on the conductivity. It has been shown that the polarizability of the substituted cation plays a major role in the conductivity and the stability of δ-cubic $Bi_2O_3$ material[1,36]. As the polarizability of the dopant cation increases, the time constant for the disorder-order transition also increases. This means that increasing the polarizability of the lattice promotes less degradation of conductivity in bismuth oxide materials. Furthermore, the polarizability of the $Bi_2O_3$ lattice effects the oxygen ion mobility. Using molecular-dynamics (MD) simulation, Aidhy et. al. demonstrated that oxygen ion diffusion is dramatically reduced in a non-polarizable system[9]. The effect of polarizability on the MD simulation of oxygen diffusion in $Bi_2O_3$ is shown in **Fig. 1.3.6**.

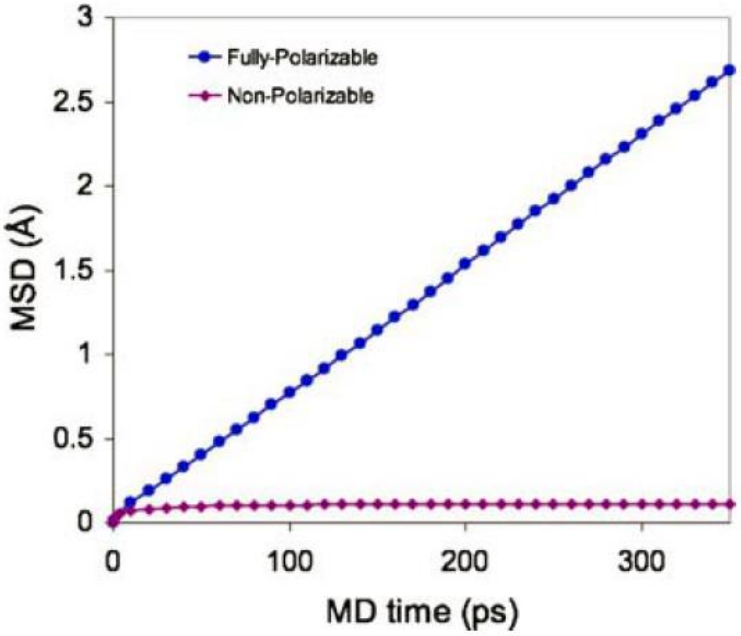


**Fig. 1.3.6**. Time dependence of mean-square displacement (MSD) of oxygen diffusion for both polarizable and non-polarizable δ-cubic $Bi_2O_3$ systems. Fig. taken from[9].

As illustrated by the figure, there is almost no oxygen diffusion in the bismuth oxide lattice when the $Bi^{+3}$ cation is non-polarizable. Because bismuth is highly

polarizable, it greatly adds to the oxygen transport. The lone pair of electrons on the $Bi^{+3}$ cation is displaced from the $O^{-2}$ anion causing a charge separation that decreases Coulombic repulsion and enhances diffusion. Thus, for all bismuth oxide systems, the conductivity can be maximized when the concentration of the bismuth cation is maximized due to the increase in polarizability.

Although the conductivity of $Bi_2O_3$ is exceptional, it cannot be used as a single electrolyte in solid oxide fuel cells because of decomposition at low $PO_2$ ranges[37–39]. The bismuth oxide material is therefore used in bilayer design with a YSZ or GDC electrolyte to not only protect the $Bi_2O_3$ from decomposition, but also boost the performance of the cell[10,37,40,41]. A stable electrolyte layer such as YSZ or GDC on the fuel side of an SOFC will incur a voltage drop across it, thus lowering the effective $PO_2$ on the bismuth oxide portion. **Fig. 1.3.7** depicts a GDC layer protecting an ESB electrolyte from a low $PO_2$ environment.

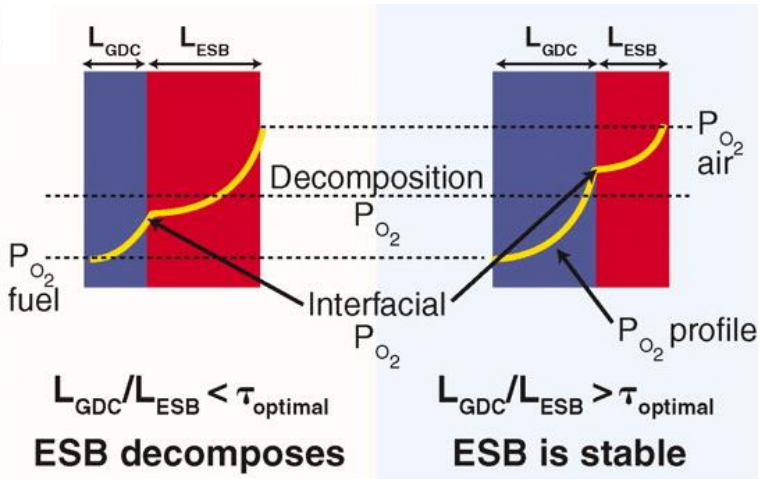


**Fig. 1.3.7**. The effect of relative thickness and $PO_2$ on ESB stability in an ESB/GDC electrolyte bilayer design. Fig. taken from[10].

The bilayer electrolyte design is interdependent. The GDC layer protects the bismuth oxide layer from decomposing, and the bismuth oxide electrolyte increases performance. With higher conductivity, the $Bi_2O_3$ layer can be increased while the traditional electrolyte layer shortened, ultimately decreasing the ohmic resistance of the cell and increasing the power density. Furthermore, the bismuth oxide layer can act as a blocking layer. GDC is not a pure ionic conductor at reducing conditions, and thus bismuth oxide can block leakage current and increase the operating voltage of an SOFC. Overall a bismuth oxide electrolyte must have high ionic conductivity, low electronic conductivity, and good structural and ionic stability at intermediate temperatures to be effective in a SOFC bilayer design.

### *1.4 Fundamentals of Solid State Sodium Batteries*

Inexpensive and reliable batteries for grid-scale storage is vital to facilitating the continued use of clean renewable energy. Alternative energy sources such as wind and solar require large energy storage devices to continue delivering electricity when the wind is not blowing, or the sun goes down. Utilizing batteries for energy storage at the grid level can ultimately improve reliability and stimulate renewable energy[42,43] Specifically Sodium-ion batteries offer a viable, lower cost alternative to lithium-ion batteries for grid-level storage[44–46].

While sodium-ion batteries have shown promise, it is the all-solid-state sodium battery that offers the best of all worlds. The solid state battery is a safer, cheaper, and more reliable alternative to other battery chemistries[47,48]. While the energy density of an all-solid-state sodium battery is sufficient for many applications, the performance is largely dependent on the anode and cathode chemistry that is applied. Authors have

demonstrated rechargeable solid state sodium batteries operating with a sodium metal anode[49–51] or a $Na_3V_2(PO_4)_3$ anode[47,48,52]. Furthermore different cathode materials have been tested in solid state sodium batteries including sulfur[49,50], $Na_3V_2(PO_4)_3$[47,48,51,52], and $Na_{0.7}CoO_2$[53]. No matter the chemistry of a solid state sodium battery, the fundamental elements that govern its operation will be the same. **Fig. 1.4.1** is a diagram that details the operation of an all-solid-state sodium battery.

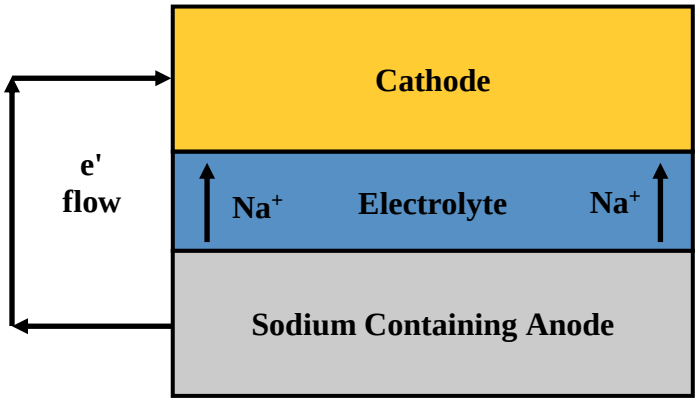


**Fig. 1.4.1**. Diagram of a solid state sodium battery during operation. Flow of sodium ions and electrons are labeled.

Inside the battery, the sodium anode will oxidize to sodium ions and the resulting electrons will flow through the external circuit. Simultaneously the sodium ions will diffuse through the electron blocking electrolyte to recombine with the electrons at the cathode. Overall the electrolyte is a very important component of the solid state battery. It must have high ionic conductivity, low electronic conductivity, and chemical stability with sodium. Ultimately increasing the ionic conductivity of a solid state electrolyte is especially important if the battery is going to be run at room temperature.

*1.5 NASICON as a Solid State Sodium Battery Electrolyte*

One of the major hurdles in creating a room temperature solid state sodium battery is finding a solid electrolyte with high enough conductivity. NASICON ($Na_3Zr_2Si_2PO_{12}$) was selected as a blueprint for investigation by many authors due to its high conductivity[50,54–56]. While it has relatively high conductivity for a solid state electrolyte, NASICON still has lower conductivity compared to many liquid electrolyte counterparts[57–60]. Ultimately modifications to the NASICON structure could lead to an increase in the room temperature sodium ion conductivity, and make it a promising candidate for solid state sodium batteries.

$Na_3Zr_2Si_2PO_{12}$ is a three-dimensional solid network composed of sodium sites nestled between interlocking silica and phosphorus tetrahedrons and zirconia octahedrons, and was originally developed by Hong and Goodenough as a fast sodium ion conductor[61,62]. The NASICON structure is depicted in **Fig. 1.5.1**.

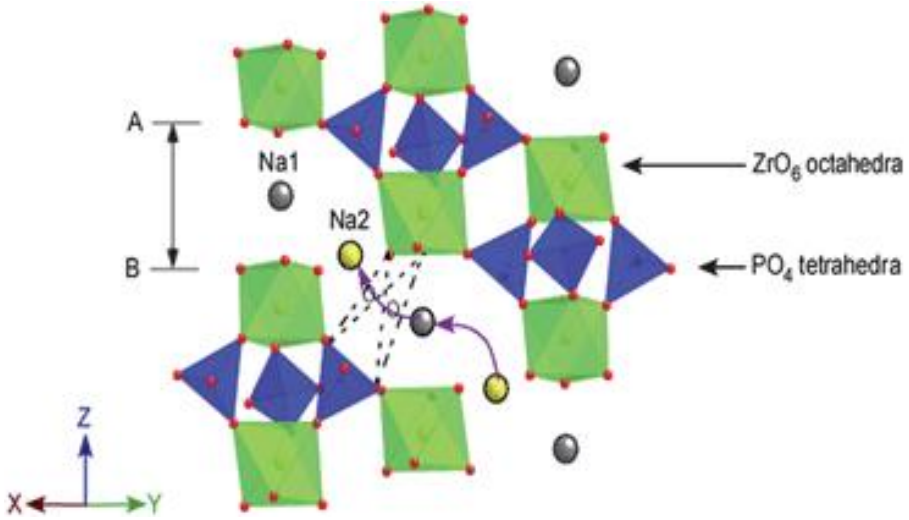


**Fig. 1.5.1**. Schematic of the $Na_3Zr_2Si_2PO_{12}$ structure. This includes the red spheres as oxygen, a mixture of $PO_4$ and $SiO_4$ tetrahedra, $ZrO_6$ octahedra, and the transport path of $Na^+$ indicated. Fig. taken from[11].

The NASICON structure can vary greatly since it is comprised of four sodium sites that can have between 25% and 100% occupancy as well as interchangeable silicon and phosphorus sites. Therefore while the NASICON compound $Na_{1+x}Zr_2Si_xP_{3-x}O_{12}$ (x=2) is regarded as having the highest conductivity, the lattice parameters and conductivity change significantly from x=0 to x=3[62,63]. Not only can the sodium concentration as well as the Si to P ratio vary in NASICON, but it is also possible dope the structure. Some doping studies have been carried out to decrease the grain boundary resistance and thus boost the total conductivity of NASICON. It has been demonstrated that doping the zirconia site of $Na_3Zr_2Si_2PO_{12}$ with yttrium can improve the microstructure and density and consequently increase the total conductivity[12,64]. The improvement to the microstructure and conductivity of NASICON due to yttrium substitution is illustrated in **Fig. 1.5.2 a.**, **b.**, and **c**.

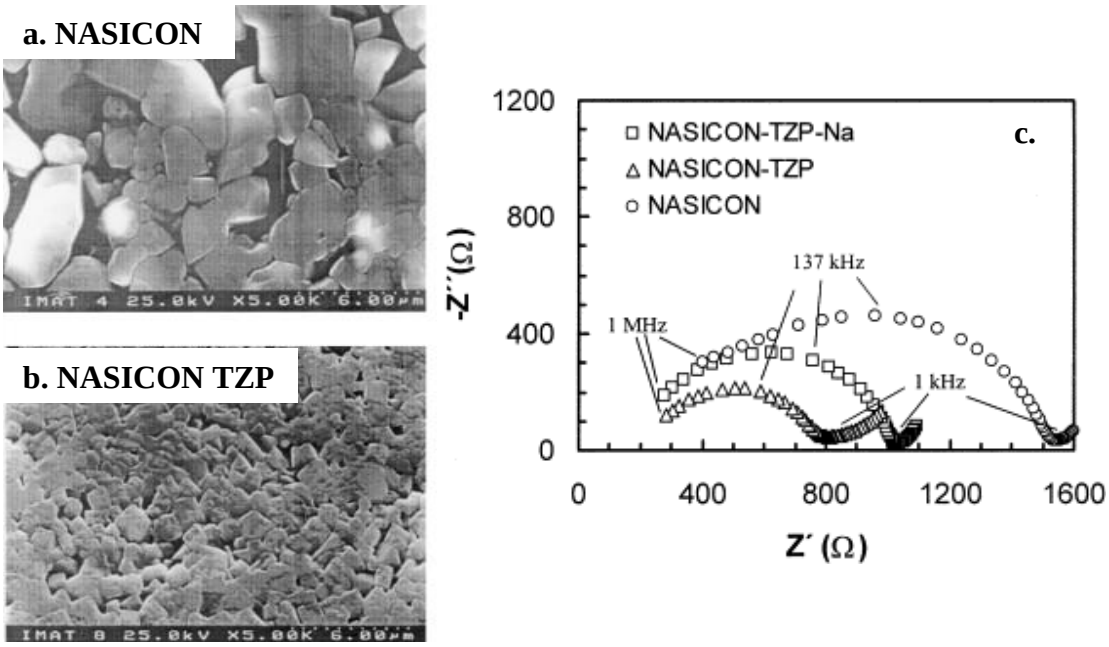


**Fig. 1.5.2 a.** SEM images of undoped NASICON. **b.** SEM images of NASICON doped with 3% $Y_2O_3$ using tetragonal polycrystalline zirconia (TZP). **c.** EIS plot of undoped and TZP doped NASICON. Fig. is taken from[12].

It is clear from the figure that the NASICON-TZP has better necking between particles. This is particularly important for mitigating grain boundary resistance to improve the total conductivity. The EIS data of the undoped NASICON illustrates that the majority of the resistance across the sample was caused by the grain boundary component. Doping the lattice improved the microstructure, and thus the resistance of the NASICON was cut in half. Since much of the conductivity depends on the grain boundary resistance, it follows that many authors would focus on reducing the grain boundary contribution. Nevertheless, understanding the effect of doping on the bulk properties of NASICON is also a primary component of increasing the conductivity.

Other authors have studied the impact of doping on the bulk properties of NASICON, but there has not been a general consensus on what component is most influential on the conductivity. It has been demonstrated that doping the zirconium site with larger radius trivalent cations in the NASICON structure $NaZr_2P_3O_{12}$ produced an increase in conductivity[65,66]. This trend appears to be limited to the silicon free version of NASICON though. There is less consensus on the effectiveness of doping the zirconium site of the $Na_3Zr_2Si_2PO_{12}$ compound. The dopant cations radius and valence do not have a distinct impact on the NASICON conductivity. Depending on the substituted cation, both higher and lower valance can either increase or decrease the conductivity of NASICON while the ionic radius does not have a clear effect on the conductivity[67,68]. More recently though, it has been demonstrated that decreasing the ionic radius of an aliovalent dopant or increasing the concentration of sodium in the lattice can increase the conductivity of NASICON[50,69]. In both cases the increase of conductivity resulted from an opening of the conductivity pathway. The decreased

ionic radius of the substituted divalent cation increased the opening of the bottleneck that the sodium ion must pass through. Excess sodium also expanded the pathway that sodium ion is transported through. The bottleneck opening of NASICON is illustrated in **Fig. 1.5.3**.

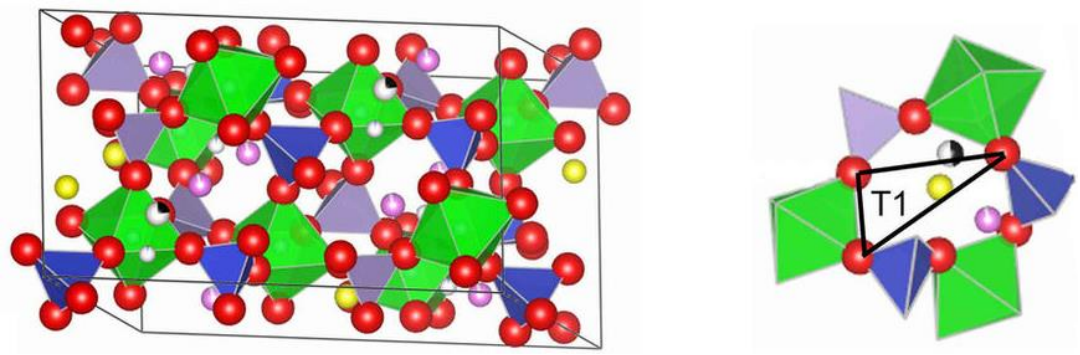


**Fig. 1.5.3**. Unit cell of NASICON on the left. It is comprised of green $ZrO_6$ tetrahedra, blue $SiO_4$ tetrahedra, purple $SiO_4$ tetrahedra, red oxygen spheres, and purple, yellow, and white sodium ions. The bottleneck that sodium ions travel through is indicated on the right by triangle T1. Fig. is taken from[69].

Understanding the effect of doping on the phase of the material is also an important angle of study. In general the highly conductive $Na_3Zr_2Si_2PO_{12}$ solid solution has the rhombohedral *R3c* space group above approximately 160°C-167°C, but transitions to the monoclinic *C2/c* space group below this temperature[13,70]. The phase transition has a large impact on the mobility of sodium ions in NASICON. The higher symmetry rhombohedral phase has a lower activation energy barrier for sodium ion transport. Ultimately NASICON would exhibit higher conductivity at room temperature if the phase change could be bypassed due to the lower activation energy of the rhombohedral phase. The Arrhenius behavior of the rhombohedral and monoclinic phase of NASICON is illustrated in **Fig. 1.5.3**.

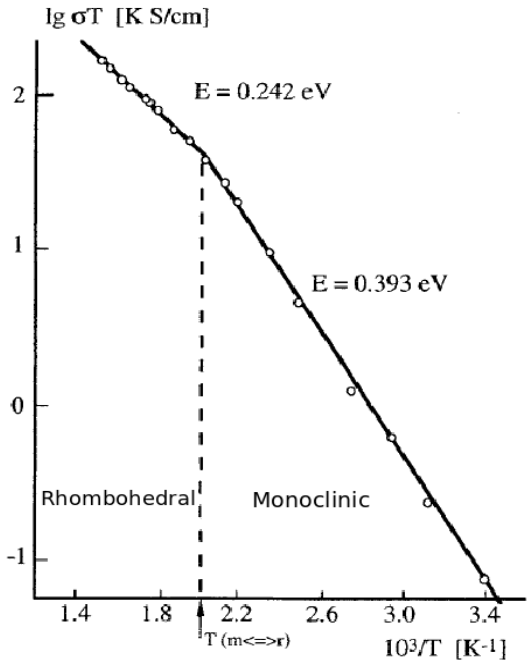


**Fig. 1.5.4**. Arrhenius behavior of NASICON over a large temperature region. The dotted line indicates where the phase transitions from rhombohedral to monoclinic. Fig. taken from[13].

Ultimately the phase transition in NASICON is both temperature dependent and reversible. In contrast, the $Na_3Zr_2Si_2PO_{12}$ crystal structure will permanently transform if the sodium, silicon and phosphorus stoichiometry is altered. The end members of $Na_{1+x}Zr_2Si_xP_{3-x}O_{12}$ (i.e. x=0 and x=4) are rhombohedral at room temperature, but their lattice parameters are observed to change significantly as x approaches 2 with the lattice distorting back to the monoclinic crystal structure[71]. In fact, Colomban et al. demonstrated that incrementally increasing sodium by increasing the silicon to phosphorus ratio in $Na_{1+x}Zr_2Si_xP_{3-x}O_{12}$ caused the critical temperature (Tc) of the phase transition to be continuously lowered until the rhombohedral phase was stabilized at room temperature[72]. While silicon and phosphorus substitution has been studied widely, zirconium substituted NASICON is notably less understood.

# Chapter 2: Experimental Procedures

## *2.1 SOFC Electrolyte Bismuth Oxide Synthesis*

All bismuth oxide electrolyte materials were synthesized using a standard solid state synthesis route. There were a number of bismuth oxide materials produced by mixing raw materials together in a stoichiometric ratio. In all cases the $Bi^{+3}$ cation in $Bi_2O_3$ was substituted with a dopant cation. Raw materials included $Bi_2O_3$ (Alfa Aesar 99.99%), $La_2O_3$ (Alfa Aesar 99.9%), $Nd_2O_3$ (Sigma Aldrich 99.9%), $Gd_2O_3$ (Alfa Aesar 99.9%), $Dy_2O_3$ (Alfa Aesar 99.9%), $Er_2O_3$ (Alfa Aesar 99.9%), $Sm_2O_3$ (Alfa Aesar 99.9%), $Y_2O_3$ (Alfa Aesar 99.9%), $CaCO_3$ (Alfa Aesar 99.5%), and $SrCO_3$ (Sigma Aldrich 99.9%).

The raw materials were mixed together with ethanol and YSZ media to provide mixing and grinding. The raw materials were ball milled for twenty-four hours in ethanol. After twenty-four hours of ball milling, the slurry was passed through a sieve and into a metal pan where it was dried at 100°C. The resulting powder was placed in an alumina crucible and calcined at 800°C for 16 hours with a heating and cooling rate of 5°C per minute. After calcining was complete, the samples were removed from the crucibles and hand ground with a mortar and pestle. The hand ground powder was then ball milled in ethanol a second time for 24 hours. The slurry was dried again at 100°C and the resulting powder was pressed into pellets. The pellets were pressed in 10 mm steel die and a carver press. The disks were generally sintered at 800°C for 16 hours with a heating and cooling rate of 5°C per minute unless otherwise stated.

*2.2 SOFC Symmetric Cell Fabrication and Cathode Synthesis*

Symmetric cells were fabricated to determine the effectiveness of bismuth oxide samples in a composite cathode design. The composite cathode was made by mixing $Bi_2O_3$ electrolytes produced by solid state reactions with an $La_{0.8}Sr_{0.2}MnO_3$ (LSM, Fuel Cell Materials) cathode powder in ethanol. The ratio of cathode to electrolyte powder was varied and will be discussed later. The slurry was ball milled for twenty-four hours prior to making the cathode paste. After ball milling, the slurry was blended in a Thinky centrifugal mixer and the ethanol was slowly replaced with a vehicle for the composite cathode powder (ESL type 441 thinner). The cathode paste was ready for deposition after it reached an optimal consistency, which occurred when the ESL thinner and cathode reached approximately equal weight and all the ethanol was removed. The cathode paste was blade coated on to the face of a dense $Bi_2O_3$ electrolyte pellet and dried at 120°C for one hour. After drying was complete, the other pellet face was coated with cathode paste and dried at 120°C for an additional hour. The symmetric cell was fired under different conditions and will be discussed in more depth in Chapter 5.

*2.3 SOFC Full Cell Fabrication*

Full SOFC button cells with a bilayer design were fabricated for testing. The cell is comprised of a porous Ni-GDC anode support layer (ASL), a Ni-GDC anode functional layer (AFL), a dense GDC electrolyte, a dense $Bi_2O_3$ electrolyte, and finally a $Bi_2O_3$-LSM composite cathode. A schematic of the full SOFC with approximately layer thicknesses is illustrated in **Fig. 2.3.1**.

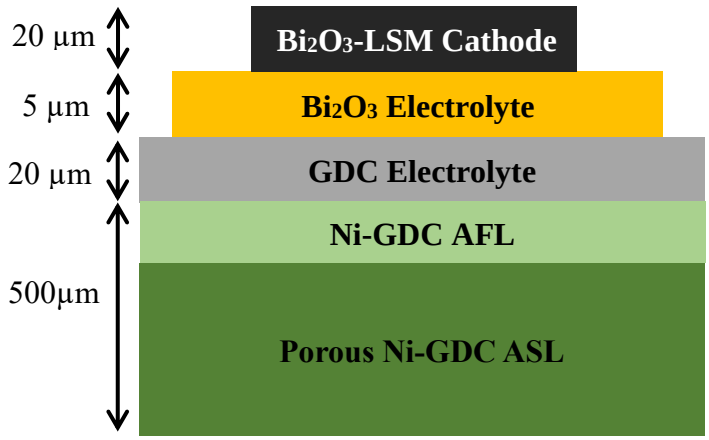


**Fig. 2.3.1**. Schematic showing the cross-section of an SOFC button cell with a bi-layer electrolyte design. The left side details the approximate thickness of each layer (not drawn to scale).

The anode, AFL, and GDC electrolyte were all fabricated using a tape casting method. The raw materials consisted for these layers consisted of NiO (99.9% Alfa Aesar) and $Ce_{0.9}Gd_{0.1}O_2$ (JT Baker). The appropriate amount of raw materials were ball milled for twenty four hours with toluene and ethanol as solvents, as well as menhaden fish oil (Tape Casting Warehouse). Next, a binder of polyvinyl butyral (PVB) and the plasticizer butyl benzyl phthalate (BBP) was added to the slurry and milled another twenty four hours. After milling, the slurry was de-aired in a vacuum chamber with additional ethanol to prevent a skin formation on the surface. The slurry was then poured on a Mylar sheet, which was pulled through a doctor blade set on a tape caster bed (Procast). Once this process was complete, the tape dried on the bed set at 120°C. Finally the complete tapes of the ASL, AFL, and GDC electrolyte were laminated together with a Carver hot press at 180°C and 180 psi. The resulting tape was presintered at 900°C for 2 hours and fully sintered at 1450°C for 4 hours.

After completing the anode half-cell, the $Bi_2O_3$ electrolyte and composite cathode layer needed to be added. The bismuth oxide electrolyte and composite cathode layer were deposited using a blade coat method rather than tape casting. The $Bi_2O_3$ electrolyte ink for blade coating was fabricated following the same steps for making the composite cathode ink that was described earlier. The electrolyte ink was blade coated on the anode half-cell and fired at 775°C for 2 hours to make a dense layer. The composite cathode ink was then blade coated on to the $Bi_2O_3$ layer and fired at 725°C for 2 hours. After the cathode finished sintering, the final SOFC button cell was ready for testing.

*2.4 Sodium Battery NASICON Electrolyte Synthesis*

All NASICON samples were synthesized using conventional solid state procedures and consisted of an aliovalent cation substitution of zirconium. The nominal compositions were $Na_3Zr_2Si_2PO_{12}$, $Na_{3.2}Zr_{1.8}M_{0.2}Si_2PO_{12}$ ($M=Al^{3+}$, $Fe^{3+}$, $Y^{3+}$), and $Na_{3.4}Zr_{1.8}M_{0.2}Si_2PO_{12}$ ($M=Co^{2+}$, $Ni^{2+}$, $Zn^{2+}$). Additionally, the amount of divalent cation substitution was varied for each sample and had the general formula $Na_{3+2x}Zr_{2-x}M_xSi_2PO_{12}$ (for x=0.1 0.2, 0.3, 0.4, 0.5 and $M=Co^{2+}$, $Ni^{2+}$, $Zn^{2+}$). The raw materials used in the synthesis included $Na_2CO_3$ (Sigma-Aldrich, 99.95-100.05%), nanocrystalline $ZrO_2$ (Inframat Advanced Materials, 99.9%) amorphous $SiO_2$ (Sigma-Aldrich, 99.80%), and $Na_2HPO_4{\cdot}7H_2O$ (Sigma-Aldrich, 98.0-102.0%), were mixed with 2% excess phosphorus and sodium to compensate for volatility. The dopant raw materials were added to NASICON raw materials in a stoichiometric ratio and included $Al_2O_3$ (Inframat Advanced Materials, 99.99%), $Fe_2O_3$ (Sigma-Aldrich,

≥99%), $Y_2O_3$ (Alfa Aesar, 99.9%), $Co(NO_3)_2 \cdot 6H_2O$ (Carolina, 98.0-102.0%), NiO (J.T. Baker, ≥99%), and ZnO (J.T. Baker, ≥99%).

The raw materials were ball milled with 8 mm YSZ media in isopropanol for twenty-four hours. After ball milling the slurry was sieved into a metal pan and dried at 100°C. The resulting powder was placed in an alumina crucible and calcined at 700°C for 12 hours. The calcined powders were ground with an agate mortar and pestle and ball milled in isopropanol for twenty-four hours. The slurry was sieved and dried again and a second calcination of the powder occurred at 900°C for 12 hours. A final grinding of the calcined powder with a mortar as well as 24-hour ball milling in isopropanol was carried out. After sieving and drying of the slurry, the calcined powder was pressed into pellets using a 10mm steel die and a metric ton of uniaxial force from a carver press. The pellets were sintered for 12 hours in alumina crucibles at a range of temperatures that will be discussed later. The heating and cooling rates for all calcining and sintering were 5°C/minute.

*2.5 Electrochemical Impedance Spectroscopy*

Electrochemical Impedance Spectroscopy (EIS) is an important technique for measuring the performance of an electrochemical cell. Specifically, EIS was used to measure the impedance of the cell which was then translated to the conductivity. The impedance of a system is determined by Eq. 2.5.1

$$Z\ (\omega) = \frac{V(t)}{I(t)} \qquad \text{(Eq. 2.5.1)}$$

For this equation V is the AC voltage and I is the current. The impedance Z has a real (Z') and imaginary (Z") component that are related by Eq. 2.5.2.

$$Z\ (\omega) = Z' + iZ''$$ (Eq. 2.5.2)

The real and imaginary parts of the impedance can be plotted on a Nyquist plot so that Z' is plotted on the x-axis and Z" is on the y-axis. The Nyquist plot is composed of a high frequency capacitance arc related to the electrolyte and a low capacitance arc related to the electrodes. The real portion of the impedance Z' can be related to the resistance, R, by Eq. 2.5.3.

$$Z' = R$$ (Eq. 2.5.3)

Ultimately the resistance of the arc can be translated to electrical conductivity, σ, with Eq. 2.5.4.

$$\sigma = \frac{L}{A \bullet R}$$ (Eq. 2.5.4)

In this equation, L is the total thickness of the species, A is the cross-sectional area, and R is the resistance measured by EIS. The conductivity of the electrolyte be expressed as S/cm while electrodes or full cells will be in terms of area specific resistance (ASR) or ohm/cm$^2$.

In practice it can be difficult to interpret raw EIS data. Non-perfect semicircles, test setup inductance, and wire resistances all add to potential reading error. Furthermore, the raw data itself can be difficult to model and interpret. Thus, all EIS data was modeled with equivalent circuit models and fit with Scribner Z-view software to obtain the best possible fits. The fit data was then compared to literature vales to confirm the components of the EIS arcs. In general, the calculated capacitance of the arcs could help identify the different regions of the EIS plot. **Table 2.5.1** lists EIS phenomena associated with different capacitance values.

| Capacitance (F) | Phenomenon Responsible |
|---|---|
| $10^{-12}$ | Bulk |
| $10^{-11}$ | Minor, secondary phase |
| $10^{-11} – 10^{-8}$ | Grain boundary |
| $10^{-9} – 10^{-7}$ | Surface layer |
| $10^{-7} – 10^{-5}$ | Sample-electrode interface |
| $10^{-4}$ | Electrochemical reactions |

**Table 2.5.1**. Capacitance values measured by EIS and the possible interpretation. Table adapted from[2].

The conductivity of all electrolyte samples and the ASR of symmetric cells were all determined by EIS. A similar setup was used for the measurement of all the samples. An alumina tube with four bored holes was outfitted with four separate silver wires. Two of the wires were attached to silver mesh and acted as the working electrode and working sense. The other two wires were attached to silver and mesh and acted as the counter electrode and counters sense. The faces of the sample were covered with a conductive paste to act as a current collector and placed between the pieces of mesh. The alumina tube and sample were placed in a tube furnace and the thermocouple controlling the furnace was placed directly above the sample. The exact procedure was different for each sample.

The $Bi_2O_3$ electrolyte was coated on both faces with Heraeus gold paste to act as a current collector. The gold paste was not fired at high temperature but rather sintered in situ at the maximum temperature that the electrolyte conductivity was measured (generally 700°C or 550°C). Resistance of the samples was determined from

fitting the impedance plot with Z-view software and the conductivity was calculated using Eq. 2.5.4. A Solartron 1260A frequency response analyzer (FRA) was used to measure the impedance of electrolyte samples under an AC voltage of 50 mV and a frequency range of 1 Mhz to 1 Hz. For aging of the electrolyte samples, a Solartron 1260A and a Solartron 1470E that acted as a multiplexer was employed to take hourly EIS measurements of samples as they aged.

The bismuth oxide symmetric cells were measured much the same way that the electrolyte samples were measured. Heraeus gold paste was painted on both faces of the symmetric cell to act as a current collector and the resistance was measured with a Solartron 1260A FRA and Solartron 1470E multiplexer. The resistance was divided by the area of the two electrode areas to determine ASR. As opposed to the electrolyte, only the low frequency, non-ohmic portion of the EIS plot was used in ASR calculation. The electrode response is located at low frequency and low capacitances.

The faces of the NASICON electrolytes were painted with platinum paste and fired at 700°C for one hour. The impedance sweep was from 5 Mhz to 1 Hz using 250 mV AC voltage. The bulk and total conductivity were deciphered from the EIS plot using Z-view software.

### *2.6 Transference Number Measurements*

The transference number of $Bi_2O_3$ was calculated using voltage measurements. The bismuth oxide sample was sealed between two gaseous environments with different oxygen concentrations. The open circuit potential (OCP) generated by the oxygen activity was measured and compared to the theoretical Nernst potential. To measure the OCP, silver paste was applied to both faces of a sintered $Bi_2O_3$ disk and

acted as electrodes for the measurements. The sample was sealed between two gas lines with a compressive seal made from Thermicullite 866 O-rings. The cell was tightened down with bolts to facilitate the seal around the O-rings. One gas line supplied air, while the other gas line supplied gas mixtures with a range of $PO_2$ values. An oxygen sensor was used downstream to measure the exact $PO_2$ being supplied to the sample. The OCP was measured using a Solartron 1455A FRA connected to a 1470E potentiostat.

The transference number of NASICON was calculated using a DC polarization technique. DC measurements were performed on sintered pellets in air at 25°C. Lead wires from a Keithley 2400 Broad Purpose SourceMeter provided current to the blocking platinum electrodes on the sintered disks. Measurements were run until the current stabilized, and the electronic conductivity was calculated by normalizing the resistance to pellet thickness and area.

### *2.7 SOFC Button Cell Testing*

A Solartron 1400 CellTest system was used to perform galvanostatic measurements of cell OCP and power density, as well as EIS measurements for ASR. These measurements were performed on an SOFC button cell using hydrogen fuel on the anode side and air on the cathode side. The gas was controlled with mass flow controllers and set to 200 SCCM. The button cell was sealed on an alumina tube that supplied the hydrogen to isolate the two gas streams using a ceramic sealant (Ceramabond). The anode side was connected to the working and sense electrodes using silver wires that bonded to the cell with silver paste (ESL). The cathode side was connected to the counter and reference electrodes with silver wires adhered to the cell

with gold paste (Heraeus). Once the button cell was connected and sealed with Ceramabond, it was dried for 4 hours at room temperature. The setup was then moved to furnace for a final curing procedure of 94°C for 2 hours and 265°C for 2 hours. Finally, the cell was heated up to the maximum temperature of testing where the anode could be reduced.

### *2.8 X-ray Diffraction*

X-ray diffraction (XRD) was performed on crushed and ground powder. For all room temperature XRD, sintered pellets were ground with an agate mortar and pestle to obtain fine powder. The room temperature XRD was collected with a Bruker D8 X-ray Diffractometer using Cu Kα radiation. High temperature XRD studies were performed with a Bruker C2 Discover X-ray Diffractometer with Cu Kα radiation and 2D area detector. An Anton Paar DHS 1100 hot stage was used for sample heating. Approximately 50mg of each powdered sample was pressed into a 6mm pellet with 1,000 lbs. of uniaxial force and placed on a Pt foil for heating. Each sample was heated at a rate of 100 C/min and held for 1 minute at the destination temperature before the pattern was collected. The high temperature XRD data was fit using the Le Bail method with the software program TOPAS (Bruker AXS, Karlsruhe, Germany) to obtain lattice parameters. The room temperature lattice parameters were extracted from room temperature XRD patterns using Rietveld refinement on TOPAS.

### *2.9 Microscopy and Elemental Analysis*

A Hitachi SU-70 scanning electron microscope (SEM) was used for the imaging of all materials and the accelerating voltage was generally set at 2.0 keV. For imaging,

samples were placed on double sided carbon tape as a way to minimize charging. Elemental analysis of NASICON samples was performed using a JEOL 8900 electron probe microanalyzer that employed standard wavelength-dispersive spectroscopy (WDS). The microprobe settings included a beam diameter of 30 μm, an accelerating voltage of 15 kV with current of 1 nA, and the absorbed current was monitored to detect sample degradation. Above sample currents of 1 nA or a beam diameter below 30 μm, electron densities would stimulate sodium migration and generate inaccurate elemental readings. ZAF correction procedures corrected raw x-ray counts, and determined the composition. Oxygen content was not directly measured. The oxygen stoichiometry of undoped NASICON was applied to all samples and was included in the ZAF corrections.

### *2.10 Differential Scanning Calorimetry*

Differential Scanning calorimetry (DSC) measurements were performed on NASICON samples using a Perkin Elmer Pyris 1. Measurements were taken in the temperature range 100°C to 200°C and a ramp rate of 5°C per minute was used. Approximately 15 mg of powder for each sample was analyzed, and the critical temperature (Tc) corresponded to the endothermic peak of the measurements and was determined by the Pyris Thermal Analysis Ver. 7 software.

# Chapter 3: Doping $Bi_2O_3$ to Improve Conductivity and Stability

## *3.1 Motivation*

Decreasing the operating temperature of an SOFC below 600°C is the main objective of this study. Because the conductivity of traditional electrolytes is not high enough to achieve high performance in cells operating at low temperatures, electrolytes with higher oxygen ion conductivities were considered. As discussed earlier, doped cubic bismuth oxide has very high ionic conductivity, but rather poor stability below approximately 600°C. Thus, doped bismuth oxide materials generally have sufficient conductivity at reduced temperatures, but experience a large decay in conductivity that drives cell performance down. Overall the objective of this work is to develop a $Bi_2O_3$ material that is stable in phase and conductivity below 600°C. Initially the cubic phase of bismuth oxide was studied and methods of reducing the degradation in conductivity was explored. Ultimately the rhombohedral phase of $Bi_2O_3$ was selected for its high stability and modifications of the material were examined to sufficiently improve the ionic conductivity.

## *3.2 Effects of Lanthanide Substitution on Cubic $Bi2O_3$*

As previous authors have shown, a double doping strategy was employed to minimize the amount of cation substitution required to stabilize the cubic phase. The dopant level was set at 12% and a range of cations were tested. For the initial study, a secondary cation with a smaller ionic radius was used at a concentration of 4% for

every sample. Niobium was selected as the secondary dopant due to the ionic radius being 0.74 Å. The primary dopant concentration was set at 8% and covered a range of rare earth elements including Dy, Gd, Sm, Nd, and La. This study was established to determine if there is an effect of dopant ionic radius on the aging rate of cubic bismuth oxide.

The list of samples that were tested include $Bi_{0.88}Dy_{0.08}Nb_{0.04}O_{1.5}$ (D8N4), $Bi_{0.88}Gd_{0.08}Nb_{0.04}O_{1.5}$ (G8N4), $Bi_{0.88}Sm_{0.08}Nb_{0.04}O_{1.5}$ (S8N4), $Bi_{0.88}Nd_{0.08}Nb_{0.04}O_{1.5}$ (N8N4), and $Bi_{0.88}La_{0.08}Nb_{0.04}O_{1.5}$ (L8N4). All of these samples existed in the cubic phase at room temperature based on X-ray diffraction. The D8N4 sample showed particularly good conductivity over the range of temperatures tested as seen in **Fig. 3.2.1**.

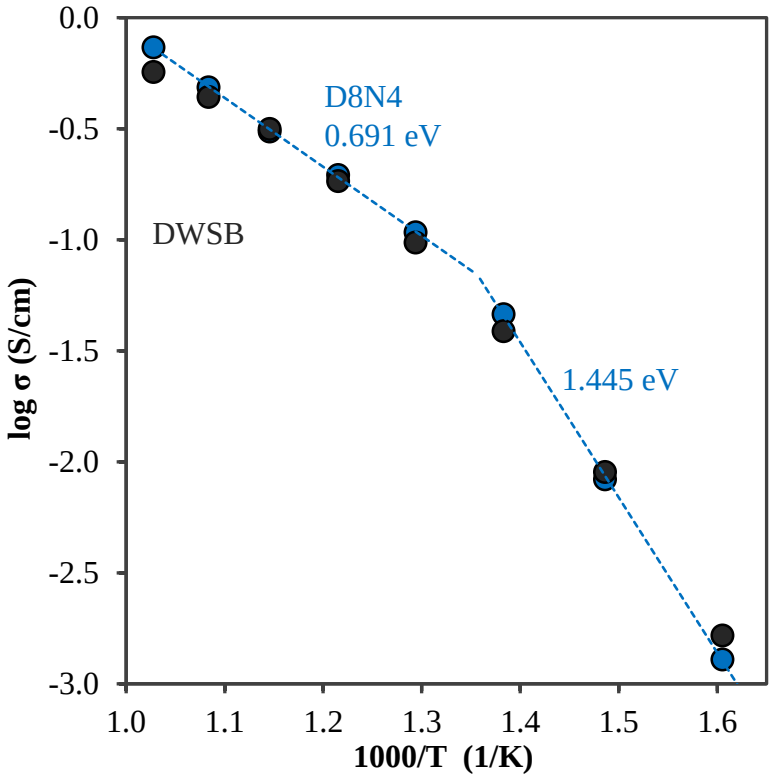


**Fig.3.2.1**. Arrhenius behavior of D8N4 and DWSB. The activation energy of D8N4 is provided on the plot. DWSB is a reference material[18].

Like other doped cubic $Bi_2O_3$ electrolytes, the D84N4 sample had a high temperature and low temperature region present in the Arrhenius behavior. The high temperature region was associated with a disordered oxygen ion sublattice, while the low temperature region was associated with ordered state. The ordered state of cubic bismuth oxide has many fewer equivalent jump directions for oxygen ion transport, which greatly reduced the pre-exponential factor and thus activation energy of the mobile ions. The main issue attributed with the low temperature ordered state of D8N4 was the degradation in conductivity at 500°C. There is a large drop as the disordered state transitions to the ordered state. **Fig. 3.2.2** illustrates the conductivity decay of D8N4 as a function of aging time at 500°C.

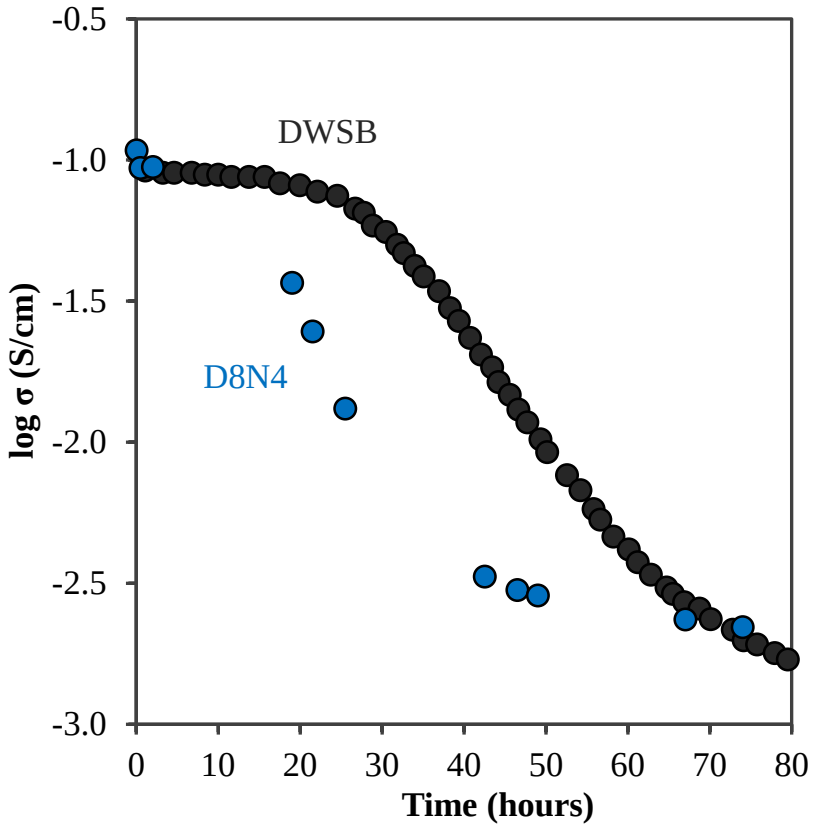


**Fig. 3.2.2**. Conductivity vs. time for D8N4 and DWSB at 500°C. DWSB is a reference material[18].

The other cubic bismuth oxide samples tested all showed similar behavior to the D8N4 sample. A high temperature activation energy attributed to the disordered state and a low temperature activation energy attributed to the ordered state was seen in all cases. Furthermore, the ordering of the oxygen vacancies caused a huge decay in conductivity as the samples were aged for an extended period of time at 500°C. Eq. 3.2.1 models the decay of conductivity.

$$\Delta \log(\sigma) = \log(\sigma_i) - \log(\sigma_f) \qquad \text{(Eq. 3.2.1)}$$

For this equation $\sigma_i$ is initial conductivity and $\sigma_f$ is conductivity measured after aging. The log of initial conductivity minus the log of final conductivity (conductivity after 70 hours of aging at 500°C) is graphed as a function of dopant ionic radius in **Fig. 3.2.3**.

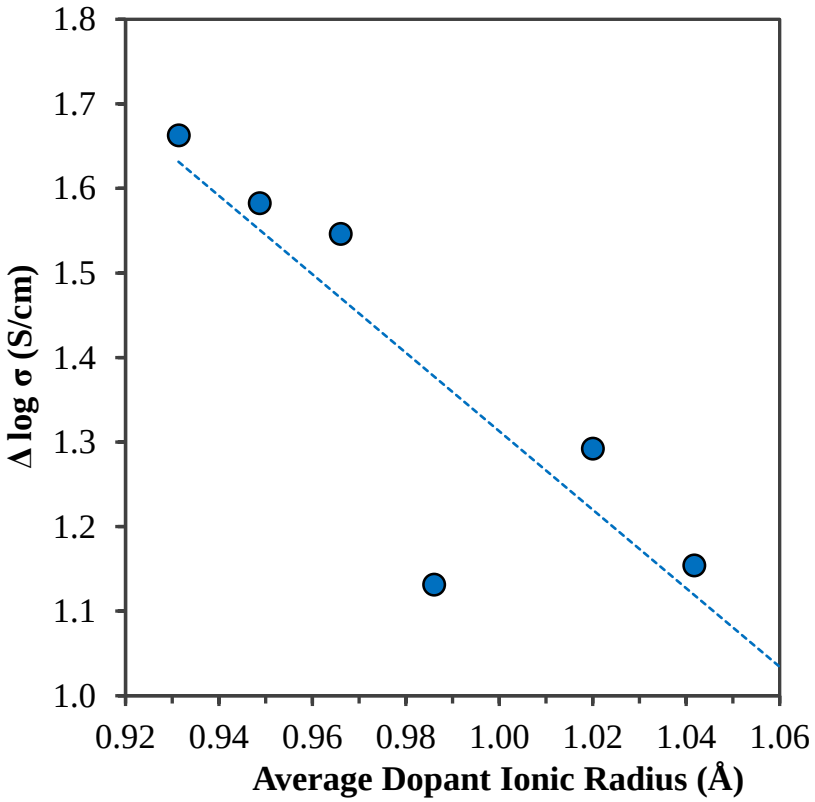


**Fig. 3.2.3**. Change in conductivity vs. average dopant radius of multiple cubic $Bi_2O_3$ samples. Change in conductivity is determined by Eq. 3.2.1 after seventy hours of aging at 500°C.

The cubic $Bi_2O_3$ samples in **Fig. 3.2.3** include D8N4, G8N4, S8N4, N8N4, and L8N4 described earlier as well as $Bi_{0.88}Gd_{0.08}Y_{0.04}O_{1.5}$ (G8Y4), which was used to bump the dopant ionic radius above 1.04 Å. The trend in the data suggests that as the dopant ionic radius increases in cubic bismuth oxide, the stability of the conductivity also increases. The larger dopant ionic radius works to decreases the overall ordering effect and lessens the degradation of conductivity. The ionic radius was investigated further with a second system.

Again, a co-doping strategy was utilized to study the effects of the dopant ionic radius on the conductivity of bismuth oxide. The dopant concentration was set at 10% to decrease the amount of substitution and obtain higher conductivity. For this study, lanthanum and yttrium were selected as dopants due to $La^{+3}$ and $Bi^{+3}$ having similar ionic radii, while $Y^{+3}$ was selected due to its relatively small size. Rather than utilizing different cations to alter the ionic radius, the ratio of La and Y was varied to increase or decrease the average dopant radius. The relative ionic radius was an average of the concentration and ionic radius of $La^{+3}$ = 1.16Å and $Y^{+3}$ = 1.019Å over the 10% total dopant content. The ionic radius was taken from Shannon radii for a coordination eight cation. Two alternative highly conductive bismuth oxide samples were used to compare the performance of materials synthesized here. Both single doped $Bi_{0.8}Er_{0.2}O_{1.5}$ (ESB) and double doped $Bi_{0.88}Dy_{0.08}W_{0.04}O_{1.5}$ (DWSB) were used as reference materials.

Initially, four different samples were synthesized: $Bi_{0.9}La_{0.015}Y_{0.085}O_{1.5}$ (La1.5Y8.5), $Bi_{0.9}La_{0.022}Y_{0.078}O_{1.5}$ (La2.2Y7.8), $Bi_{0.9}La_{0.029}Y_{0.071}O_{1.5}$ (La2.9Y7.1), and $Bi_{0.9}La_{0.036}Y_{0.064}O_{1.5}$ (La3.6Y6.4). This naming scheme will be applied to all subsequent sample. The letters signify the dopant and the numbers signify the

percentage of cation substituted for $Bi^{+3}$. The X-ray diffraction patterns of the doped samples are laid out in **Fig. 3.2.4**.

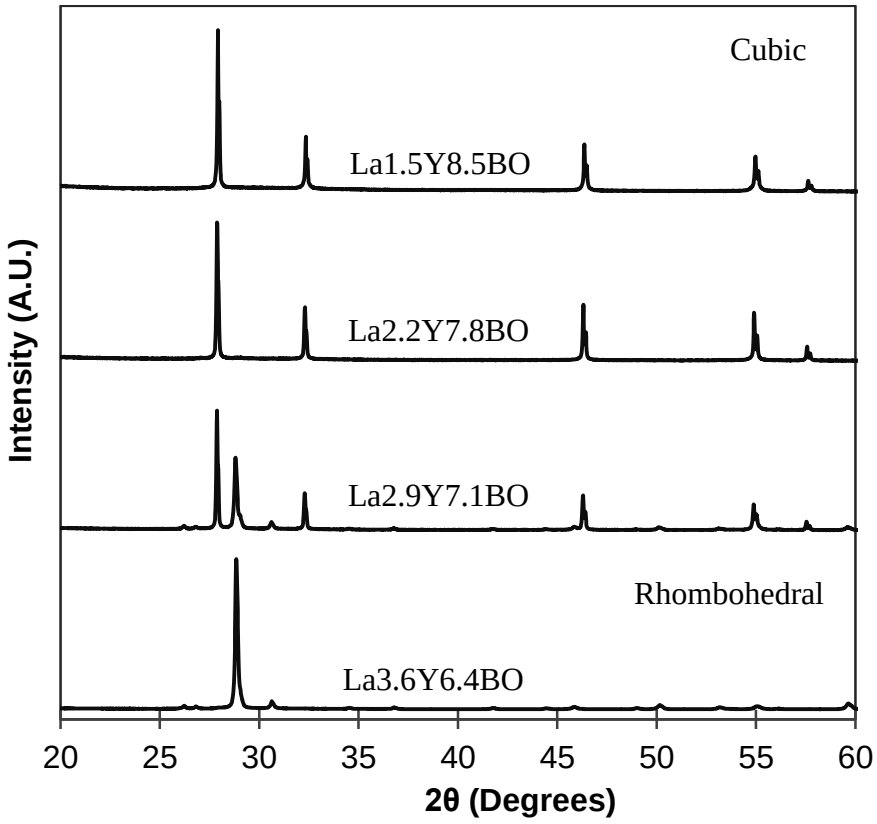


**Fig. 3.2.4**. X-ray diffraction patterns of four different double doped $Bi_2O_3$ samples. La1.5Y8.5 was purely cubic while La3.6Y6.4 was entirely rhombohedral.

It was observed that as the relative ionic radius increased, the amount of rhombohedral phase present in the sample increased. La1.5Y8.5 had an average dopant radius of 1.04Å and existed in the cubic phase, while the La3.6Y6.4 sample was entirely rhombohedral with an average dopant radius of 1.07Å. La2.2Y7.8 had a very tiny impurity peak attributed to the rhombohedral phase while La2.9Y7.1 was clear mixture of the cubic and rhombohedral phase.

The Arrhenius behavior and stability of the cubic La1.5Y8.5 sample were examined first. **Fig. 3.2.5** is the EIS data obtained from the La1.5Y8.5 sample over a range of temperatures.

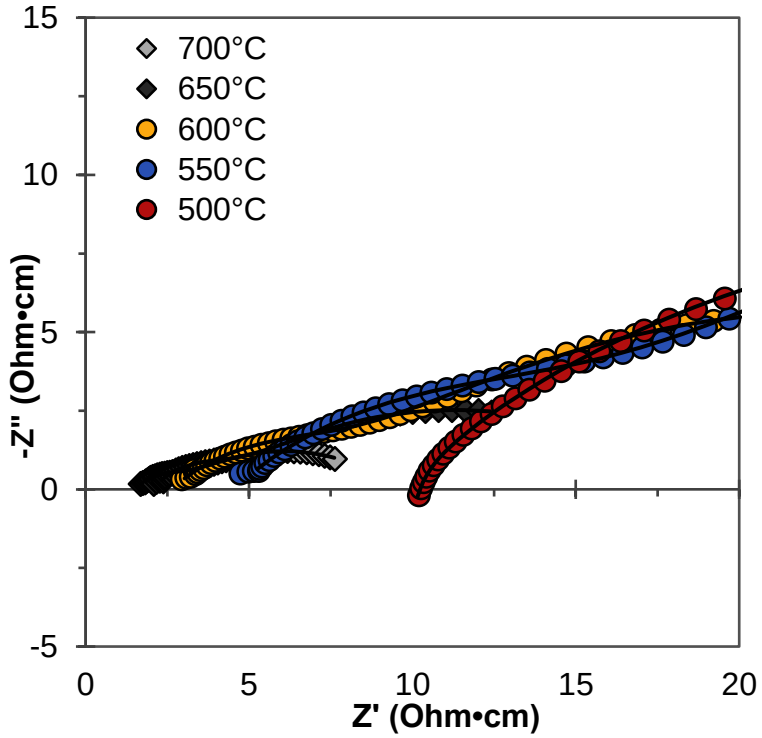


**Fig. 3.2.5**. EIS plot for La1.5Y8.5 from 700°C-500°C. The black lines are the fits of the impedance data.

An equivalent circuit model used to fit the impedance arcs. The equivalent circuit was composed of a resistor in series with two separate resistor and CPE elements in parallel. For temperatures ≤500°C, an inductor was also used to model the EIS data, since inductive effects from the setup became prominent. The high frequency intercept corresponded to the total conductivity of the material with no resolvable grain boundary resistance detected. Meanwhile, the low frequency arcs were attributed to oxidation reduction reactions taking place at the gold current collectors/electrodes. The

conductivity of La1.5Y8.5 at multiple temperatures was determined from the EIS arcs and plotted in **Fig 3.2.6**.

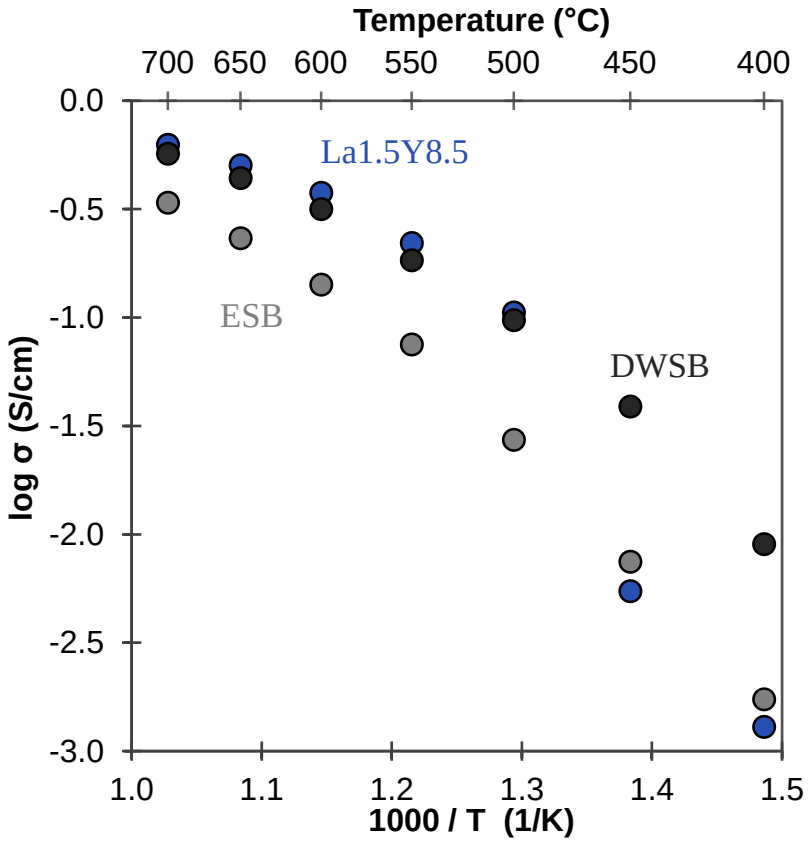


**Fig 3.2.6**. Arrhenius plot of three cubic bismuth oxide samples. The 10% doped La1.5Y8.5 sample is compared to DWSB and ESB for reference. The DWSB and ESB data is taken from[18].

The high temperature conductivity of La1.5Y8.5 is higher than both the previously measured D8N4 and DWSB. This is particularly notable since DWSB has one of the highest known oxygen conductivities below 700°C. The higher conductivity of La1.5Y8.5 is most likely a result of the lowering the overall dopant concentration while still maintaining the cubic phase. Decreasing the amount of bismuth substitution in $Bi_2O_3$ increases the polarizability of the cations and thus the mobility of oxygen ions[9]. The down side of decreasing the dopant concentration is a notable increase in the

rate of ordering. While the previous D8N4 sample exhibited a kink in the activation energy going from the high temperature region to the low temperature region, the La8.5Y1.5 sample shows a large drop in conductivity. The drop off in conductivity below 500°C is most likely a result of the anion sublattice transitioning from the disordered state to the ordered state. The disorder-order transition occurs so rapidly that there is large decay in conductivity just from short period of time the sample was cooled below 600°C.

The stability at 500°C was also investigated. **Fig 3.2.7** is a plot of La8.5Y1.5, ESB, and DWSB conductivity as a function of aging time at 500°C. Like both ESB and DWSB, La1.5Y8.5 exhibited considerable conductivity degradation after just sixty hours of aging at 500°C.

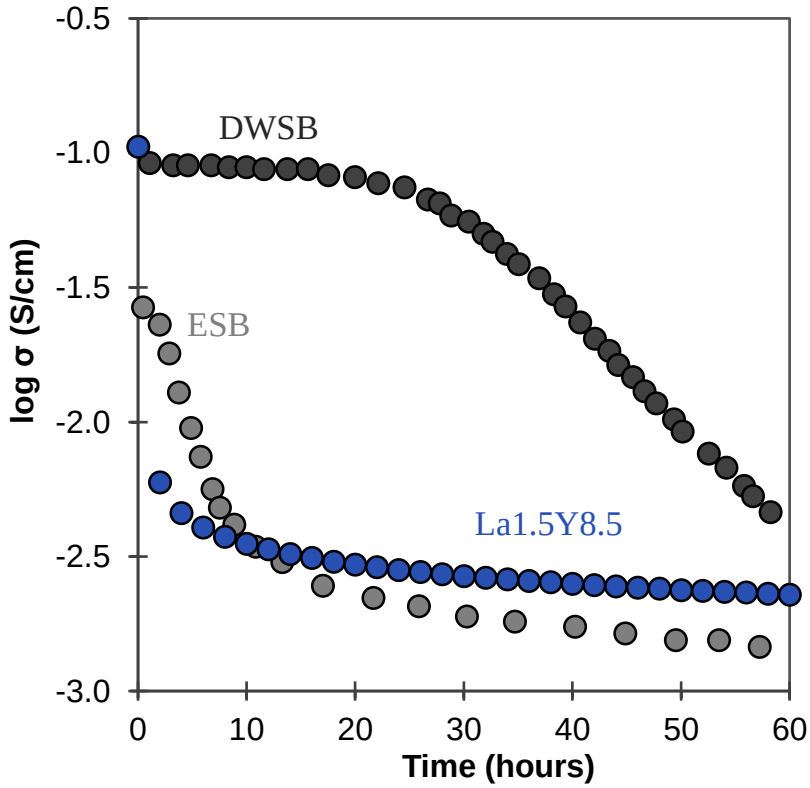


**Fig. 3.2.7**. Conductivity as function of aging time for La1.5Y8.5, DWSB and ESB at 500°C. The DWSB and ESB data is used as a reference and is taken from[18].

While the huge drop in the Arrhenius behavior and the rapid decay in aging conductivity could signify a phase change had occurred in the material, the XRD confirmed the cause was the ordering of oxygen sublattice. **Fig. 3.2.8** is the room temperature X-ray diffraction pattern of the La1.5Y8.5 sample prior to aging and post aging at 500°C for sixty hours.

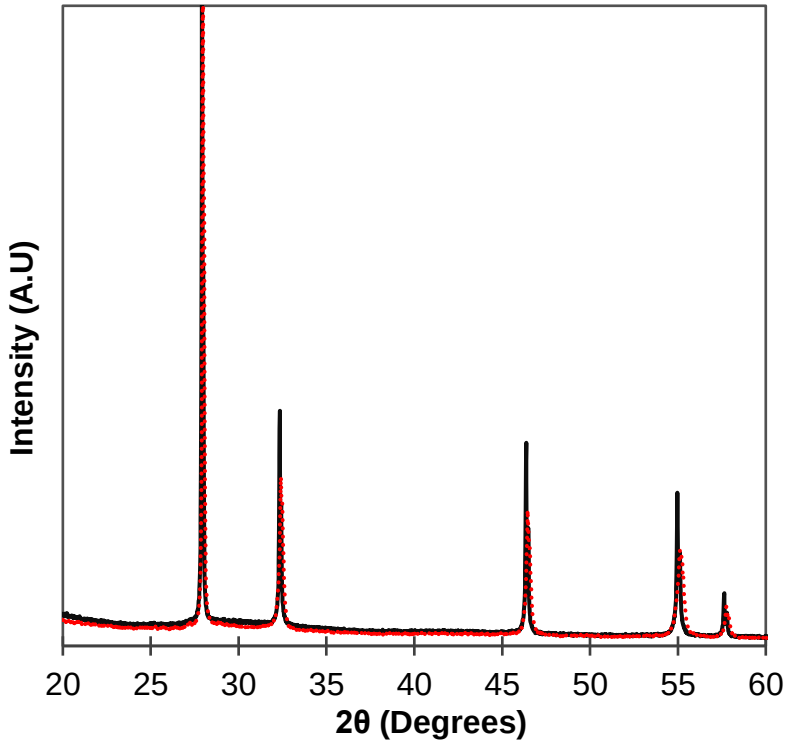


**Fig. 3.2.8**. Room temperature X-ray diffraction pattern of La1.5Y8.5 before and after aging at 500°C for 60 hours. The black line is the initial XRD plot and the dashed line is after aging.

Because the cubic phase was retained after aging, the transition from the disordered to ordered state was the primary cause of conductivity degradation in La1.5Y8.5. The drop in conductivity was more abrupt in the aging of La1.5Y8.5 as a result to faster kinetics in the disorder-order transition. As discussed earlier, the lower dopant concentration allows for more rapid ordering of the oxygen vacancies and a

hence a more rapid degradation of conductivity. Ultimately the cubic phase of bismuth oxide could not be stabilized with cations large enough to stabilize the conductivity at lower temperatures. As the average dopant ionic radius increased, the rhombohedral phase in bismuth oxide began to form. Although stabilizing the cubic phase of bismuth oxide at high dopant regimes was not possible, the rhombohedral phase could be stabilized.

Also, $Zr^{+4}$ was also explored as a dopant due to its small size compared to $Bi^{+3}$. In order to stabilize the cubic phase, the large $La^{+3}$ cation and the small $Zr^{+4}$ cation were both substituted into the $Bi_2O_3$ lattice. The room temperature XRD patterns of two La and Zr double doped $Bi_2O_3$ samples are given in **Fig. 3.2.9**.

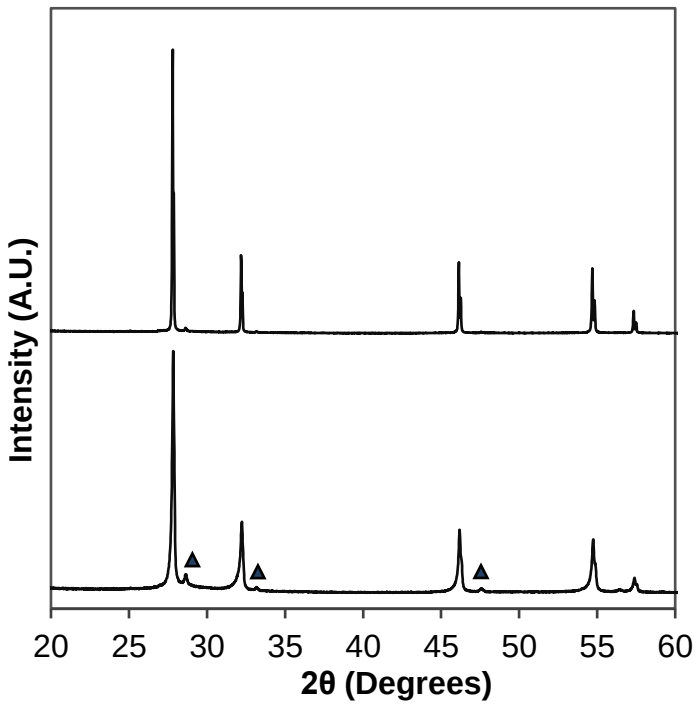


**Fig. 3.2.9**. Room temperature X-ray diffraction patterns of 10% La and Zr doped cubic $Bi_2O_3$ materials. The $La_2Zr_2O_7$ impurity phase is indicated with triangles.

The La7Zr3 composition possessed a relative ionic radius of 1.065Å and the

La5Zr5 composition had an ionic radius of 1.00Å. While there was a large variation in average dopant ionic radius, the La and Zr doped compounds produced the cubic phase. The main difference in phase, was at higher zirconium concentrations, there was a marked increase in $La_2Zr_2O_7$ impurity phase formation. Consequently, a substantial secondary phase is formed within the La5Zr5 composition.

Also the conductivity of both samples are measured. Overall, the La7Zr3 compound exhibited the highest conductivity of all $Bi_2O_3$ materials synthesized in this investigation. The Arrhenius behavior of the cubic La7Zr3 is compared to other oxygen ion conductors in **Fig. 3.2.10**.

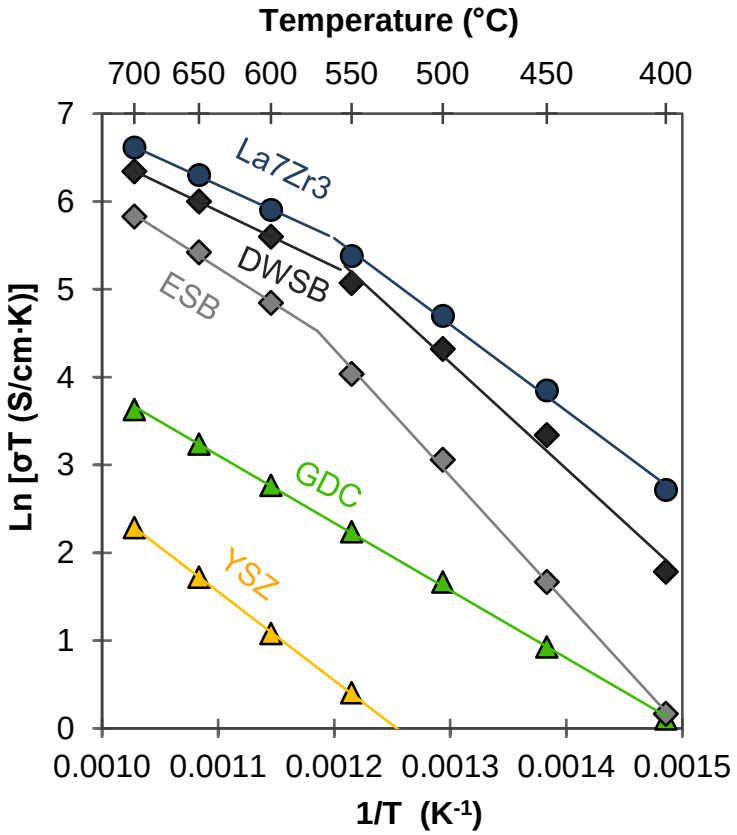


**Fig. 3.2.10**. Arrhenius plot of multiple SOFC electrolytes from 700°C to 400°C. The high temperature activation energy of the cubic La7Zr3 sample is 0.520 eV and the low temperature activation energy is 0.847 eV. Plot adapted from

The conductivity of La7Zr3 compound exceeds all other oxygen ion conducting materials developed to date. The conductivity of La7Zr3 is over 30% higher than DWSB at 650°C, which previously held the record for highest oxygen ion conductivity[8]. In fact, the cubic La7Zr3 material is the fastest oxygen ion conducting material ever developed. The superior conductivity of the La7Zr3 electrolyte would permit further increase in $Bi_2O_3$ layer thickness and reduction of the less conductive electrolyte layer (GDC, SNDC, etc.) to minimize the ohmic ASR of an SOFC without sacrificing OCV[73].

Like DWSB, the high conductivity in La7Zr3 was an outcome of lowering the total dopant concentration in $Bi_2O_3$, while also retaining the highly conductive cubic phase. The conductivity of La7Zr3 was improved beyond DWSB by reducing the total dopant concentration to 10%, providing a larger concentration of highly polarizable $Bi^{+3}$ in the lattice. Because the polarizability of bismuth is higher than the dopant cations, decreasing the total cation substitution increased the lattice polarizability, consequently allowing for greater oxygen ion mobility and facilitated anion diffusion[9,74]. Higher polarizability equates to larger cation charge separation and improved anion diffusion due to the reduction in coulombic repulsion that oxygen ions experience when moving through the saddle point of the conductivity pathway. The lanthanum cation has the largest ionic radius of all lanthanide series cations, and since the ionic radius is linearly related to polarizability, the large $La^{+3}$ cation is more polarizable than the other rare earth elements[9]. The La7Zr3 compound contained over four times more lanthanum than the La1.5Y8.5 sample for an equivalent dopant ionic radii.

The La7Zr3 composition was also aged at multiple temperatures to determine its stability. First, La7Zr3 was aged at intermediate temperatures (650°C) due to the high stability of cubic $Bi_2O_3$ at this temperature[14]. The aging performance of La7Zr3 at 650°C (**Fig. 3.2.11**) illustrates the high stability of the electrolyte at intermediate temperature.

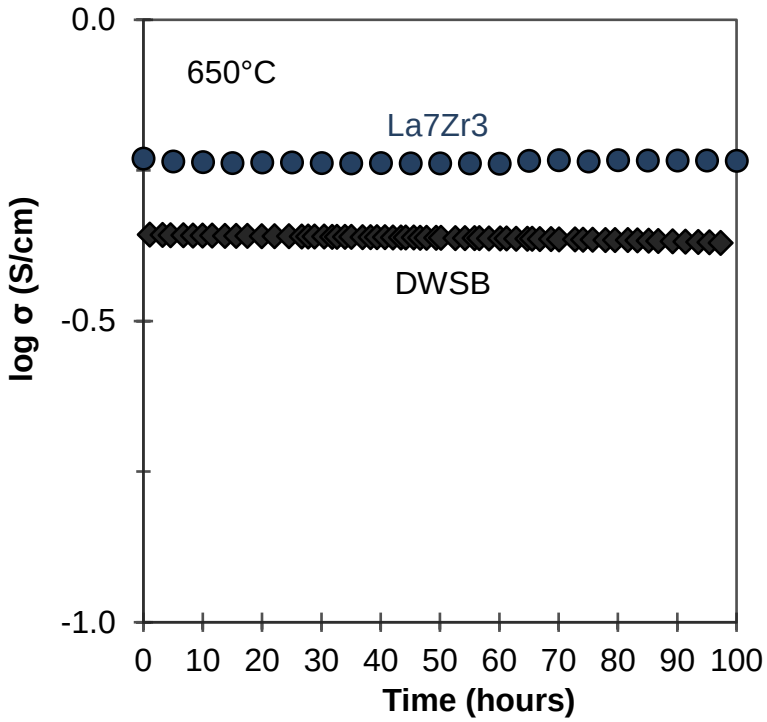


**Fig. 3.2.11**. Conductivity as function of aging time for La7Zr3 and DWSB at 650°C. The DWSB is plotted as a reference cubic bismuth oxide material[14].

At lower temperatures (<600°C), the conductivity of La7Zr3 is not as stable with time. While cubic $Bi_2O_3$'s generally display stable performance at intermediate temperature, degradation at lower temperatures is a problem for SOFCs operating below 650°C. In particular, anion ordering is most rapid in cubic $Bi_2O_3$ at 500°C[14]. To ensure the $Bi_2O_3$ electrolytes were capable of operation at low temperatures, the sample was aged for one hundred hours at 500°C. Both ESB and DWSB exhibit a sharp decay

in conductivity, due to the ordering of the oxygen ion sublattice[14]. The La7Zr3 compound meanwhile, had a much more gradual decay in conductivity as it was aged at 500°C (**Fig 3.2.11**).

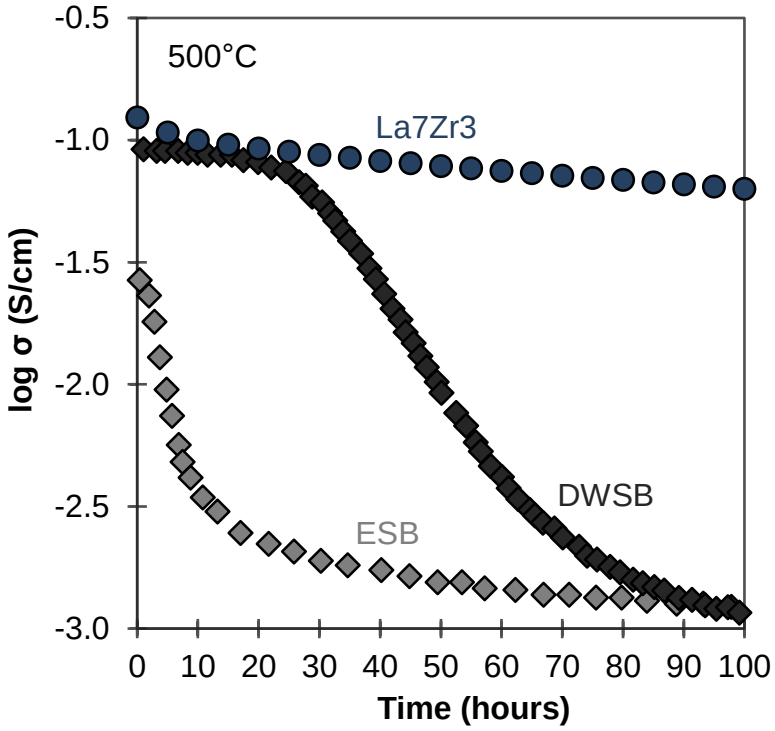


**Fig 3.2.11** Conductivity as function of aging time for La7Zr3, DWSB and ESB at 500°C. The DWSB and ESB samples are plotted as reference cubic oxide materials[14].

It has been reported that the disorder-order transition in $Bi_2O_3$ can be suppressed with aliovalent doping of $Zr^{+4}$ cations[75]. Thus, La7Zr3 may undergo a much slower aging phenomenon than other cubic bismuth oxide materials doped with rare earth cations. The decline in conductivity though, was likely exacerbated by phase instability at 500°C. After a 100 hour hold at 500°C, there was a growth in a $La_2Zr_2O_7$ secondary phase, which is illustrated by the room temperature XRD pattern of La7Zr3 before and after aging given in the supplemental section (**Fig 3.2.12**). The lower conductivity after

aging can in part be attributed to La and Zr dopants leaving the $Bi_2O_3$ solid solution to form the $La_2Zr_2O_7$ impurity phase.

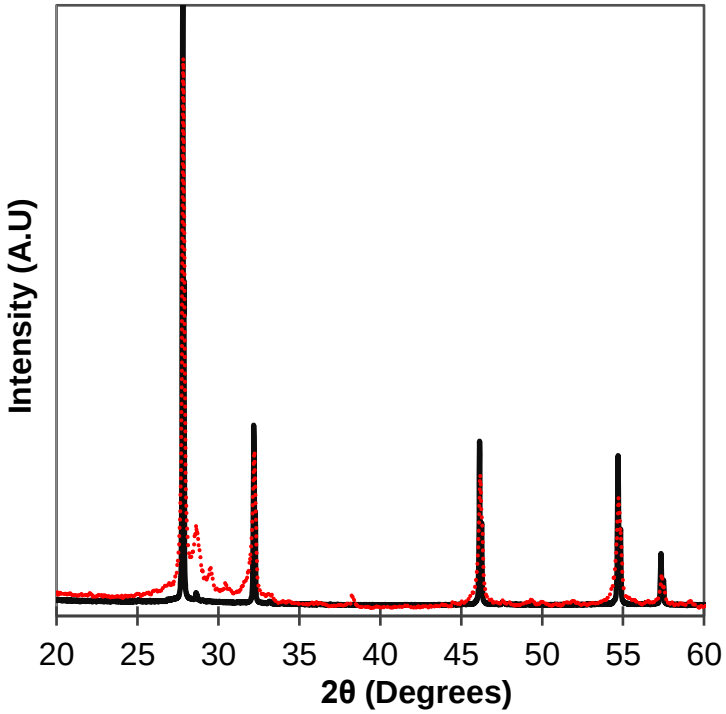


**Fig 3.2.12**. Room temperature X-ray diffraction pattern of cubic La7Zr3 before and after aging at 500°C for 100 hours. The black line is the initial XRD plot and the dashed line is after aging. The intensity of the secondary phase $La_2Zr_2O_7$ peaks grew after aging.

*3.3 Optimizing the Rhombohedral $Bi_2O_3$ Lattice for Maximum Conductivity*

As the La and Y doped $Bi_2O_3$ system was examined further, it became clear that the rhombohedral phase was a very promising electrolyte material for low temperature SOFCs. At a dopant concentration rate of 10%, the rhombohedral phase of bismuth oxide grew rapidly after the dopant radius was increased above approximately 1.05 Å. At a La and Y cation substitution rate of 3.6% and 6.4% respectively (La3.6Y6.4) the average dopant ionic radius was equal to approximately 1.07Å. At a dopant ionic radius of 1.07Å, XRD confirmed that the pure rhombohedral phase of $Bi_2O_3$ was present as

shown in the previous **Fig. 3.2.3**. As opposed to the cubic phase, the rhombohedral phase of bismuth oxide does not undergo an ordering of the oxygen vacancies at lower temperatures. By avoiding the ordering phenomena, the rhombohedral structure does not exhibit a large drop in conductivity. The stable conductivity of the rhombohedral phase is demonstrated in **Fig. 3.3.1** which is the aging of La3.6Y6.4 for sixty hours at 500°C compared to other cubic $Bi_2O_3$ samples.

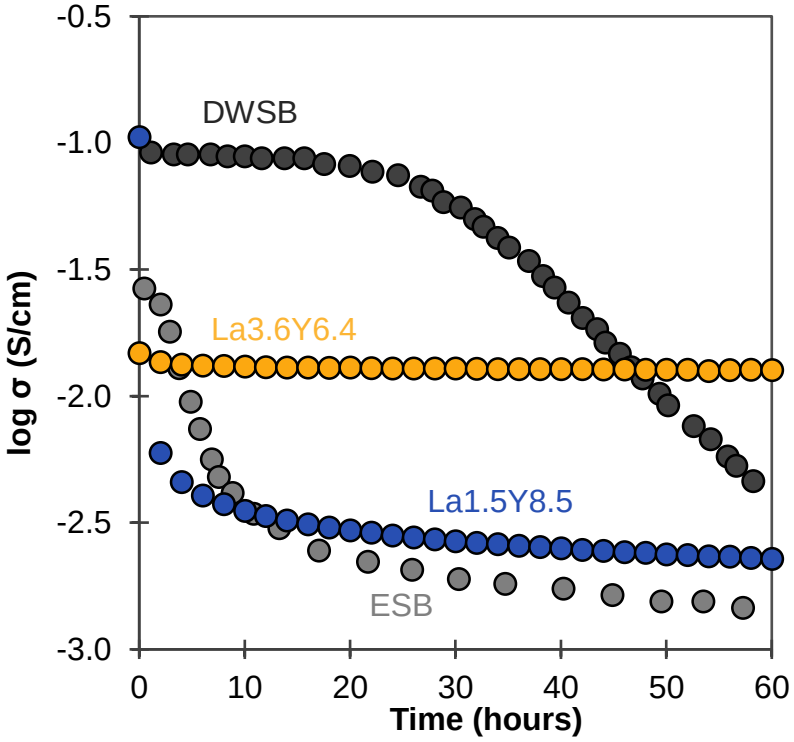


**Fig. 3.3.1**. Conductivity as function of aging time for four bismuth oxide samples at 500°C. The DWSB and ESB data is used as a reference and is taken from[18].

It is clear that conductivity of the rhombohedral La3.6Y6.4 sample is much more stable than the cubic La1.5Y8.5, ESB, and DWSB samples. Since it does not have a disorder-order transition, the rhombohedral phase does not incur a drop in conductivity when aged at 500°C. Not only is the conductivity of La3.6Y6.4 stable, but the rhombohedral phase is also thermodynamically stable. After sixty hours of aging at

500°C, the rhombohedral phase of La3.6Y6.4 does not break down. Furthermore, there is no growth of secondary phases that occur after aging. **Fig. 3.3.2** is the XRD pattern of La3.6Y6.4 before and after aging at 500°C for sixty hours. It is clear that the there is almost no change in the phase after aging.

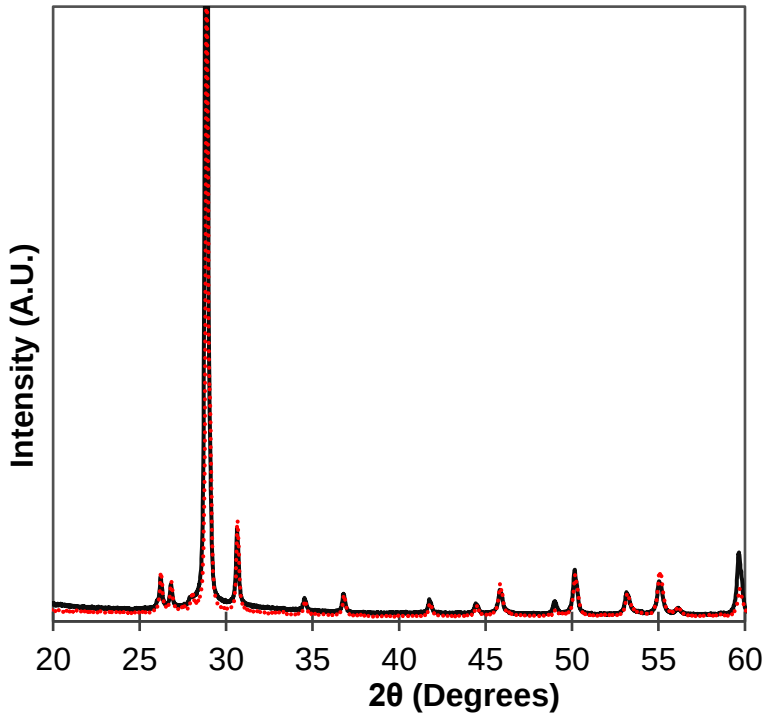


**Fig. 3.3.2**. Room temperature X-ray diffraction pattern of La3.6Y6.4 before and after aging at 500°C for 60 hours. The black line is the initial XRD plot and the dashed line is after aging.

Overall the phase of $Bi_2O_3$ was highly dependent on the ionic radius of the dopant. As the ionic radius increased, the amount of rhombohedral phase also increased. Furthermore, as the amount of rhombohedral phase increased, the stability of conductivity at 500°C increased. The correlation between dopant ionic radius, the phase of the material, and conductivity degradation after aging was determined by Rietveld refinement and Eq. 3.2.1. Rietveld refinement was carried out to determine the proportion of cubic phase and rhombohedral phase in each sample. Additionally,

Eq. 3.2.1 was used to evaluate the amount of conductivity degradation occurred after aging the samples for sixty hours at 500°C. The relationship between ionic radius, phase, and stability of conductivity for $Bi_2O_3$ is plotted in **Fig. 3.3.3**.

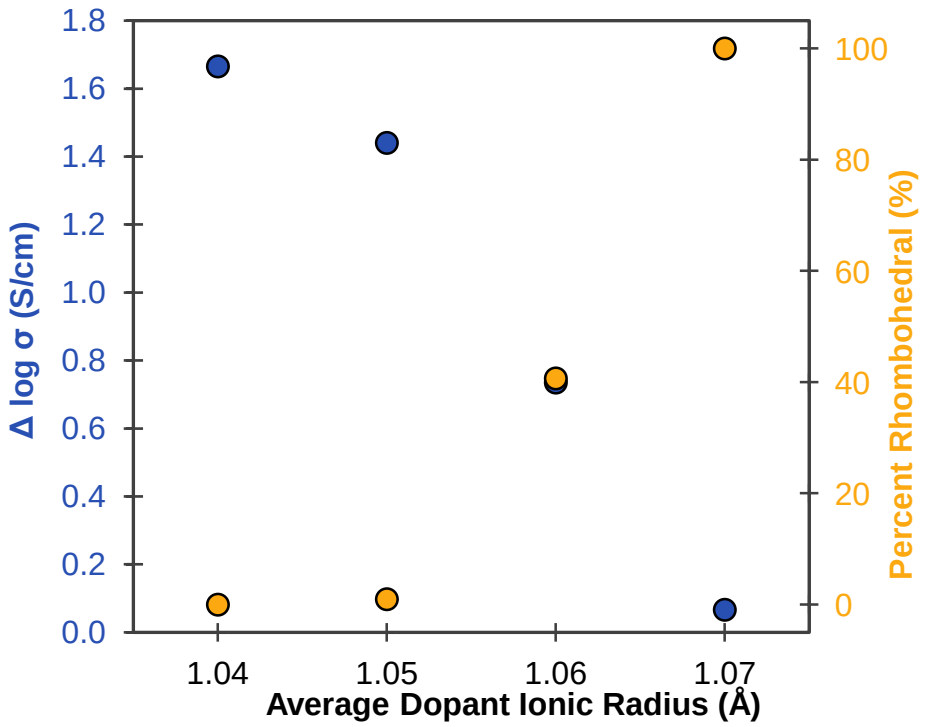


**Fig. 3.3.3**. Decay in conductivity (Eq. 3.2.1) vs. average dopant ionic radius for 10% La and Y doped $Bi_2O_3$ at 500°C. Plotted on the second axis is the rhombohedral/cubic phase percentage determined by room temperature XRD and Rietveld refinement.

The rhombohedral phase exhibited much better stability, but lower initial conductivity when compared to the cubic phase. Therefore, increasing the conductivity of the rhombohedral phase would make it even more viable as an SOFC electrolyte. As with the La and Y double doped cubic bismuth oxide study, the ratio of La to Y was varied to study the effect of average dopant radius on the conductivity. With a relative dopant ionic radius of 1.07Å, La3.6Y6.4 had the smallest ratio of lanthanum to yttrium that could stabilize the rhombohedral phase. Increasing the amount of $La^{+3}$ substitution and decreasing the amount of $Y^{+3}$ substitution tested the upper limits of the

rhombohedral phase stability. For a dopant concentration held constant at 10%, a relative dopant ionic radius from 1.07Å up to 1.14Å resulted in the formation of the rhombohedral phase of $Bi_2O_3$. Above 1.14Å, secondary phase formation occurred and caused a drop in conductivity. Below 1.07Å the formation of the cubic resulted in lower conductivity due to the ordering of the secondary cubic phase. Like La3.6Y6.4, all the La and Y double doped $Bi_2O_3$ samples in the rhombohedral phase had very stable conductivity for over sixty hours of aging time at 500°C. Overall the relative dopant ionic radius, and hence the lattice parameters of the rhombohedral $Bi_2O_3$ unit cell had very little impact on the conductivity of the material. The average dopant ionic radius and rhombohedral lattice volume vs conductivity is plotted in **Fig. 3.3.4**.

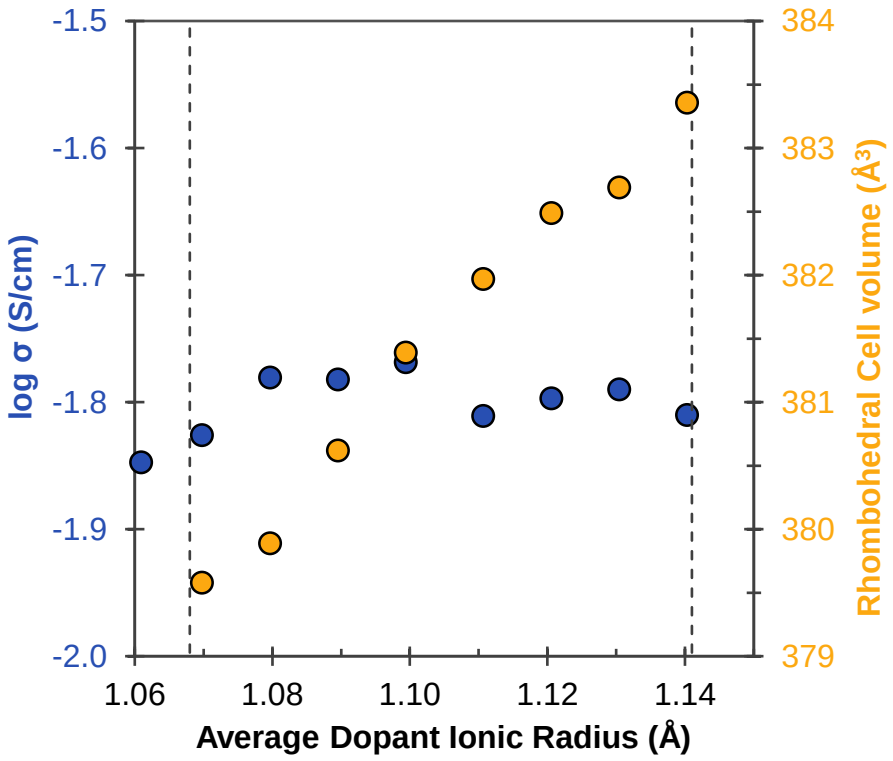


**Fig. 3.3.4**. Conductivity vs. relative dopant ionic radius in $Bi_2O_3$. Conductivity was measured after a two hour hold at 500°C. The dotted lines represent approximate stability window of the rhombohedral phase. The secondary vertical axis identifies the volume of the rhombohedral unit cell determined by Rietveld refinement.

While the lattice volume scales with dopant radius, the conductivity of the material is relatively constant over the entire stability window of the rhombohedral phase. Since the ionic radius of the dopant had very little effect on the conductivity of rhombohedral bismuth oxide, the total dopant concentration was lowered to improve performance. Like previous authors' work to decrease bismuth substitution in cubic $Bi_2O_3$ to increase conductivity, the amount of dopant in the rhombohedral phase was similarly carried out. **Fig. 3.3.5** illustrates the conductivity as a function of total dopant concentration in the rhombohedral $Bi_2O_3$ lattice.

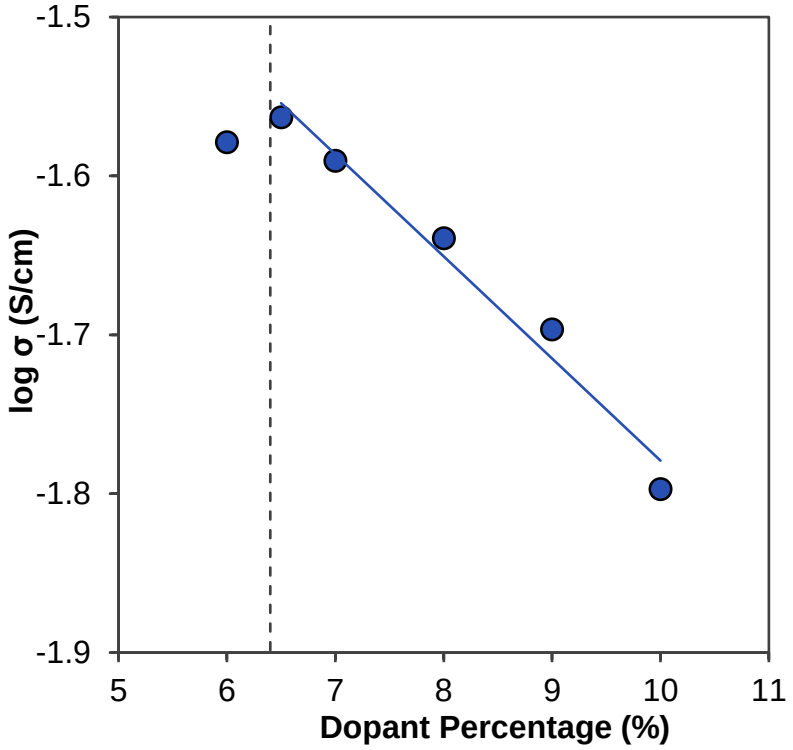


**Fig. 3.3.5**. Conductivity vs. total dopant concentration in rhombohedral $Bi_2O_3$. Conductivity was measured after a two hour hold at 500°C. The dashed line represents the approximate rhombohedral phase boundary determined by room temperature XRD. The solid line represents the linear fit of the data. Average dopant ionic radius is 1.12Å.

From the figure, it is clear the conductivity of the La and Y double doped bismuth oxide material increased as the dopant concentration decreased. The linear

trend of increasing conductivity with decreasing dopant concentration held true all the way up to the rhombohedral phase boundary. When the dopant level was dropped below approximately 6.5%, the tetragonal secondary phase began to form for the La and Y double doped $Bi_2O_3$ system with a relative ionic radius of 1.12 Å. The secondary phase formation resulted in a decrease of conductivity in the material. Thus, a maximum conductivity was recorded at a substitution rate of 6.5% which corresponded to the sample La4.7Y1.8. Less substitution of trivalent cations into the $Bi_2O_3$ network increased the concentration of the highly polarizable $Bi^{+3}$ cation. The improvement in conductivity therefore resulted from the increased polarizability of the cation network. The lone pair of electrons on the $Bi^{+3}$ cation in conjunction with its loose bonding with surrounding disordered oxygen ions makes a particularly favorable environment for fast $O^{-2}$ transport.

With the phase stability window mapped out for the low dopant regime of La and Y doped $Bi_2O_3$ rhombohedral phase, it was necessary to also examine the phase stability at elevated temperatures. High temperature X-ray diffraction was performed on La5.1Y1.4 to determine the phase stability of the rhombohedral phase at elevated temperatures. La5.1Y1.4 was chosen because of its high conductivity. The X-ray diffraction patterns were recorded from room temperature up to 700°C to determine if there were any phase transitions that occurred in the material. The plot of XRD patterns taken every ten degrees from 550°C to 600°C is laid out in **Fig. 3.3.6**. From this figure there is a sharp peak shift between 580°C and 590°C. By fitting the XRD patterns it was determined that the shift in peaks was a result of the low temperature rhombohedral phase transforming to the cubic phase.

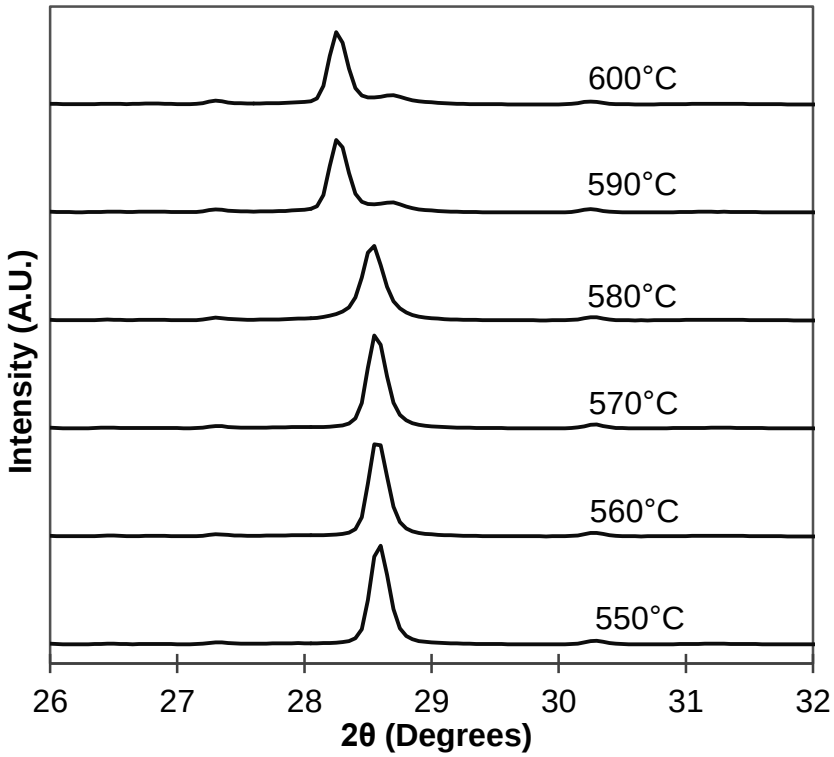


**Fig. 3.3.6**. High temperature X-ray diffraction of La5.1Y1.4. The temperature of each scan is indicated on the plot. The phase transition can be observed above 580°C.

From room temperature up to approximately 580°C the La5.1Y1.4 sample exhibits the pure rhombohedral phase. Above 580°C the cubic phase forms and grows while the rhombohedral phase shrinks. Once the temperature reaches 700°C, the La5.1Y1.4 sample is entirely cubic. The phase transformation at high temperature is problematic for the low dopant rhombohedral phase. Since the cubic phase has issues with ordering, operating a fuel cell above the phase transition of the rhombohedral to cubic phase could cause instability. Since the phase transition occurs around 580°C, the rhombohedral phase should be maintained at or below 550°C. The conductivity of the La5.1Y1.4 sample was measured as a function of time for multiple temperatures and is plotted in **Fig. 3.3.7**.

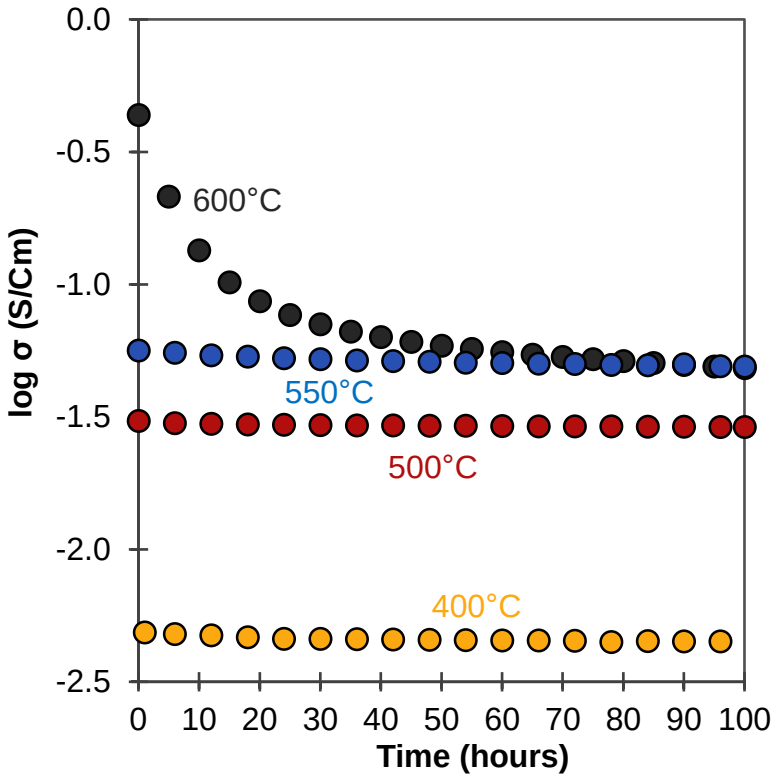


**Fig. 3.3.7**. Conductivity as a function of aging time for the La5.1Y1.4 rhombohedral sample. The aging temperature is listed on the plot.

While the conductivity of La5.1Y1.4 sample was stable from 400°C through 550°C, at 600°C there was a large decay in conductivity. The initial conductivity at 600°C was relatively high, but it quickly fell off. Because the cubic phase forms at 600°C, it boosts the initial conductivity of the material, but also causes degradation. Like the La1.5Y8.5 sample that was discussed earlier, the cubic phase present at 600°C in the La5.1Y1.4 undergoes an ordering of the oxygen ion sublattice and subsequent decay in conductivity. The low overall dopant concentration of La5.1Y1.4 leads to faster kinetics of ordering and thus a more rapid decay in conductivity than would be observed in ESB. Since the phase stability window of the rhombohedral phase has been mapped out in terms of dopant ionic radius, the total dopant concentration and the

temperature, it was next important to identify what type of cation substitution maximized the conductivity.

While minimizing total dopant concentration is a key component of increasing ionic conductivity of rhombohedral $Bi_2O_3$, the type of substituted cation is also an important consideration. A variety of other dopants were selected to study their effect on the conductivity of rhombohedral bismuth oxide. For this investigation, the average dopant radius was set between 1.095Å and 1.12Å to remain sufficiently within the rhombohedral phase boundary. For this investigation a single cation was selected if it was between these bounds, otherwise yttrium was used as a secondary dopant to decrease the relative dopant radius. Furthermore, the dopant concentration was held constant at 8% to ensure high conductivity. **Fig. 3.3.8** depicts the conductivity of the rhombohedral bismuth oxide material as a function of primary cation dopant.

It can be seen from the figure that substitution with $La^{+3}$ provides a peak in conductivity. The two lanthanum double doped materials exhibited higher conductivity than the calcium, strontium, neodymium, or samarium doping. The peak in conductivity is likely a product of lanthanum possessing the largest ionic radius of the trivalent cations. Other authors have observed that substituting larger cations in to the rhombohedral bismuth oxide framework increases conductivity[33,35]. The larger ionic radius widens the conduction pathway and allows for greater oxygen ion mobility. The investigation also demonstrated that trivalent cation substituted $Bi_2O_3$ samples had greater conductivity than the divalent cation substitutions. The lower conductivity of the divalent substitution may have been caused by alterations in the defect structure.

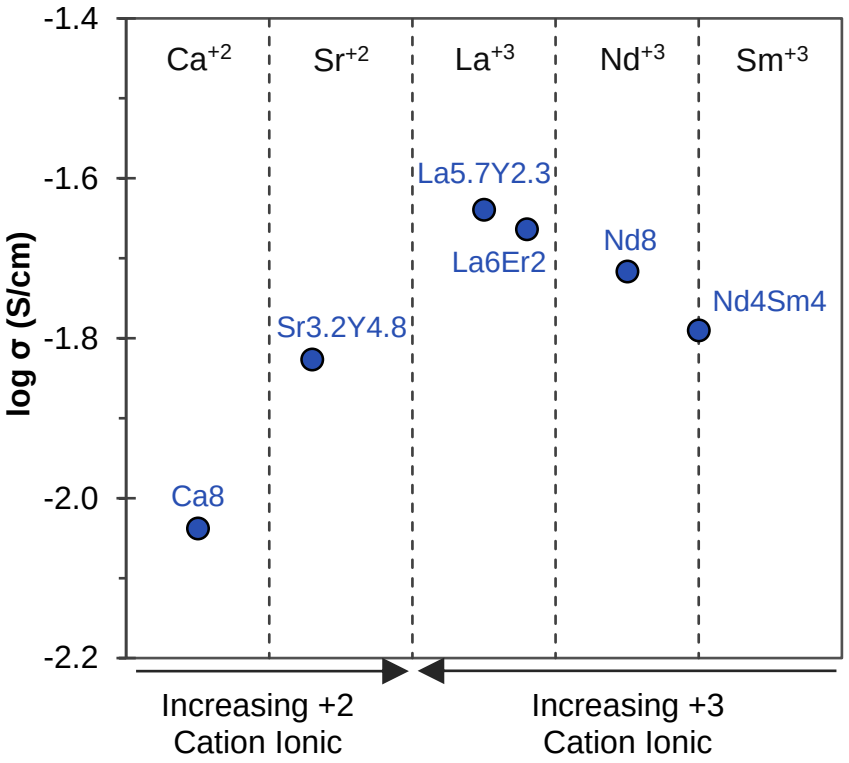


**Fig. 3.3.8**. Conductivity of multiple rhombohedral $Bi_2O_3$ samples measured at 500°C. Divalent cation substituted $Bi_2O_3$ samples are located on the left side and trivalent cations substitution is on the right. The ionic radius of the primary dopant increases toward the center. Each sample is labeled on the plot.

Doping $Ca^{+2}$ in to the $Bi^{+3}$ site would result in additional negative charge from the aliovalent substitution. The charge imbalance would need to be compensated with additional positive charge, such as decreased oxygen vacancies. A reduction in oxygen vacancies would bring about fewer jumping sites for oxygen ions and cause a decrease in ionic conductivity. Ultimately using lanthanum in a double doping scheme allowed for higher conductivity in a low dopant regime. With an ionic radius of 1.16Å, $La^{+3}$ was too large to stabilize the rhombohedral phase at low dopant regimes. Substituting a smaller secondary cation into the lanthanum doped $Bi_2O_3$ lattice resulted in a lower relative dopant ionic radius. Thus, a La-doped rhombohedral phase could form at lower

dopant concentrations than would be possible otherwise due to double doping. Thus, the conductivity of rhombohedral bismuth oxide was maximized by decreasing the total cation substitution as well as widening the conduction pathways by doping large trivalent cations. Ultimately the La5.1Y1.4 sample exhibited the highest conductivity of any rhombohedral $Bi_2O_3$ sample. The La5.1Y1.4 contained both the large cation $La^{+3}$ and a low total dopant concentration.

The La and Y double doped $Bi_2O_3$ samples exhibited the highest conductivity of all rhombohedral samples tested. To ensure this material would be an appropriate ion conducting electrolyte, the ratio of the ionic conduction to electronic conduction was measured. The electrical potential generated from an oxygen ion conductor in a two gas environment was used to determine the ionic transference number. The La5.1Y1.4 sample was made into a disc with silver electrodes and sealed between two different $PO_2$ environments. The symmetric cell was held for an hour at each condition before the OCP was measured and EIS was performed. The ionic transference number was calculated using Eq. 3.3.1, as detailed by other authors[76].

$$T_i = 1 - \frac{R_b}{R_T}\left(1 - \frac{V_{OC}}{V_N}\right) \qquad \text{(Eq. 3.3.1)}$$

In this equation $R_b$ = bulk resistance, $R_T$ = total resistance, $V_{OC}$ = open circuit potential, and $V_N$ = Nernst potential. The voltage measurement as a function of $PO_2$ for La5.1Y1.4 is given in **Fig. 3.3.9 a** and the impedance of the cell taken at different $PO_2$ values is plotted in **Fig. 3.3.9 b**. All measurements were recorded at 500°C. Overall the La5.1Y1.4 sample exhibited an average ionic transference number greater than 0.997 across the entire $PO_2$ range that was measured.

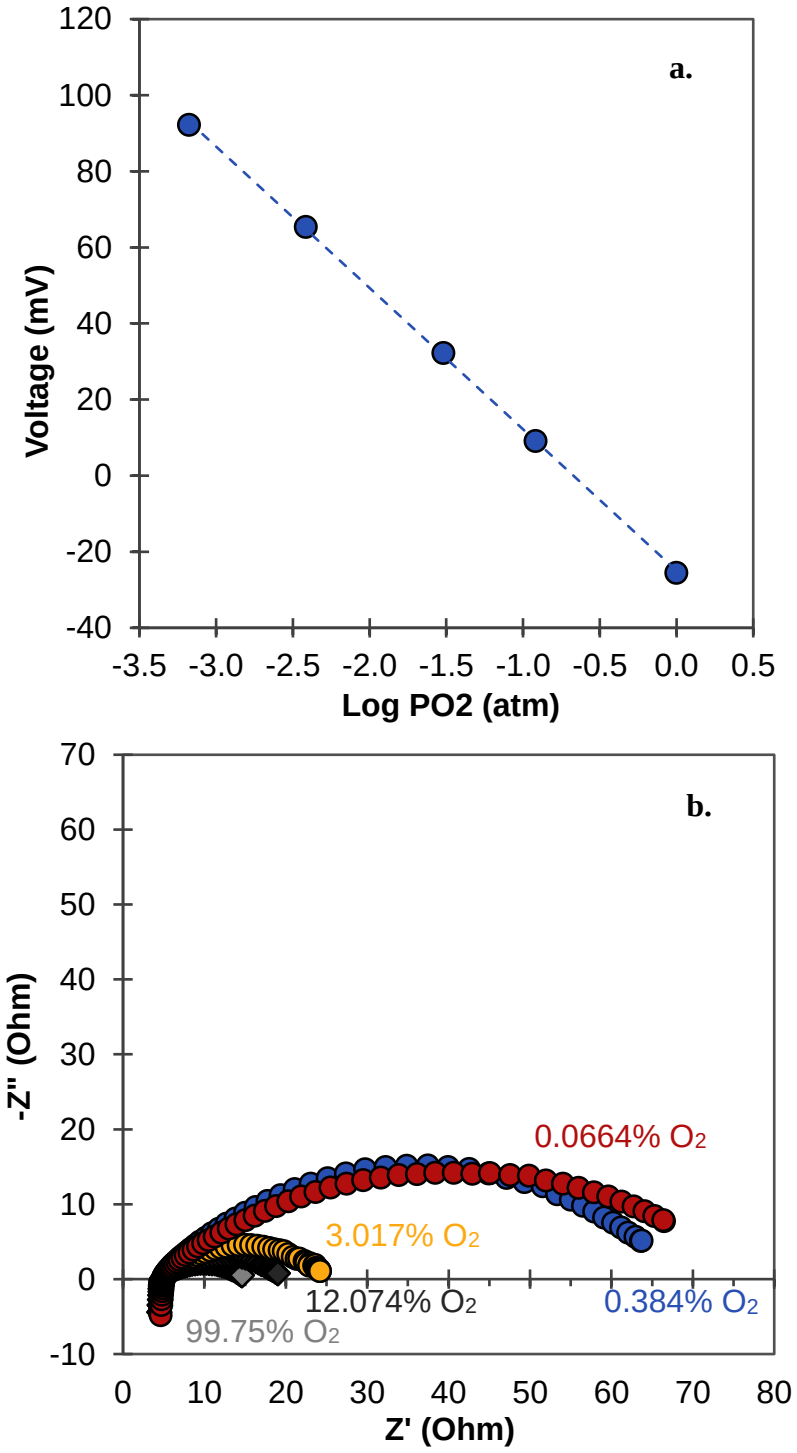


**Fig. 3.3.9 a**. Voltage as function of "anode" $PO_2$ supplied to the La5.1Y1.4 symmetric cell at 500°C. The "cathode" side was steadily supplied with air. **b**. EIS plot of the La5.1Y1.4 symmetric cell at 500°C. The atmosphere suppled to the "anode" side is indicated by the oxygen concentration on the plot. The "cathode" side was steadily supplied with air.

The measured voltage, the bulk resistance, total resistance and calculated ionic transference number for different $PO_2$ values is tabulated in **Table 3.3.1**.

| $PO_2$ (atm.) | Voltage (mV) | $R_b$ (ohm) | $R_t$ (ohm) | Transference number |
|---|---|---|---|---|
| 0.9975 | -25.464 | 4.70 | 15.16 | 0.9942 |
| 0.12074 | 9.159 | 4.75 | 19.72 | 0.9985 |
| 0.030168 | 32.266 | 4.78 | 25.40 | 0.9997 |
| 0.0038394 | 65.419 | 4.80 | 68.03 | 0.9987 |
| 0.0006636 | 92.262 | 4.90 | 77.02 | 0.9976 |

**Table 3.3.1**. Voltage measurement, bulk resistance, total resistance and calculated transference number (Eq. 3.3.1) for the La5.1Y1.4 sample over a range of $PO_2$ values. The $PO_2$ value refers to the atmosphere on the "anode" of the La5.1Y1.4 sample. The "cathode" side is exposed to air.

To be a suitable electrolyte in an SOFC, an oxygen conductor must have high and stable ionic conductivity, but it also must be able to block electrons. If the electrolyte conducted electrons, the OCV and operating voltage would both be low and the cell would have poor power density. There was some small variability in the transference number measurements over the entire $PO_2$ range, thought it was likely due to small experimental errors. Overall the transference number approached unity, confirming that the La and Y double doped rhombohedral $Bi_2O_3$ is a pure ion conductor. After verifying the ionic conduction of the La and Y doped rhombohedral bismuth oxide, it was necessary to compare its conductivity to other prominent SOFC electrolytes. The Arrhenius behavior compared to other prominent oxygen ion conductors and bismuth oxide electrolytes is presented in **Fig. 3.3.10**.

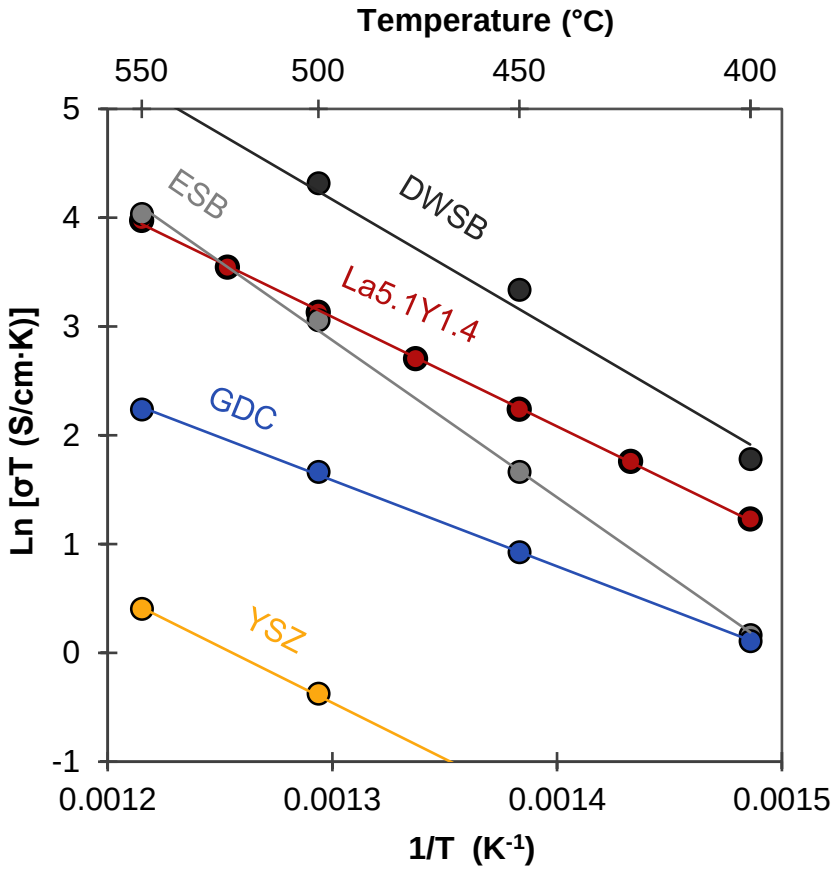


**Fig. 3.3.10**. Arrhenius plot of multiple SOFC electrolytes from 550°C to 400°C. The activation energy of the La5.1Y1.4 sample is 0.867 eV. Adapted from[7].

It is clear that ionic conductivity of La5.1Y1.4 is higher than traditional electrolytes such as GDC and YSZ, and comparable to ESB over the stability range of the rhombohedral phase. Only DWSB has higher conductivity over the entire temperature range. The rhombohedral $Bi_2O_3$ though has much lower activation energy when compared to the cubic $Bi_2O_3$ samples. Since the ESB and DWSB are in the ordered state in this temperature range, the mobility of the oxygen ions is much lower. What makes the La5.1Y1.4 sample a superior and more reliable oxygen ion conducting material at intermediate temperatures though, is its stable performance. **Fig. 3.3.11**

illustrates the degradation of conductivity in La5.1Y1.4, ESB, and DWSB samples as a function of aging time at 500°C.

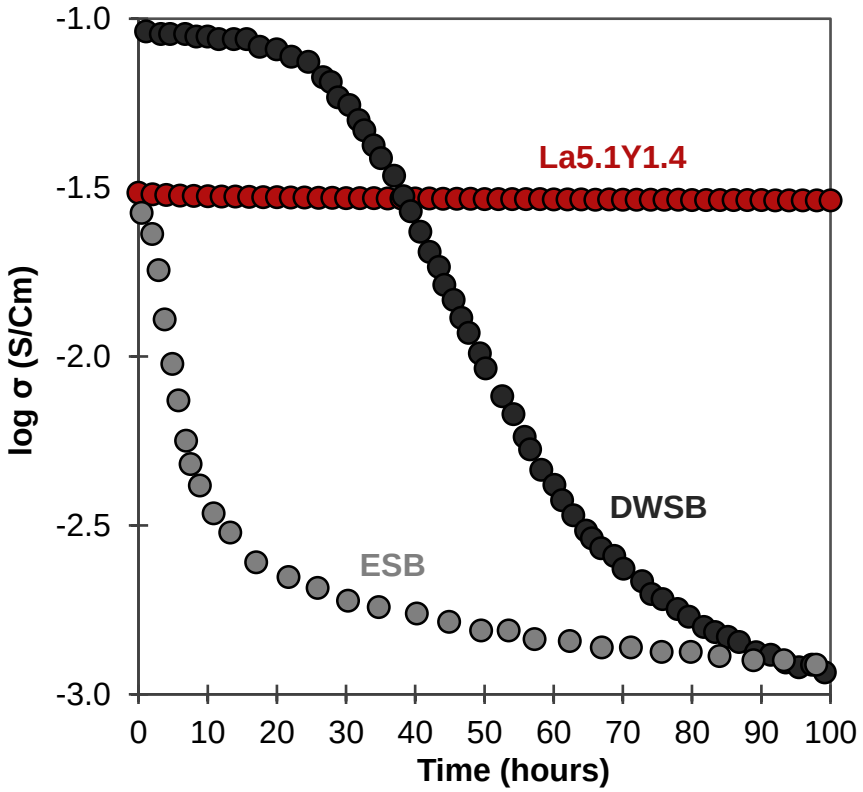


**Fig. 3.3.11**. Conductivity as function of aging time for La5.1Y1.4, ESB and DWSB as a function of aging time at 500°C. The DWSB and ESB data is used as a reference and is taken from[18].

The La5.1Y1.4 sample exhibited no appreciable decay for the entire hold at 500°C, while both ESB and DWSB experienced over an order of magnitude drop in conductivity. With high ionic conductivity, low electronic conductivity, and stable performance, the rhombohedral La and Y doped $Bi_2O_3$ is a good SOFC electrolyte candidate. Furthermore, the rhombohedral phase of bismuth oxide in general is a promising SOFC electrolyte due to its flexibility. The rhombohedral phase of $Bi_2O_3$ can be formed using a variety of different dopants. With a large range of potential

chemistries, rhombohedral bismuth oxide can be optimized and tailored for specific traits. The La5.1Y1.4 sample was optimized to produce the highest conductivity at 500°C, but other attributes could be examined further. With a large phase boundary, there are many options to explore. Utilizing either divalent or trivalent cations with sufficient ionic radius should be sufficient in stabilizing the rhombohedral phase. **Fig. 3.3.12** is a partial phase diagram of bismuth oxide that highlights the stability range of the rhombohedral phase.

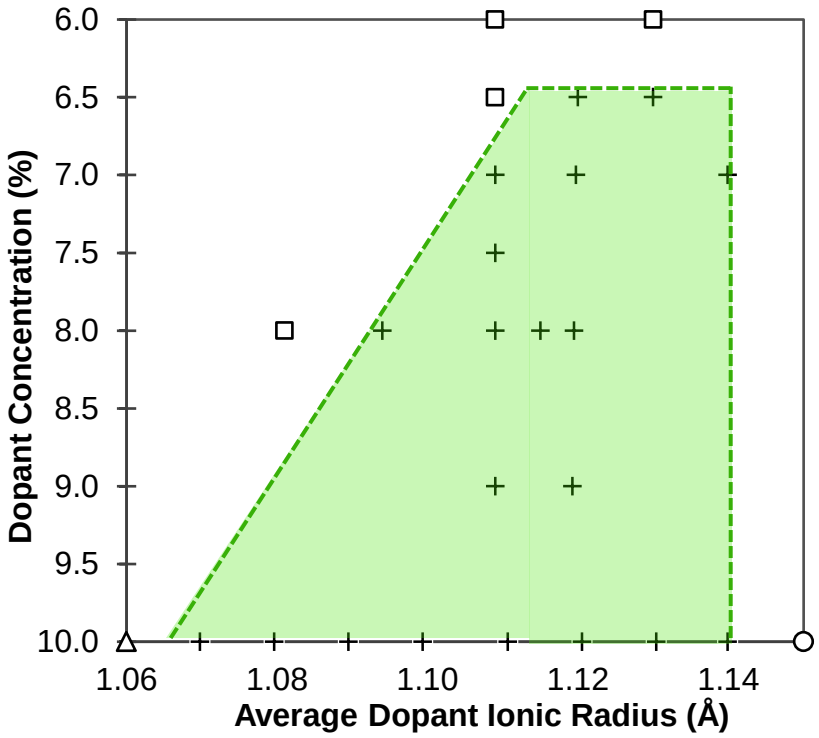


**Fig. 3.3.12**. Approximate phase stability window of rhombohedral $Bi_2O_3$ (dotted lines) given as function of total dopant concentration and average dopant ionic radius. The plus symbols indicate $Bi_2O_3$ compositions that are entirely rhombohedral, triangles are a rhombohedral/cubic mixture, squares indicate a rhombohedral/tetragonal mixture, and circles represent a rhombohedral/monoclinic mixture.

The rhombohedral phase of bismuth oxide included a large possible array of dopant ionic radius and dopant concentrations. While an exhaustive set of samples were not synthesized and characterized to construct and exact phase diagram of $Bi_2O_3$, the

approximate stability window of the rhombohedral phase is helpful for crafting the most highly conductive electrolytes. At lower dopant concentrations, bismuth oxide electrolytes are more conductive. Therefore, rhombohedral bismuth oxide samples that exist within the top of the plot should exhibit the highest conductivity. Ultimately using a trivalent cation substitution rate of approximately 6.5% and an average dopant ionic radius of around 1.125 Å should provide the highest conductivity among rhombohedral bismuth oxide. The Rietveld refinement and conductivity of all samples in the phase diagram are listed in **Table 3.3.2**.

| Name | Composition | Dopant Ionic Radius (Å) | Secondary Phase | Lattice Parameter a (Å) | Lattice Parameter c (Å) |
|---|---|---|---|---|---|
| La2.9Y7.1 | $Bi_{0.9}La_{0.029}Y_{0.071}O_{1.5}$ | 1.06 | Cubic | 3.95902(17) | 27.90979(63) |
| La3.6Y6.4 | $Bi_{0.9}La_{0.036}Y_{0.064}O_{1.5}$ | 1.07 | None | 3.96255(13) | 27.9143(10) |
| La4.3Y5.7 | $Bi_{0.9}La_{0.043}Y_{0.057}O_{1.5}$ | 1.08 | None | 3.96423(17) | 27.9131(14) |
| La5Y5 | $Bi_{0.9}La_{0.05}Y_{0.05}O_{1.5}$ | 1.09 | None | 3.96677(11) | 27.9314(9) |
| La5.7Y4.3 | $Bi_{0.9}La_{0.057}Y_{0.043}O_{1.5}$ | 1.10 | None | 3.96890(11) | 28.0581(8) |
| La6.5Y3.5 | $Bi_{0.9}La_{0.065}Y_{0.035}O_{1.5}$ | 1.11 | None | 3.96929(12) | 27.9932(9) |
| La7.2Y2.8 | $Bi_{0.9}La_{0.072}Y_{0.028}O_{1.5}$ | 1.12 | None | 3.96901(19) | 28.0366(15) |
| La7.9Y2.1 | $Bi_{0.9}La_{0.079}Y_{0.021}O_{1.5}$ | 1.13 | None | 3.9686(2) | 28.0575(17) |
| La8.6Y1.4 | $Bi_{0.9}La_{0.086}Y_{0.014}O_{1.5}$ | 1.14 | None | 3.97037(21) | 28.0810(51) |
| La9.3Y0.7 | $Bi_{0.9}La_{0.093}Y_{0.007}O_{1.5}$ | 1.15 | Monoclinic | 3.97095(21) | 28.0810(15) |
| La6.4Y2.6 | $Bi_{0.91}La_{0.064}Y_{0.026}O_{1.5}$ | 1.12 | None | 3.97017(13) | 28.0401(10) |
| La5.7Y2.3 | $Bi_{0.92}La_{0.057}Y_{0.023}O_{1.5}$ | 1.12 | None | 3.96875(12) | 28.0575(10) |
| La5Y2 | $Bi_{0.93}La_{0.05}Y_{0.02}O_{1.5}$ | 1.12 | None | 3.96515(13) | 28.1061(10) |
| La4.7Y1.8 | $Bi_{0.935}La_{0.047}Y_{0.018}O_{1.5}$ | 1.12 | None | 3.96712 | 28.0789 |
| La5.1Y1.4 | $Bi_{0.935}La_{0.051}Y_{0.014}O_{1.5}$ | 1.13 | None | 3.9672(2) | 28.1539(17) |
| La4.3Y1.7 | $Bi_{0.94}La_{0.043}Y_{0.017}O_{1.5}$ | 1.13 | Tetragonal | 3.96743(10) | 28.1680(8) |
| La6Y1 | $Bi_{0.93}La_{0.06}Y_{0.01}O_{1.5}$ | 1.14 | None | 3.96902(12) | 28.1238(9) |

| | | | | | |
|---|---|---|---|---|---|
| La6Er2 | $Bi_{0.92}La_{0.06}Er_{0.02}O_{1.5}$ | 1.12 | None | 3.96810(19) | 28.0633(14) |
| Nd9 | $Bi_{0.91}Nd_{0.09}O_{1.5}$ | 1.11 | None | 3.9675(1) | 27.964(1) |
| Nd8 | $Bi_{0.92}Nd_{0.08}O_{1.5}$ | 1.11 | None | 3.9662(2) | 28.010(1) |
| Nd7.5 | $Bi_{0.925}Nd_{0.075}O_{1.5}$ | 1.11 | None | 3.9649(2) | 28.044(1) |
| Nd7 | $Bi_{0.93}Nd_{0.07}O_{1.5}$ | 1.11 | None | 3.9648(2) | 28.055(1) |
| Nd6.5 | $Bi_{0.935}Nd_{0.065}O_{1.5}$ | 1.11 | Tetragonal | 3.9631(2) | 28.070(1) |
| Nd6 | $Bi_{0.94}Nd_{0.06}O_{1.5}$ | 1.11 | Tetragonal | 3.9622(2) | 28.0901(9) |
| Nd4Sm4 | $Bi_{0.92}Nd_{0.04}Sm_{0.04}O_{1.5}$ | 1.095 | None | 3.96375(10) | 27.9842(7) |
| Nd4Gd4 | $Bi_{0.92}Nd_{0.04}Gd_{0.04}O_{1.5}$ | 1.08 | Tetragonal | 3.9648(4) | 28.011(3) |
| Ca8 | $Bi_{0.92}Ca_{0.08}O_{1.5}$ | 1.12 | None | 3.95211(13) | 27.94928(79) |
| Sr3.2Y4.8 | $Bi_{0.92}Sr_{0.032}Y_{0.048}O_{1.5}$ | 1.115 | None | 3.95718(12) | 28.03506(94) |

**Table 3.3.2**. Rhombohedral $Bi_2O_3$ compositions, average dopant ionic radius, secondary phase, and lattice parameters based on Rietveld refinement and the Le Bail method. Lattice parameters relate to the R-3m space group of the rhombohedral lattice. The lattice parameters of the secondary phase is not included.

Overall the rhombohedral lattice showed promise as an SOFC electrolyte for intermediate temperature operation. It had high ionic conductivity, low electronic conductivity, and good stability at 500°C. While the La5.1Y1.4 sample exhibited the highest stable conductivity at 500°C, the partial phase diagram of bismuth oxide and the host of rhombohedral samples synthesized demonstrates that a large variation in chemistry is possible. Ultimately the La5.1Y1.4 sample is a promising intermediate temperature SOFC electrolyte due to its high and stable conductivity at 500°C.

# Chapter 4: Doping NASICON to Increase Conductivity

## *4.1 Motivation*

When considering batteries for grid-level storage, sodium-ion batteries have been shown to have a more viable and lower cost alternative to lithium-ion batteries[44–46]. Specifically using a ceramic $Na_3Zr_2Si_2PO_{12}$ (NASICON) electrolyte in an all solid-state battery design has been demonstrated to be a safer, less expensive, and more reliable than other sodium battery chemistries[47,48]. Although NASICON is safer than liquid electrolytes, its ionic conductivity is an order of magnitude lower than many organic electrolytes and is thus less appealing as an electrolyte[57]. The main objective of this research is to enhance the room temperature conductivity of NASICON sufficiently to operate a high-performance room temperature solid-state battery. To increase the conductivity of NASICON, modifications of the structure will be carried out and interpreted to ultimately optimize the material properties and improve $Na^+$ transport through the lattice. Much of the analysis focused on understanding the effect of doping on the bulk properties of NASICON rather than its effect on microstructure.

## *4.2 The Effect of Aliovalent Cation Substitution on NASICON Structure*

As discussed previously, structural investigations on doping the NASICON lattice have been done, but most of the work was focused on the microstructure. The work described here delves more into how the lattice is modified by lattice substitution on $Na_3Zr_2Si_2PO_{12}$ rather than the microstructural changes that occur. Although the

microstructure was detailed, the effect of doping on the phase transition from rhombohedral to monoclinic and changes in NASICON composition was the primary focus.

For this study, a host of divalent and trivalent cations were substituted for the $Zr^{+4}$ cation in the $Na_3Zr_2Si_2PO_{12}$ structure. The objective was to determine the effect of dopant ionic radius and valance on the phase of NASICON. To begin with, the zirconia octahedrons in NASICON have a coordination number of six, so at the very least all the potential dopant cations must support a six-fold coordination. Furthermore, the lower valance of the dopants generates a charge imbalance that must be compensated. Since there are vacant sodium sites in the NASICON structure, charge neutrality was obtained by filling the vacant sites with additional sodium ions. Overall the dopants were selected by their oxidation state and ionic radius to ensure a spectrum of ionic radii and overall lattice sodium content. The smallest coordination six ionic radius dopant was $Al^{+3}$ (0.535 Å) and largest ionic radius dopant was $Y^{+3}$ (0.90 Å). Ultimately the nominal stoichiometry of the NASICON materials had the following compositions: $Na_{3.2}Zr_{1.8}M_{0.2}Si_2PO_{12}$ ($M=Al^{3+}$, $Fe^{3+}$, $Y^{3+}$), and $Na_{3.4}Zr_{1.8}M_{0.2}Si_2PO_{12}$ ($M=Co^{2+}$, $Ni^{2+}$, $Zn^{2+}$).

After all the materials were synthesized, room temperature x-ray diffraction was carried out to determine purity and lattice parameters of each sample. The room temperature XRD patterns of each sample is given in **Fig. 4.2.1**. The Rietveld fit confirmed that all samples exhibited greater than 90% purity. Monoclinic $ZrO_2$ was an impurity observed in all prepared samples, but this is a common secondary phase found

in all types of NASICON synthesis[70,77,78]. The absence of a dopant containing secondary phase reinforces a successful substitution for the zirconium site.

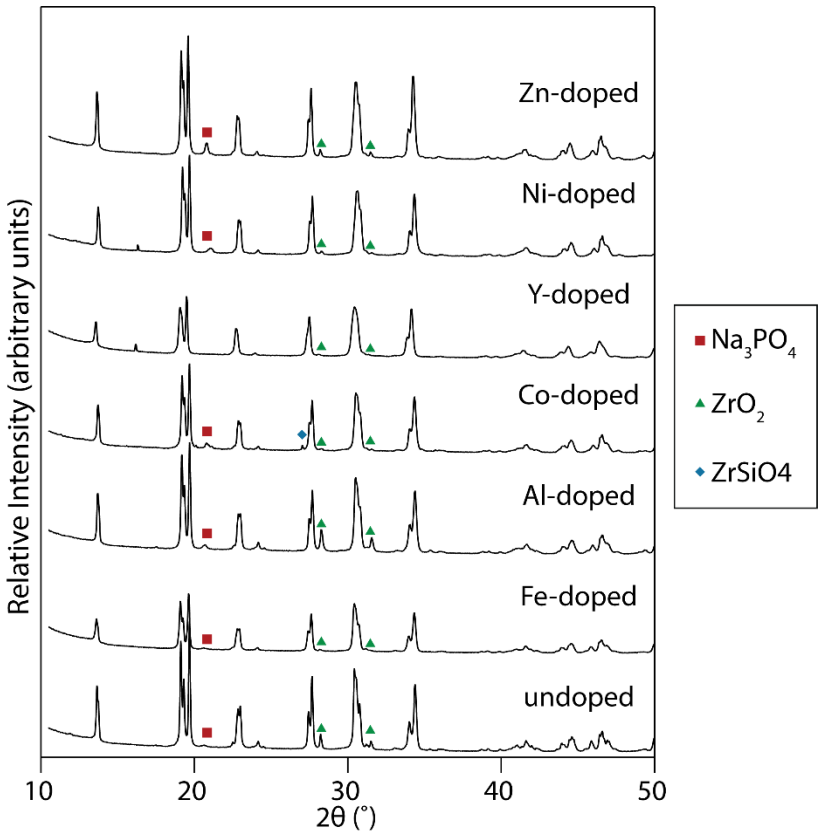


**Fig. 4.2.1**. Room temperature XRD pattern of all 10% doped NASICON samples. Rectangles, triangles, and diamonds representing $Na_3PO_4$, monoclinic $ZrO_2$, and $ZrSiO_4$ secondary phases respectively. All unlabeled peaks represent monoclinic $Na_3Zr_2Si_2PO_{12}$.

Furthermore, WDS was performed on all the NASICON samples to provide an elemental configuration. In general, the actual composition of each sample was close to the nominal stoichiometry. The elemental analysis of all samples as well as room temperature lattice parameters determined by Rietveld refrainment are provided in **Table 4.2.1**. Of all the samples, only the Y doped sample showed noticeably lower dopant levels than the intended stoichiometry. $Y_2O_3$ is generally stable at elevated temperatures so volatilization of the species is unlikely. Therefore, the lower amount

of yttrium could be an artifact of the peak overlap present between phosphorus and yttrium in the WDS. The phosphorus content of the Y-doped NASICON is much higher than the rest of the samples, reinforcing the likelihood of peak overlap causing an inaccurate reading of both species.

| Sample | a (Å) | b (Å) | c (Å) | beta (°) | Stoichiometry |
|---|---|---|---|---|---|
| Undoped | 15.63638 | 9.048573 | 9.220053 | 123.6849 | $Na_{2.99}Zr_{2.03}Si_{2.07}P_{0.92}O_{12}$ |
| Al-doped | 15.66292 | 9.0589967 | 9.216331 | 123.8453 | $Na_{3.38}Zr_{1.80}Al_{0.26}Si_{2.06}P_{0.88}O_{12}$ |
| Fe-doped | 15.6505 | 9.050462 | 9.219722 | 123.7619 | $Na_{3.13}Zr_{1.94}Fe_{0.21}Si_{2.12}P_{0.85}O_{12}$ |
| Y-doped | 15.70341 | 9.0802053 | 9.222833 | 124.0603 | $Na_{3.24}Zr_{1.91}Y_{0.09}Si_{1.93}P_{1.02}O_{12}$ |
| Co-doped | 15.6755 | 9.069542 | 9.214981 | 123.9256 | $Na_{3.47}Zr_{1.93}Co_{0.18}Si_{1.97}P_{0.91}O_{12}$ |
| Ni-doped | 15.68352 | 9.073429 | 9.211291 | 123.9757 | $Na_{3.59}Zr_{1.92}Ni_{0.21}Si_{1.93}P_{0.91}O_{12}$ |
| Zn-doped | 15.68515 | 9.075624 | 9.212081 | 123.9897 | $Na_{3.43}Zr_{1.83}Zn_{0.22}Si_{1.93}P_{1.02}O_{12}$ |

**Table 4.2.1**. Room temperature lattice parameters and actual stoichiometry of all NASICON samples. Rietveld refinement was used to determine lattice parameters. Stoichiometry was determined from WDS and normalized by 12 oxygen atoms per molecular formula of NASICON.

Overall elemental analysis confirmed there was an increased amount of sodium in aliovalent substituted NASICON. Furthermore, divalent substituted NASICON contained a higher sodium content than trivalent doped NASICON as expected. The microstructure of the samples was also investigated. SEM images of all the NASICON samples are given in **Fig. 4.2.2**. In general, the particle size is in the submicron range and the grains are well connected. While most NASICON samples were defined by cubic grains with an average particle size smaller than 1 μm, Y-doped NASICON

differed in that there was greater necking between particles, smaller average particle size, and much more rounded grains. Furthermore Al-doped NASICON and Fe-doped NASICON had an inhomogeneous grain shape, displaying cubic particles, triangular particles, and irregular particles.

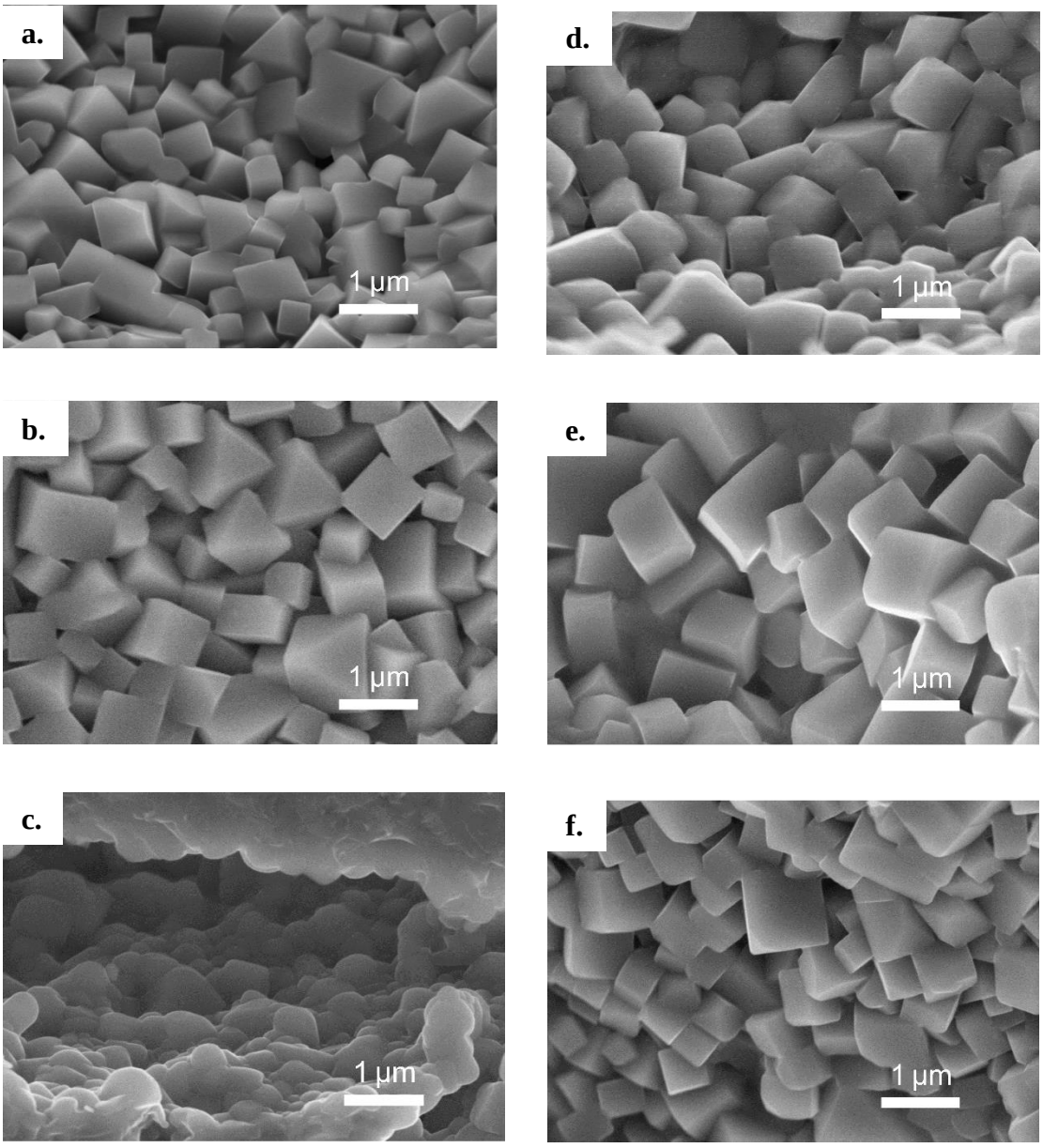


**Fig. 4.2.2**. SEM images of **a.** Al-doped NASICON **b.** Fe-doped NASICON **c.** Y-doped NASICON **d.** Co-doped NASICON **e.** Ni-doped NASICON and **f.** Zn-doped NASICON

The microstructure of Ni-NASICON, Zn-NASICON, and Co-NASICON were the most consistent, demonstrating that NASICON doped with the +2 valent cations had the most uniform cubic particles. Additionally, there was no indication from the SEM photographs or from energy dispersive spectroscopy (EDS) that there was significant glassy phase in any sample. The microstructure of the samples could probably be further improved, as optimization of the fabrication process and sintering conditions was not the focus of this investigation.

As indicated earlier, the structure and phase of NASICON is the primary concern of the investigation. Namely, understanding the effect of aliovalent doping on the rhombohedral-monoclinic phase transition. To accomplish this, *in-situ* X-ray diffraction was run from 30°C up to 300°C to monitor the NASICON structure over the phase transition. **Fig. 4.2.3** is a plot of the high temperature XRD scans for the undoped NASICON.

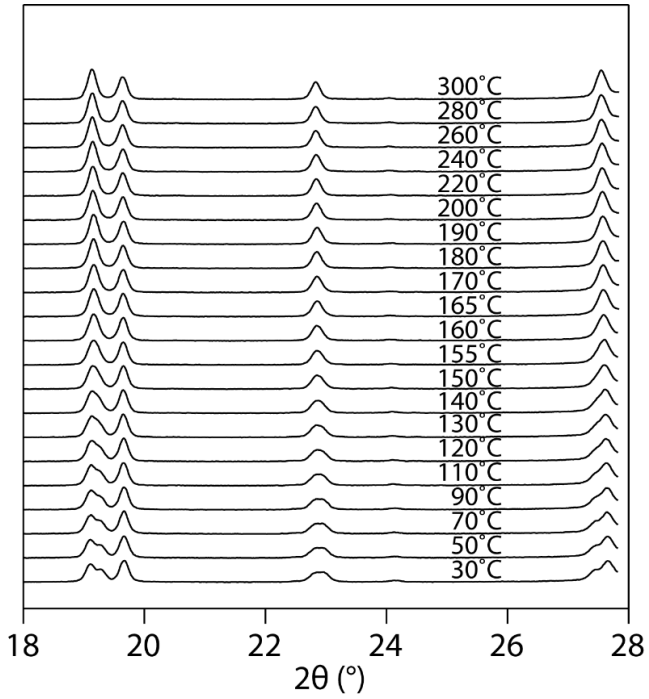


**Fig. 4.2.3**. XRD patterns of $Na_3Zr_2Si_2PO_{12}$ from 30°C up to 300°C. The high temperature XRD scan is zoomed in on the 2theta region from 18° to 28°.

The plot clearly illustrates a change from lower symmetry phase at 30°C to higher symmetry phase at 300°C, due to the increased number of peaks at lower temperature. The XRD patterns were fit at each temperature and lattice parameters were extracted. The refined lattice parameters at each temperature as well as the geometric relationships between the monoclinic and rhombohedral unit cells were used to model the phase transition.

The phase transition from rhombohedral to monoclinic was modeled by equating the lattice parameters geometrically. The low temperature (monoclinic) and high temperature (rhombohedral) phases of NASICON are geometrically related as illustrated in **Fig. 4.2.4**.

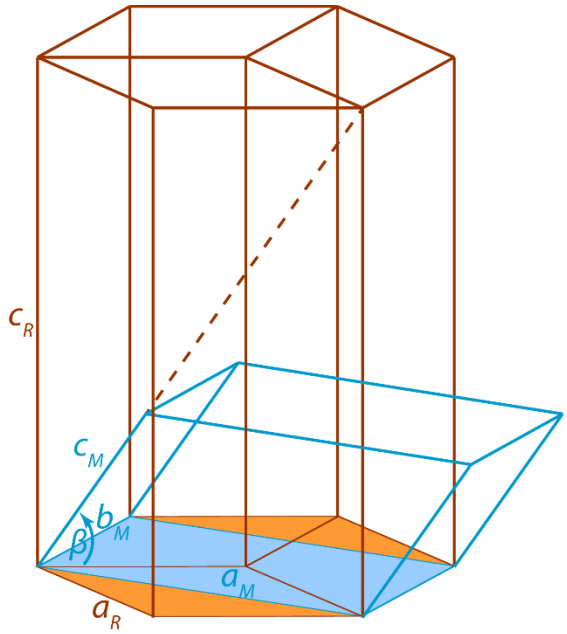


**Fig. 4.2.4**. Geometric representation of the monoclinic unit cell aligning with the rhombohedral unit cell. The orange base represents the rhombohedral phase and the blue base represents monoclinic. The hexagonal lattice system is used as a reference.

Above the phase transition the two unit cells fit together as illustrated in the figure and the following relationships are true: $a_M = a_R\sqrt{3}, b_M = a_R,\ c_M = 1/3\sqrt{3{a_R}^2 + {c_R}^2}$, with $a_M$, $b_M$, $c_M$, and $\beta_M$ representing the monoclinic lattice parameters, and $a_R$ and $c_R$ for the rhombohedral lattice parameters. As the lattice cools below the phase transition temperature, the rhombohedral lattice distorts to the monoclinic cell. The distortion of the rhombohedral cell to the less symmetric monoclinic cell can be modeled by two different mechanisms (Eq. 4.2.1 and Eq. 4.2.2).

$$1 - a_M/\left(b_M\sqrt{3}\right) \qquad \text{(Eq. 4.2.1)}$$

$$1 - (3c_M \cos(180 - \beta))/a_M \qquad \text{(Eq. 4.2.2)}$$

Eq. 4.2.1 models the distortion of the rhombohedral *a*-base and is illustrated by the graphic in **Fig. 4.2.5 a**. Eq. 4.2.2 models the shear distortion of rhombohedral unit cell and is represented in **Fig. 4.2.5 b**.

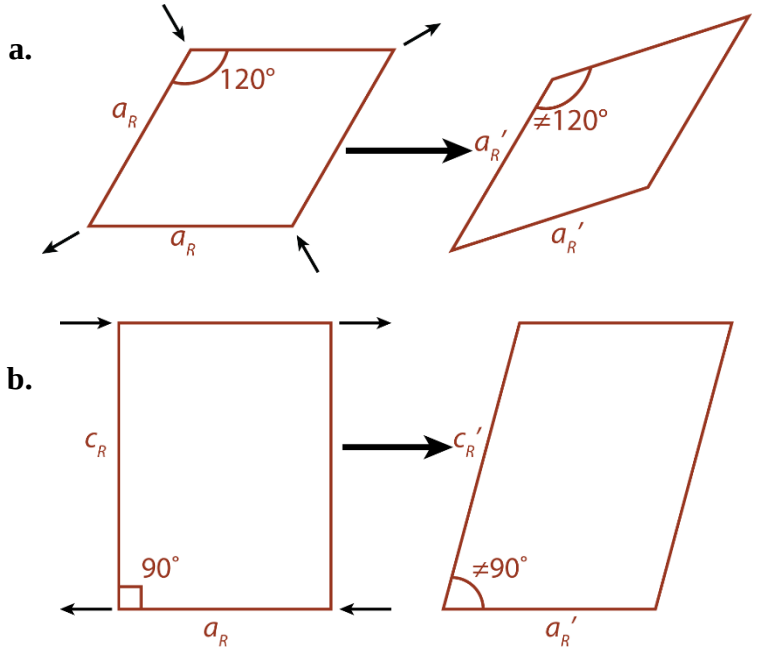


**Fig. 4.2.5 a.** Distortion of the a-base observed from the 001 direction. **b.** Shear deformation of the unit cell observed from the 010 direction. The subscript R indicates rhombohedral and R' indicates non-rhombohedral.

Above the phase transition, Eq. 4.2.1 and Eq. 4.2.2 will nominally equal zero, indicating that the unit cell is entirely rhombohedral. Below the phase transition the two equations should diverge from zero. Thus, the mechanism of the phase transition could be determined by plotting these equations against temperature. **Fig. 4.2.6 a.** and **Fig. 4.2.6 b.** are the plots of Eq. 4.2.1 and Eq. 4.2.2 versus temperature respectively for all NASICON samples.

While the data in **Fig. 4.2.6 a.** remains relatively constant over the entire temperature region, **Fig. 4.2.6 b.** can be seen to change significantly with temperature. The discontinuous change in Eq. 4.2.2 is indicative of the temperature where the phase change occurred. Furthermore, the dependence of Eq. 4.2.2 on temperature indicates that shear distortion of the rhombohedral unit cell is responsible for the phase transition. Meanwhile Eq. 4.2.1 independence on the temperature reveals that the a-base of the unit cell remains relatively constant through the phase transition. Finally, despite the robustness of the Le Bail method, there is a small systematic error that prevents Eq. 4.2.1 and Eq. 4.2.2 from ever truly reaching zero. This error is a result of the limited number of observable peaks within the 2θ range covered by the detector and the high degree of peak overlap between the high and low temperature phases. Nevertheless, the discontinuous change in the value of Eq. 4.2.2 is undeniable proof of the phase transition.

From the data it is clear the deformation of the unit cell is dependent on the dopant. Yttrium doped NASICON exhibits approximately 50% less unit cell distortion than undoped NASICON at 100°C as well as smaller overall distortion of the lattice through the phase transition.

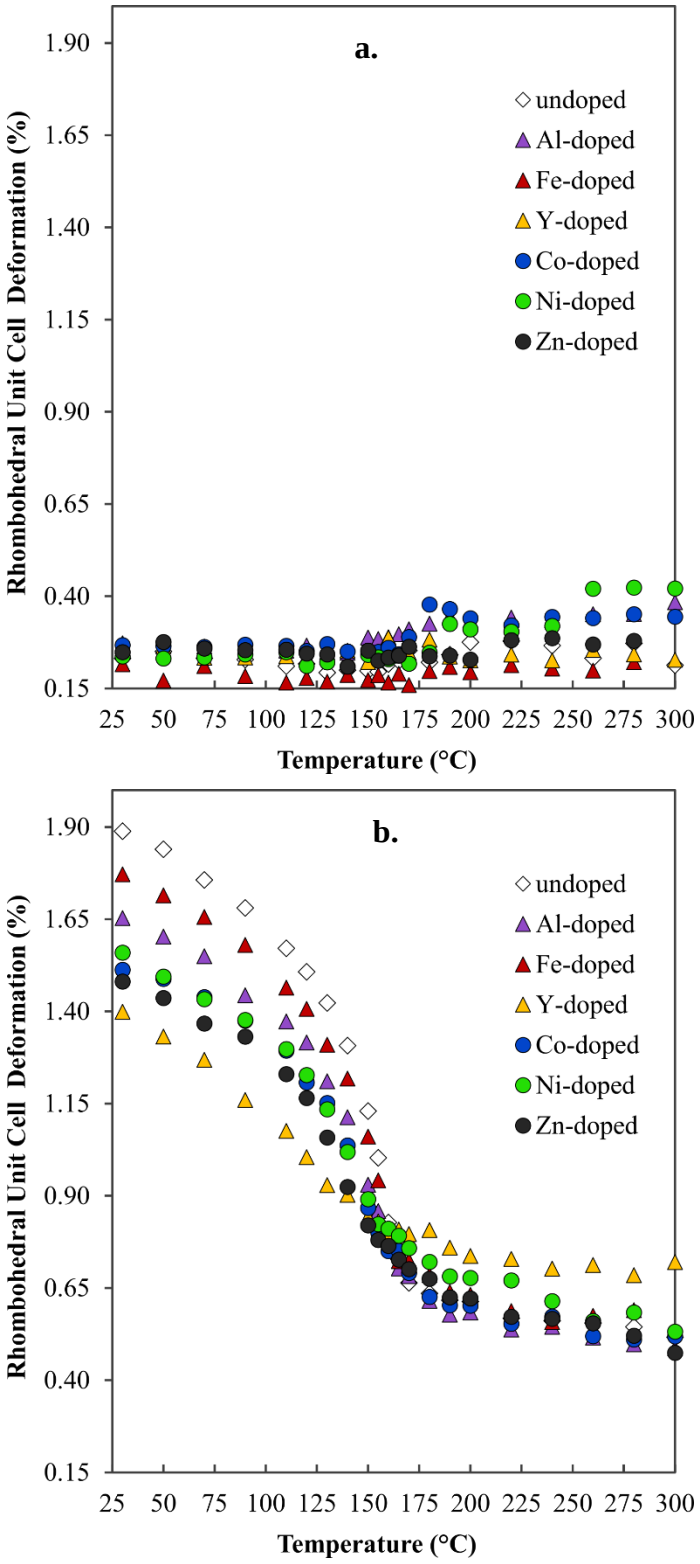


**Fig. 4.2.6 a.** Shear deformation (Eq. 4.2.1) plotted as a function of temperature for all doped and undoped NASICON. **b.** Distortion of the unit cell *a*-base (Eq. 4.2.2) plotted as a function of temperature for all doped and undoped NASICON.

In fact all aliovalent doping of the zirconium site resulted in a reduction of shear deformation of the rhombohedral unit cell below the phase transition. DSC measurements also confirmed that doping NASICON reduced the transition temperature of the phase change. The endothermic peak was determined by the Perkin-Elmer software and represents the critical temperature (Tc) in the phase transition. The phase transition temperature determined from DSC is presented for all samples in **Table 4.2.2**. DSC confirms that the phase transition temperature of all doped NASICON in this investigation was lower than that of base NASICON.

| Sample | Tc (°C) |
|---|---|
| Undoped NASICON | 157.7 |
| Al-doped NASICON | 151.3 |
| Fe-doped NASICON | 156.5 |
| Y-doped NASICON | 139.5 |
| Co-doped NASICON | 148.0 |
| Ni-doped NASICON | 151.2 |
| Zn-doped NASICON | 151.2 |

**Table 4.2.2**. Phase transition temperature of all NASICON samples determined from the endothermic peak (Tc) using DSC.

The reduction of the monoclinic-rhombohedral phase transition in the NASICON samples is a result of doping the zirconium site with lower valent cations. However, vacant sodium sites are filled to compensate for the charge imbalance of +3 and +2 valent dopants in the +4 zirconium site, and this could also have a stabilizing

effect that lowers the phase transition temperature. The reduction in the phase transition temperature as a result of aliovalent substitution for zirconium is analogous to the phenomena observed in aliovalent phosphorus substitution in NASICON[72]. Colomban observed that there was lower static disorder in $Na_{1+x}Zr_2Si_xP_{3-x}O_{12}$ for $1.8<x<2.2$, which ultimately caused greater monoclinic unit cell distortion and an increase in the monoclinic-rhombohedral phase transition temperature[79]. Thus, stabilization of the rhombohedral structure in doped NASICON could be a consequence of greater disorder in the crystal induced by higher levels of $Na^+$ in the lattice, or by dopant radius mismatch on the zirconium site.

There are however more variables introduced through aliovalent doping of the zirconium site. Based on the WDS analysis, sodium content was not the only variable affected by the substitution for zirconium. Silicon and phosphorus levels also varied between samples. Furthermore, the oxygen was assumed to be stoichiometric, but the material could also potentially be oxygen rich or deficient. With eighty atoms and five different elements in a single unit cell of undoped NASICON, the mechanism to establish charge balance in aliovalent doped NASICON is probably more complex than just $Na^+$ filling vacant sodium sites. In fact, the lattice volume does not linearly depend on the dopant ionic radius suggesting there are other interactions involving doped NASICON than just lattice shrinkage or expansion from site mismatch.

Nevertheless, all doped samples had higher sodium content, and exhibited less shear distortion of the unit cell at room temperature and a lower phase change temperature than undoped NASICON. What is more, a similar trend cannot be drawn between any of the other elements with respect to lattice distortion or lower phase

change temperature. However, although Y-doped NASICON did not contain the most sodium, it does have the smallest room temperature lattice distortion, the lowest phase change temperature, and it's the only sample whose main room temperature XRD peak at ~19° (2θ) does not show peak splitting indicative of monoclinic phase. Thus, yttrium helps to stabilize the rhombohedral phase of NASICON most at room temperature. This could indicate that the rhombohedral phase in doped NASICON is also influenced by the stabilization of the zirconia precursor phase. $Y_2O_3$ is known to stabilize the cubic fluorite structure of $ZrO_2$, which could cause less distortion of the NASICON unit cell upon phase formation hence stabilizing the non-distorted rhombohedral unit cell.

Overall high temperature *in-situ* X-ray diffraction data demonstrated that shear deformation of the unit cell is the mechanism that drives the transformation of the high temperature rhombohedral phase to the low temperature monoclinic phase in NASICON. Doping the zirconium site in the $Na_3Zr_2Si_2PO_{12}$ framework decreased the phase transition temperature and resulted in lower distortion of the rhombohedral lattice as it deformed to the monoclinic phase. Ultimately aliovalent substitution for the zirconium site in $Na_3Zr_2Si_2PO_{12}$ stabilized the rhombohedral phase, and yttrium doped NASICON exhibited both the smallest distortion of the rhombohedral unit cell as it transitioned to the monoclinic phase and the greatest reduction of the phase change temperature. Since the more conductive and higher symmetry rhombohedral phase only occurs at high temperatures in $Na_3Zr_2Si_2PO_{12}$, stabilizing the rhombohedral phase down to room temperature by substitution for zirconium is an avenue that should continue to be explored to improve the room temperature conductivity of NASICON. A thorough investigation of the phase transition energetics could help garner a deeper

understanding and future elimination of the rhombohedral-monoclinic phase change in NASICON.

*4.3 The effect aliovalent cation substitution on NASICON conductivity*

After the structural effects of doping the NASICON lattice was investigated, the influence of aliovalent cation substitution on conductivity was examined. The main focus was analyzing how the bulk conductivity of each sample responded to cation substitution. The 10% doped NASICON samples from the previous investigation, $Na_{3.2}Zr_{1.8}M_{0.2}Si_2PO_{12}$ ($M=Al^{3+}$, $Fe^{3+}$, $Y^{3+}$), and $Na_{3.4}Zr_{1.8}M_{0.2}Si_2PO_{12}$ ($M=Co^{2+}$, $Ni^{2+}$, $Zn^{2+}$), were studied here. For this study the bulk conductivity of the samples was the primary interest. Bulk conductivity divulges the inherent electrochemical properties of the material and is independent from processing flaws such as insulating secondary phases at grain boundaries, porosity, etc. While the microstructure can influence the total conductivity of the pellets, it should have minimal effect on the bulk conductivity of the material. Thus, the total conductivity reflects the processing of the samples, while bulk conductivity is a function of the inherent material property.

First it was important to ensure that the sample had sufficient density to provide good EIS measurements. The density was maximized for each NASICON sample by optimizing sintering temperature. Density of the samples were confirmed with a standard Archimedes test in ethanol, and are indicated in **Table 4.3.1** along with sintering temperature. The NASICON lattice parameters were used to construct the theoretical cell volume for density measurements, and impurities were ignored because of their small presence in the samples.

| Sample | Sintering temperature (°C) | Density (% of theoretical) |
|---|---|---|
| Undoped NASICON | 1200 | 96.1 |
| Al-doped NASICON | 1150 | 93.1 |
| Fe-doped NASICON | 1125 | 94.5 |
| Y-doped NASICON | 1200 | 99.2 |
| Co-doped NASICON | 1125 | 97.9 |
| Ni-doped NASICON | 1150 | 97.1 |
| Zn-doped NASICON | 1150 | 96.9 |

**Table 4.3.1**. Sintering temperature and resulting density of all NASICON samples.

To study the effect of aliovalent doping on the sodium ion diffusion in NASICON, it was important to employ EIS to study the bulk conductivity of the electrolyte and gain deeper insight into the electrical properties. Like others authors, sodium ion blocking platinum electrodes were placed on the NASICON to measure the impedance of the electrolyte[12,80]. The Nyquist plots in **Fig. 4.3.1 a.** and **Fig. 4.3.1 b.** illustrate the room temperature impedance of each sample. The Nyquist plots contain both an unresolved and clearly defined semi-circle for all investigated compounds. The unrealized high frequency semi-circle is attributed to ion transport in the grains, while the low frequency semi-circle is caused by ion transport in the grain boundaries. This macroscopic process of mass and charge transport can be described by an equivalent circuit (**Fig. 4.3.1 b.** insert). A resistor describing the bulk resistance in series with a resistor and CPE element in parallel describing the grain boundary contribution.

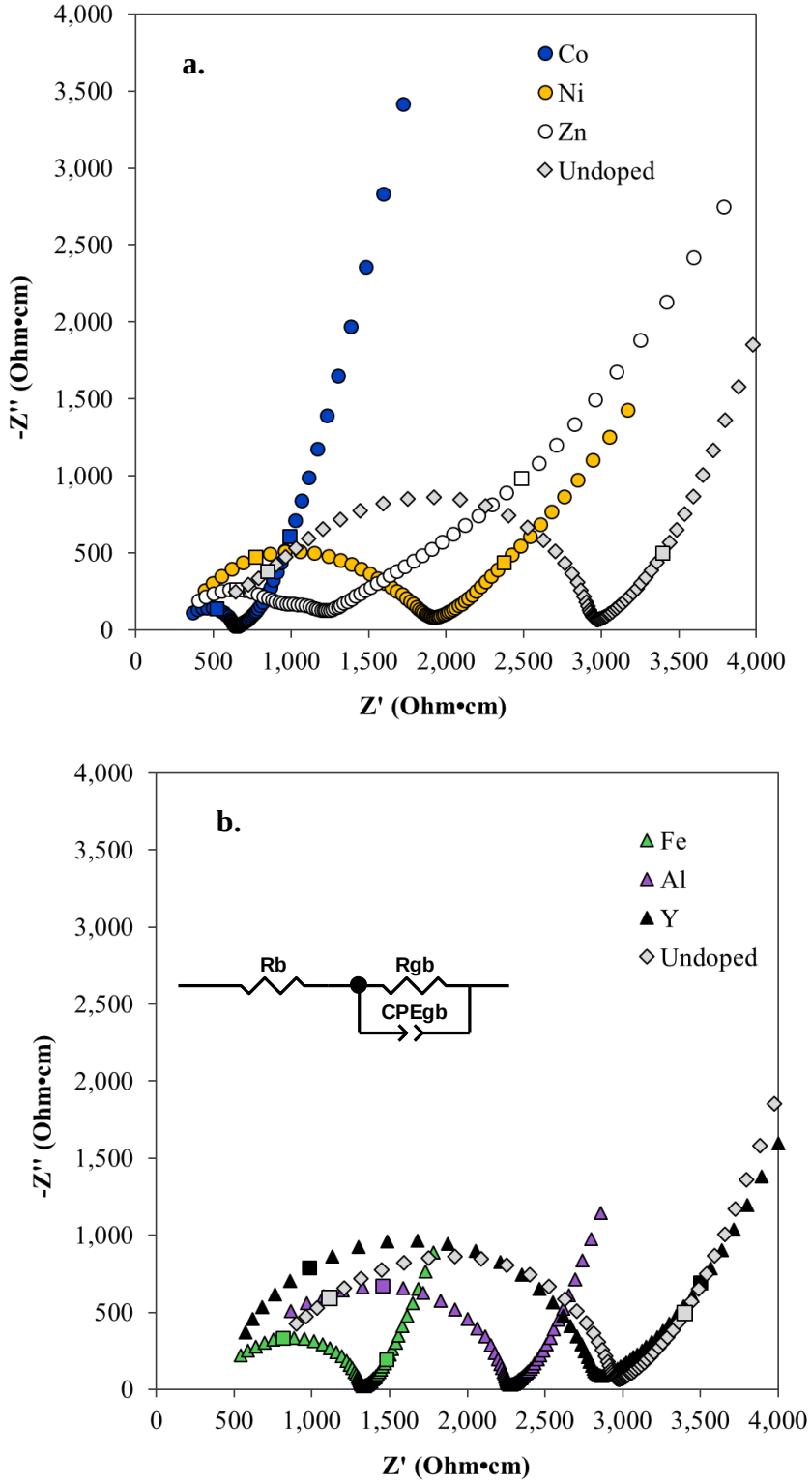


**Fig. 4.3.1 a**. EIS plot of undoped and divalent substituted NASICON at 25°C. **b**. EIS plot of undoped and trivalent substituted NASICON at 25°C. The first square data point indicates a frequency of $10^6$ Hz while the second square data point indicates 10 Hz.

The equivalent circuit model consists of a resistor connected in series with an RQ element, corresponding to the contributions from the grain bulk and grain boundary respectively. A CPE element is used to describe the non-ideal capacitance of the dispersed semi-circle element. Although the bulk resistance arc could not be directly resolved, Scribner Z-view software was used to fit the grain boundary resistance arc. The bulk resistance was then identified as the origin of the grain boundary arc at the x-axis, while the total resistance is the end of grain boundary arc.

There is also an artifact from the EIS setup that is not included in the equivalent circuit model. The resistance of the wires and blocking electrodes contribute an additional 0.25 Ω at room temperature (as measured by a null) that was subtracted from the fit bulk and grain boundary resistances. A null was measured at each temperature through the entire temperature range and subtracted from corresponding EIS measurement. Ultimately the low frequency data outside the grain boundary arc was not fit with Z-view, since this region does not correspond to ion mobility in the electrolyte, but rather semi-infinite diffusion to the blocking electrodes consistent with a Warburg element[81]. There is also a depressed region after the grain boundary in the Zn-doped sample that was not fit with the RQ circuit, but was still included in the total conductivity calculation. The raw fitting data collected from Z-view is listed in **Table 4.3.2**. The conductivity was normalized by a circular pellet geometry of a roughly 8.5 cm diameter and a 1-2 cm thickness for each sample. The calculated capacitance of the fitted grain boundary arcs all matched typical capacitance values attributed to ion transport in the grain boundaries of ceramics[2].

| Sample | Rb Ω (error %) | Rgb Ω (error %) | CPE-T x$10^{-9}$ F (error %) | CPE-P (error %) |
|---|---|---|---|---|
| Undoped NASICON | 175.5 (1.36) | 576.1 (0.76) | 15.0 (7.94) | 0.81 (0.72) |
| Al-doped NASICON | 194.4 (0.96) | 591.8 (0.43) | 2.66 (4.11) | 0.85 (0.35) |
| Fe-doped NASICON | 111.9 (0.53) | 239.8 (0.32) | 14.0 (2.9) | 0.82 (0.27) |
| Y-doped NASICON | 93.35 (0.4) | 559.2 (0.12) | 5.9 (1.38) | 0.85 (0.12) |
| Co-doped NASICON | 73.81 (1.26) | 80.03 (1.53) | 4.27 (15.29) | 0.93 (1.16) |
| Ni-doped NASICON | 68.6 (3.52) | 349.9 (1.44) | 27.1 (13.93) | 0.77 (1.27) |
| Zn-doped NASICON | 67.89 (4.20) | 155.6 (3.86) | 7.91 (39.28) | 0.87 (3.05) |

**Table 4.3.2**. Fitting parameters and percent error generated by the equivalent circuit fit of the EIS data in Z-view for all NASICON samples.

The shape of the EIS curve for each sample also began to diverge from the room temperature plot with increasing temperature. **Fig. 4.3.2** illustrates the impedance of the Al-doped NASICON sample over the entire measured temperature range. Up to a temperature of 100°C the grain boundary arc is clearly observed, however with increasing temperatures the arc disappears progressively from the spectra, indicating a thermally activated process with the addition of an inductive contributor. The inductive tail observed in the impedance at high temperature was also observed in the null measurement. In both cases the inductive tail curved toward the origin which is indicative of natural inductance in the setup. The high temperature inductance was

manually eliminated, and the intersection of the real impedance with the negative imaginary portion of the Nyquist plot was identified as the bulk resistance.

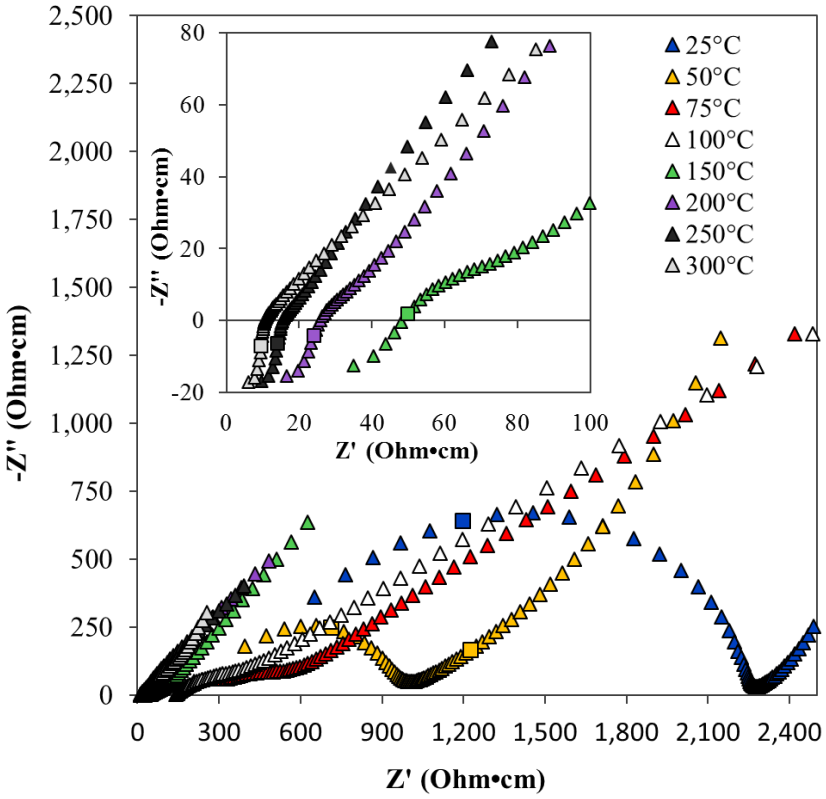


**Fig. 4.3.2**. EIS plot of Al-doped NASICON at selected temperatures indicated on the right. The first square data point indicates a frequency of $10^6$ Hz while the second square data point indicates 10 Hz.

Unfortunately, bulk resistance could not be separated from total resistance for all temperatures. The grain boundary arc dissolved into the Warburg tail above approximately 200°C, and thus the intersection with the x-axis is taken as the total resistance. Since the grain boundary resistance is negligible at higher temperatures, the total resistance is effectively the grain resistance at high temperatures.

The frequency dependence of the real and imaginary parts of impedance at 25°C for all NASICON samples is shown in **Fig. 4.3.3 a.** and **Fig. 4.3.3 b.** respectively.

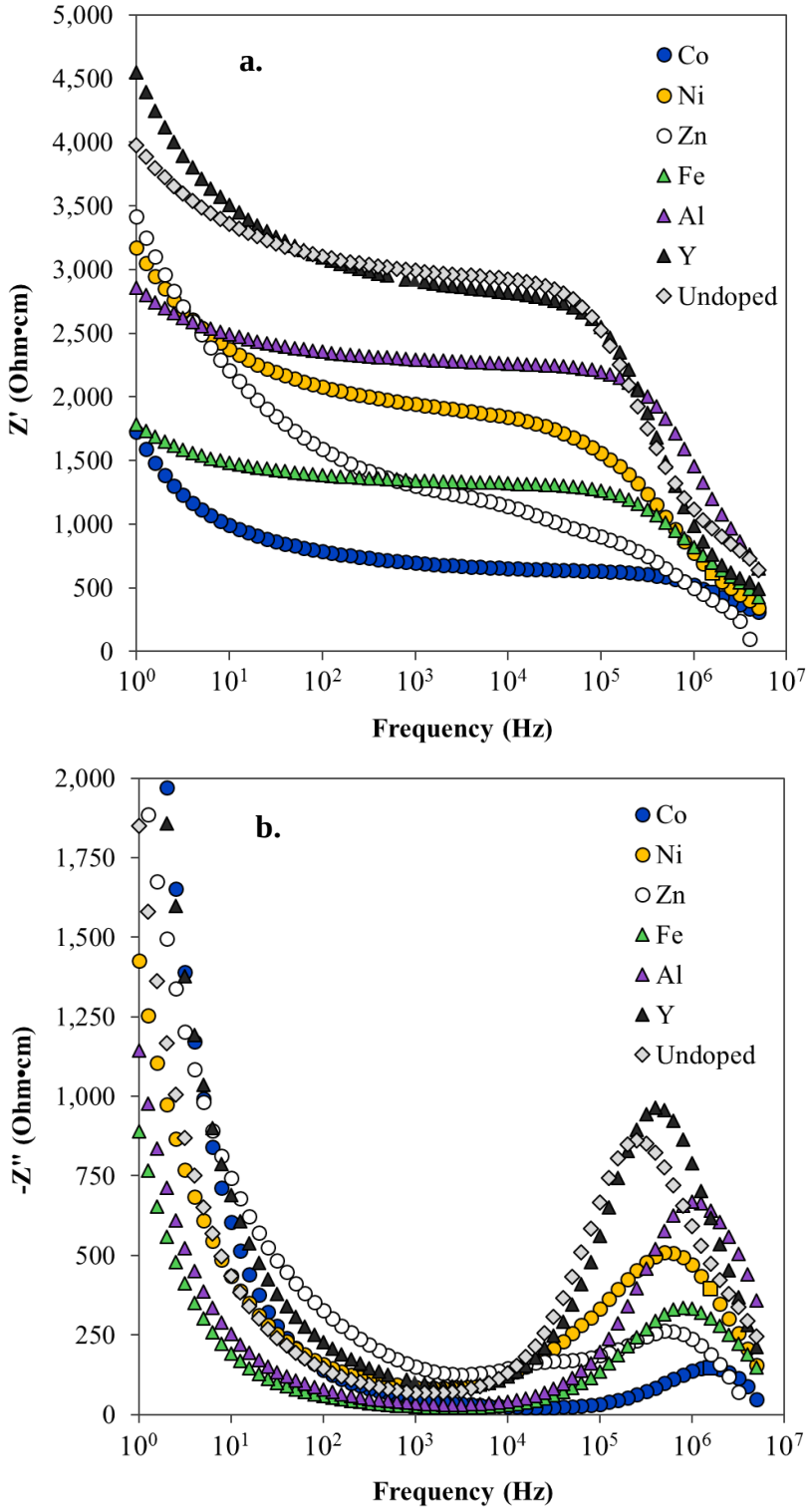


**Fig. 4.3.3 a.** Real part of the complex impedance for all doped NASICON at 25°C. **b.** Imaginary part of the complex impedance for all doped NASICON at 25°C.

A step-like decreasing trend is observed for all the dopants in the real impedance spectra, while a peak shape spectra was obtained from the imaginary part. The plot reveals that the Z" peak occurs in the frequency range from $2x10^5$ to $10^6$ Hz, depending on the sample. This peak corresponds to the middle of the step-like decreasing trend of the real portion, indicating a relaxation behavior of the ions. Finally, the real portion of the impedance was plotted as a function of temperature for a representative sample (Al-doped NASICON) in **Fig. 4.3.4**.

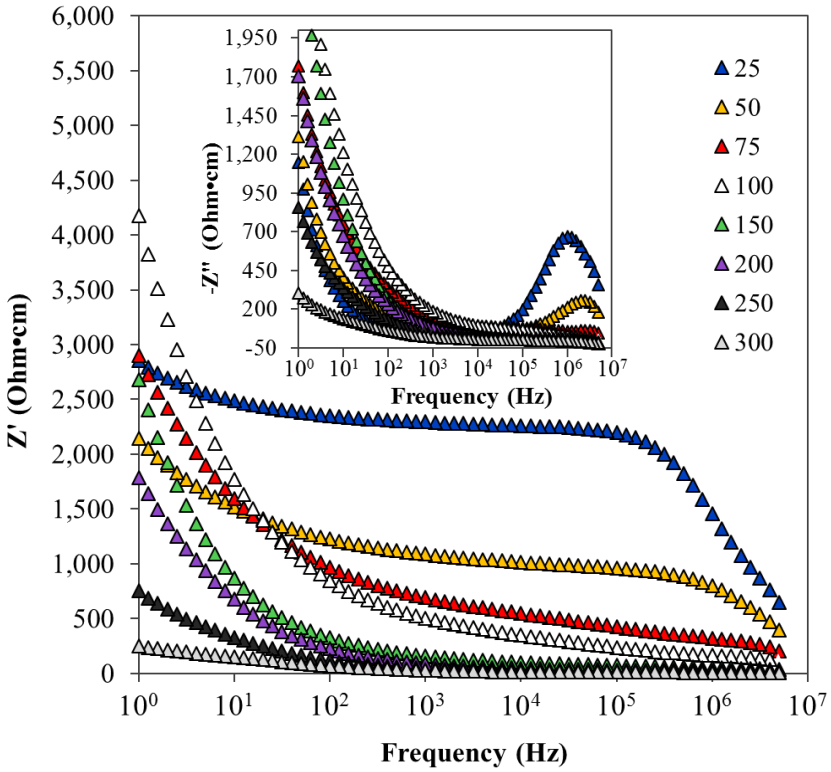


**Fig. 4.3.4** Real and imaginary parts of the complex impedance for Al-doped NASICON at selected temperatures.

The spectra were characterized by two dispersion regions, where the boundary between the two regions shifts towards higher frequencies as the temperature increases. This behavior is another indication for a thermally activated process, and is typical in

relaxation type dispersions. The relaxation frequencies, $f_R$, obtained from the Z" vs. frequency graph (insert **Fig. 4.3.4**) also exhibit a shift toward high frequency with increasing temperature.

Once the impedance of all the samples were analyzed, the electrical properties could be extracted. The bulk conductivity, total conductivity, and activation energy of all the NASICON samples is listed in **Table 4.3.3**.

| Sample | Bulk Conductivity at 25°C (S/cm) | Total Conductivity at 25°C (S/cm) | Activation energy (eV) |
|---|---|---|---|
| Undoped NASICON | $1.34\times10^{-3}$ | $3.35\times10^{-4}$ | 0.267 |
| Al-doped NASICON | $1.77\times10^{-3}$ | $4.39\times10^{-4}$ | 0.258 |
| Fe-doped NASICON | $2.44\times10^{-3}$ | $7.53\times10^{-4}$ | 0.264 |
| Y-doped NASICON | $2.39\times10^{-3}$ | $3.52\times10^{-4}$ | 0.224 |
| Co-doped NASICON | $3.33\times10^{-3}$ | $1.55\times10^{-3}$ | 0.379 (300°C-225°C)<br>0.266 (200°C-25°C) |
| Ni-doped NASICON | $3.47\times10^{-3}$ | $6.18\times10^{-4}$ | 0.362 (300°C-200°C)<br>0.192 (175°C-25°C) |
| Zn-doped NASICON | $3.75\times10^{-3}$ | $8.05\times10^{-4}$ | 0.321 (300°C-225°C)<br>0.221 (200°C-25°C) |

**Table 4.3.3** Bulk conductivity and total conductivity given for all samples at room temperature. Activation energy is listed for high and low temperature for non-linear Arrhenius plots. The activation energy is calculated over the whole 300°C-25°C temperature range if a specific range is not indicated.

Cobalt-doped NASICON exhibited the highest room temperature total conductivity of all samples, $1.55\times10^{-3}$ S/cm. Zn-doped NASICON meanwhile had the highest bulk conductivity of all samples. While the microstructure of the sintered

pellets was not optimized, the enhanced total conductivity of the Co-doped NASICON was most likely a result of the dense and uniform grains. Furthermore, since the conductivity of the doped NASICON was superior to the undoped samples it was necessary to ensure the measured conductivity was purely ionic. A DC polarization technique was run on the samples to effectively measure the ionic transference number. A select DC polarization plot (Co-doped NASICON) is presented in **Fig. 4.3.5**.

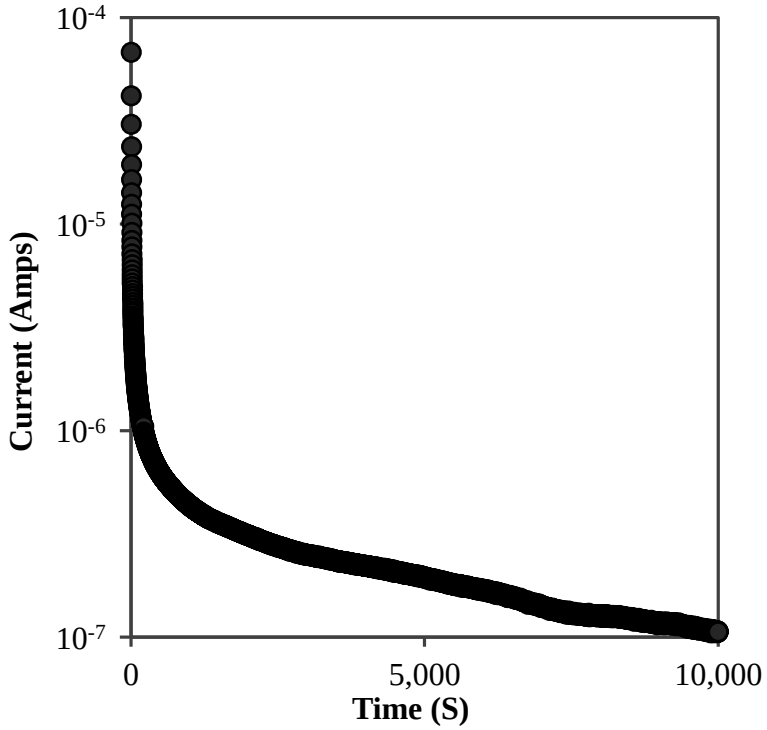


**Fig. 4.3.5** DC polarization of Co-doped NASICON at 25°C represented as current vs. time.

A transference number greater than 0.999 was calculated for all doped and undoped NASICON samples at room temperature. This confirms that the conductivity is almost purely ionic with very little conduction of electrons. Since it was verified that the conducting species in NASICON was sodium ions, the ionic mobility of different samples could be compared. Ultimately comparing the sodium ion mobility between

samples was achieved by analyzing the bulk conductivity of the NASICON samples over a wide temperature range.

The Arrhenius plots of bulk conductivity for doped and undoped NASICON is plotted in **Fig. 4.3.6**

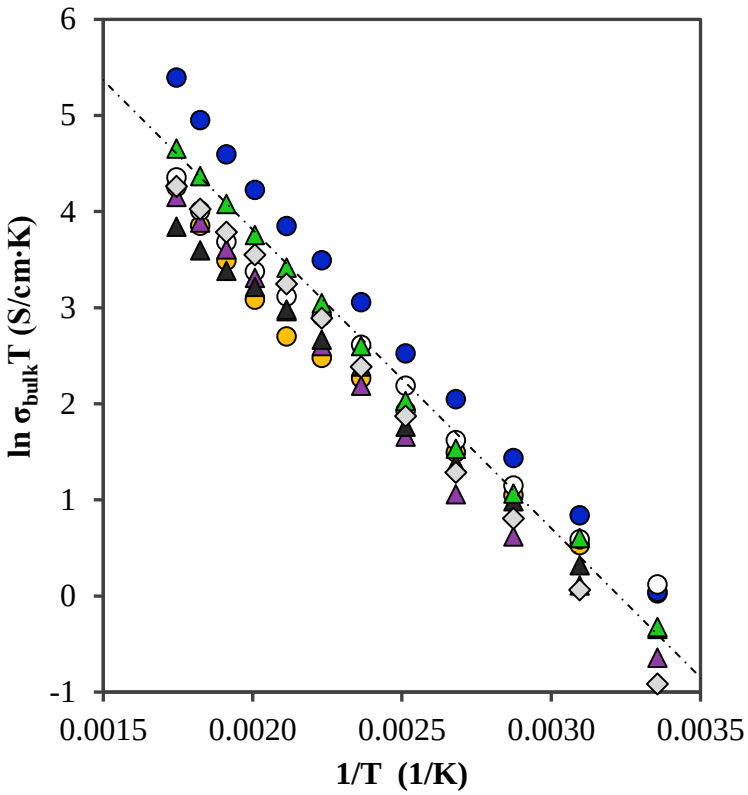


**Fig. 4.3.6**. Arrhenius plot of all NASICON samples. The following legend indicates the dopant: ●Ni ●Co ○Zn ▲Al ▲Y ▲Fe ◇Undoped

The impedance results demonstrate that all aliovalent doping investigated improved the bulk conductivity of NASICON at room temperature. Overall the divalent cation substituted NASICON exhibited higher bulk conductivity when compared to trivalent doped NASICON. At 300°C Co-doped NASICON exhibited the largest bulk conductivity improvement over undoped NASICON with almost a threefold increase. Meanwhile at 25°C, Zn-doped NASICON exhibited bulk conductivity that was over

three times greater than undoped NASICON. The enhancement of the +2 dopants on ionic conductivity at both high and low temperatures can be attributed to the change in activation energy. Co, Ni, and Zn-doped NASICON have a distinct high temperature and low temperature activation energy as well as higher room temperature conductivity than the other NASICON samples. In contrast undoped NASICON and Al, Fe, and Y-doped NASICON have a linear activation energy over the whole temperature range. The change in activation energy could be a result of the phase change that occurs in these materials above approximately 150°C. The conductivity pathways in the high temperature rhombohedral phase may be more severely affected by aliovalent substitution than in the low temperature monoclinic phase. Therefore, the activation energy would change in a more pronounced way in NASICON doped with divalent cations.

Aliovalent substitution increases $Na^+$ conductivity in NASICON as result of structural changes and an optimization of the chemistry. By doping the +4 zirconium site with lower valent cations, the sodium in the lattice must be increased to compensate for the charge imbalance. The $Na_3Zr_2Si_2PO_{12}$ structure has a single vacant $Na^+$ site per molecular formula, thus the additional sodium added to the doped NASICON would be expected to fill the vacant sites. While charge balance in doped NASICON may be obtained by increasing the sodium occupancy, the defects associated with aliovalent zirconium substitution is also likely to be more complex than solely adjustments in sodium levels. For example, oxygen vacancies or cation interstitials could be forming to provide charge balance. Although oxygen was set to a stoichiometric 12 in the WDS analysis and therefore appears constant, both the P and Si levels vary slightly between

samples. Furthermore, the lattice volume does not linearly depend on the apparent dopant radius supporting that there may be other interactions within the 80-atom large $Na_3Zr_2Si_2PO_{12}$ unit cell. Nevertheless, the aliovalent substituted NASICON has increased sodium in a sodium deficient material with little secondary phase, emphasizing that more Na must be in the lattice.

Increased sodium in the lattice equates to an increase in charge carrier density. Thus, an influx of mobile sodium ions in the conducting pathways would result in higher conductivity. The WDS analysis confirmed that NASICON doped with +2 oxidation state cations contained the most sodium in the bulk, and helps explain why Co, Ni, and Zn-doped NASICON exhibited higher conductivity than all the other samples. Furthermore, aliovalent doping decreases the electrostatic interactions of the sodium ion with the zirconium site. A lower valent cation occupying the zirconium site would decrease the coulombic repulsion between the dopant ion and the sodium ion. With less electrostatic interactions on the sodium ion, it would take less energy for the ion to navigate the bottlenecks around the zirconium ions.

Although increased sodium in the lattice enhanced the conductivity, there was still variability in the bulk conductivity amongst the +3 and +2 valent doped NASICON. Thus, the ionic radius of the dopant, another critical variable affecting the structure, had a large impact on the conductivity of NASICON. Graphing the ionic radius of dopant vs. bulk conductivity revealed that the optimum value of dopant radii is approximately 0.73 Å. In **Fig. 4.3.7** the relationship between bulk conductivity of the doped NASICON and dopant ionic radius can be seen at a range of temperatures. Therefore, while the ionic radius of zirconium (0.72 Å) is an ideal size for the site,

undoped $Na_3Zr_2Si_2PO_{12}$ does not have the advantage of increased sodium and charge imbalance at the Zr site that aliovalent substitution offers.

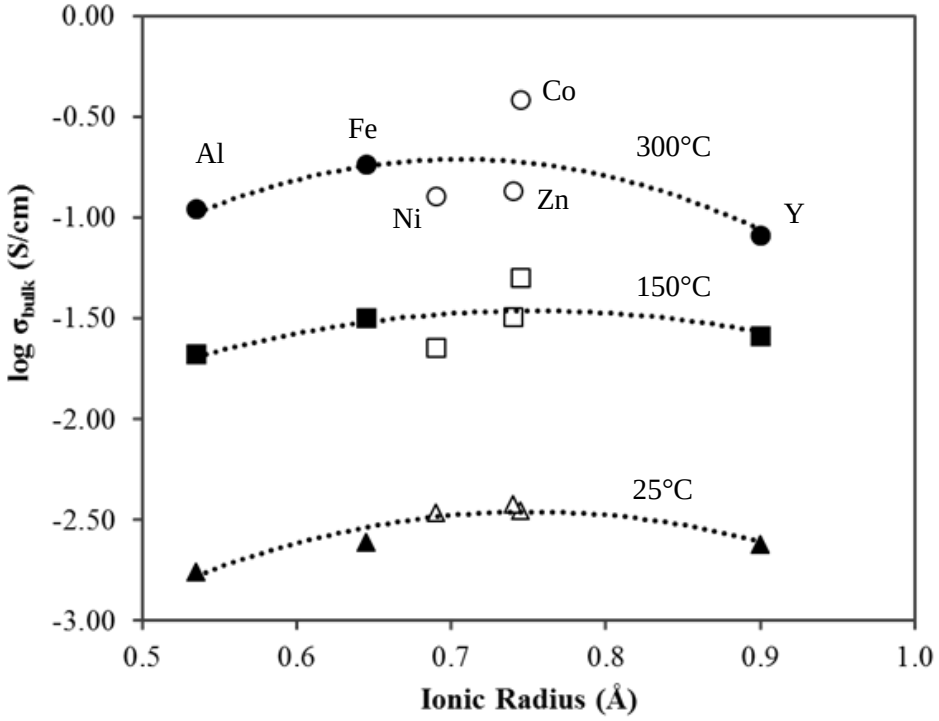


**Fig. 4.3.7**. Bulk conductivity of doped NASICON vs. the ionic radius of the dopant. Circles represent conductivity at 300°C, squares represent conductivity at 150°C, and triangles represent conductivity at 25°C. Black shaded shapes represent trivalent dopants and white shapes are divalent dopants. A polynomial fit was used to describe the best fit line.

It is clear that increasing the amount of sodium in the NASICON structure through aliovalent doping the zirconium site enhances the bulk conductivity. Increased sodium charge carriers in the lattice and a charge imbalance of the zirconium site related directly to improved ionic mobility. As a result, the low temperature activation energy was decreased for doped samples while their room temperature conductivity was increased. The conductivity was impacted by the ionic radius of the dopant as well, illustrating another important factor that effects the mobility of sodium ions.

Ultimately aliovalent substation of NASICON maximizes the conductivity when the dopant is +2 oxidation state cations and has an ionic radius of ~0.73 Å. As a result, Zn-doped NASICON displayed the highest bulk conductivity at room temperature with $3.75\times10^{-3}$ S/cm. Nonetheless, Co-doped NASICON exhibited the highest total conductivity at room temperature, $1.55\times10^{-3}$ S/cm, which is suitable for practical application even before it has been optimized.

*4.4 Optimizing the Bulk Conductivity of NASICON with Aliovalent Doping*

With the both the conductivity and structural trends associated with doping the NASICON mapped out, it was important to optimize the cation substitution to maximize conductivity. To begin with, as it was determined that divalent cation substitution provided improved conductivity over trivalent cation substitution, the Zn, Co, and Ni dopants were explored further. As a cation substitution rate of 10% was already investigated in depth for NASICON, this study would focus on varying the dopant concentration. The composition of the NASICON samples had the following general formula: $Na_{3+2x}Zr_{2-x}M_xSi_2PO_{12}$ (for x=0.1 0.2, 0.3, 0.4, 0.5 and M=$Co^{2+}$, $Ni^{2+}$, $Zn^{2+}$). The samples were again synthesized following a standard solid state synthesis route, and a range of sintering temperatures were selected to obtain robust samples. The sintering temperature for each sample is detailed in **Table 4.4.1**. From the sintering temperatures it is clear that as the amount of zirconium decreased and the divalent dopant increased, the resulting sintering temperature dropped. Decreasing the sintering temperature is an important facet of increasing the dopant concentration since it would make manufacturing of the material cheaper and easier.

| NASICON dopant | 5% doped | 10% doped | 15% doped | 20% doped | 25% doped |
|---|---|---|---|---|---|
| Zn | 1175°C | 1150°C | 1125°C | 1100°C | 1075°C |
| Co | 1150°C | 1125°C | 1100°C | 1075°C | 1050°C |
| Ni | 1175°C | 1150°C | 1125°C | 1100°C | 1075°C |

**Table 4.4.1**. Sintering temperature for a range of NASICON samples. The left column displays the dopant and the top row identifies the total dopant concentration. The sintering time is twelve hours at each condition.

X-ray diffraction was performed on all the materials to check the phase. As the Zn cation substation increased, the amount of secondary phase also increased. The XRD patterns of the Zn-doped NASICON is plotted in **Fig. 4.4.1**.

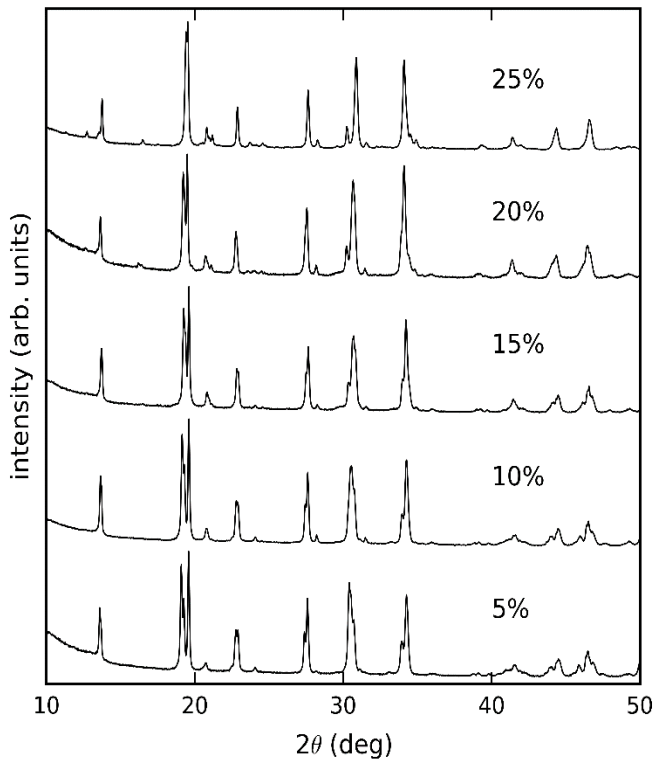


**Fig. 4.4.1**. Room temperature X-ray diffraction patterns for Zn-doped NASICON. The amount of zinc substitution is given as percent above the pattern.

The 5-15% Zn-doped NASICON samples showed both $Na_3PO_4$ and $ZrO_2$ secondary phases, as was detected in the previous study. The samples with greater amounts of zinc substitution, 20-25% Zn-doped NASICON, exhibited the secondary phase $Zn_3(PO_4)_2$. The existence of the zinc containing secondary phase revealed that the NASICON could not incorporate more than approximately 20% Zn substitution. The dopant containing secondary phase was also present in Co and Ni-doped NASICON for dopant concentration of 20% or higher.

After synthesizing and characterizing all the samples, the conductivity of the samples was measured. The room temperature conductivity of Zn, Co, and Ni-doped NASICON vs. the dopant concentration is presented in **Fig. 4.4.2**.

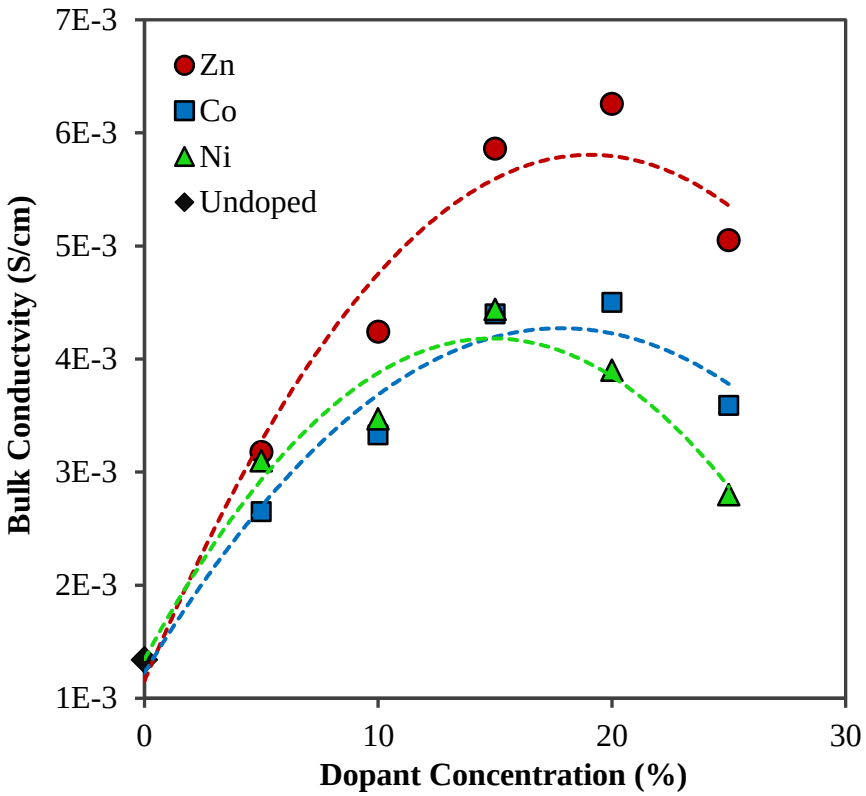


**Fig. 4.4.2**. Room temperature bulk conductivity as a function of dopant concentration for Zn, Co, and Ni-doped NASICON.

As detailed in the figure, the maximum conductivity of doped NASICON occurred at a dopant concentration between 15-20%. This peak in conductivity makes sense from a phase stability point of view. As the aliovalent dopant concentration increased, the conductivity also increased due to the presence of the divalent cation. Work done in the previous study demonstrated that the substitution of divalent cations into the NASICON network had the biggest effect on conductivity. Decreased Coulombic repulsion forces from the lower valance state would allow for faster sodium ion transport. As the dopant concentration increased past the phase stability of the NASICON, the conductivity decreased. The dopant containing secondary phase in NASICON grew when the dopant concentration increased above 20%. The increase in the dopant containing secondary phase formation was due to the NASICON structure being unable to incorporate any more mismatched cations into the lattice. Therefore, beyond the threshold of incorporation, the NASICON conductivity suffered with the increase of secondary phase. Ultimately the peak in conductivity corresponded to the highest possible cation incorporation in the NASICON lattice.

From the room temperature conductivity, the Zn-doped NASICON exhibited higher conductivity than the Co and Ni-doped samples. Examining the conductivity as a function of temperature for Zn-doped NASICON revealed that the lower energy barrier for sodium ion conduction played a significant role in the increased conductivity at higher dopant concentrations. The Arrhenius behavior of undoped NASICON as well as 10% Zn-doped and 20% Zn-doped NASICON is given in **Fig. 4.4.3**.

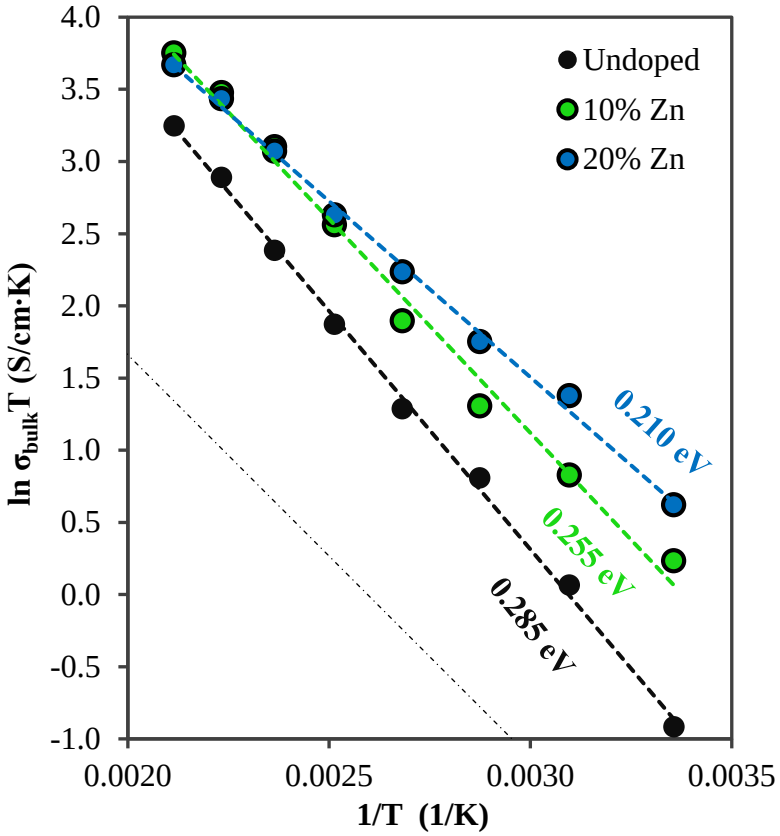


**Fig. 4.4.3**. Arrhenius plot of bulk conductivity for 10% Zn-doped, 20% Zn-doped, and undoped NASICON. The fit linear fit of the data and resulting activation energy is given for each sample.

As discussed in the previous section, there is a definite improvement in the conductivity of NASICON when the lattice is doped with divalent cations. As expected, the increase of conductivity is seen for both the 10% Zn-doped NASICON and the 20% Zn-doped NASICON. The main difference between the 10% and 20% Zn-doped NASICON though is the activation energy. The 20% Zn-doped NASICON has higher room temperature conductivity because of the lower activation energy. For the ten percent doped NASICON samples studied previously, the decrease in activation energy was attributed to lower distortion of the rhombohedral lattice to the monoclinic lattice. Therefore, high temperature XRD was performed on the Zn-doped samples to

determine if the phase change from rhombohedral to monoclinic played a role in the reduction of activation energy. Again, the phase and lattice parameters were mapped out as a function of temperature to evaluate the lattice distortion over the phase transition. The lattice parameters were then plugged into Eq. 4.2.1 and Eq. 4.2.2 as detailed in the previous section. As was observed before, Eq. 4.2.2 exhibited a temperature dependence while Eq. 4.2.1 was fairly stationary. The shear deformation of the rhombohedral unit cell as a function of temperature is plotted for the Zn-doped NASICON samples in **Fig. 4.4.4**.

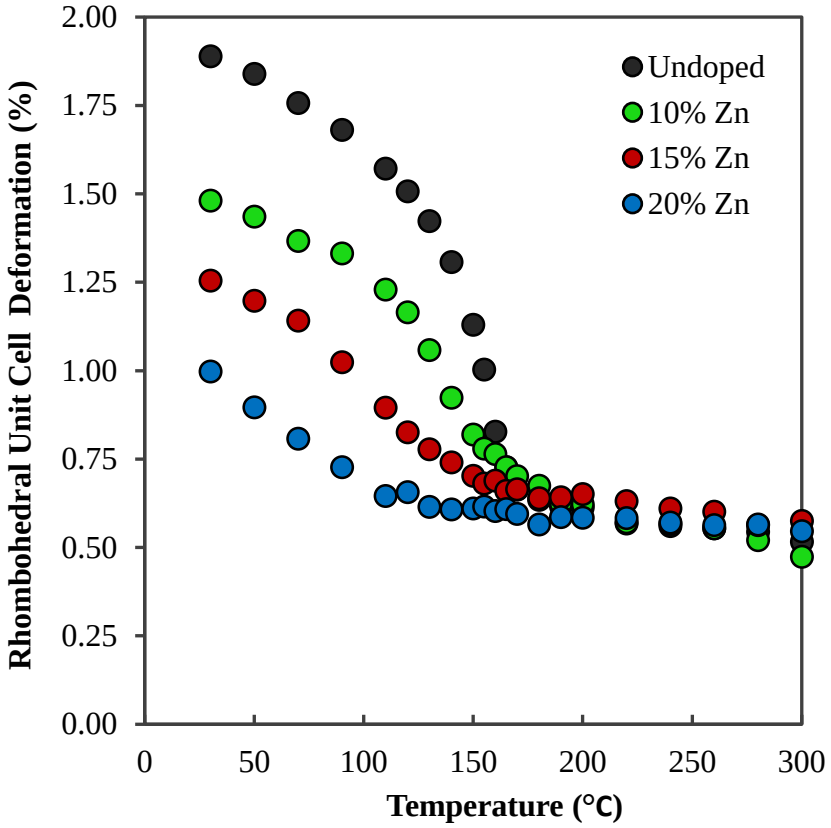


**Fig. 4.4.4**. Shear deformation of the rhombohedral unit cell of NASICON (Eq. 4.2.2) as function of temperature for multiple Zn-doped samples.

There is a decrease in the distortion of the rhombohedral unit cell as the amount

of cation substitution increases. The 20% Zn doped sample in fact changes very little through the phase transition. The rhombohedral lattice is almost unchanged between 300°C and 25°C. This indicates that although there is a phase change, the low temperate monoclinic phase associated with the 20% Zn-NASICON is almost indistinguishable from the high temperature rhombohedral phase. Since the low temperature phase has higher symmetry, the 20% Zn-doped NASICON has decreased activation energy for the sodium ion conduction.

Finally, because the 20% Zn-doped NASICON exhibited the highest conductivity under normal conditions, the synthesis procedure was tweaked to maximize conductivity. Specifically, the sintering profile was optimized to improve the conductivity. Originally the sintering step for the 20% Zn-doped NASICON was a hold for 12 hours at 1100°C. By lowering the sintering temperature, the sample could be held for an extended time at the maximum temperature to promote necking and densification of grains without volatilizing the phosphorus and sodium. Elevated synthesis temperatures have been shown to cause sodium and phosphorus compounds to volatilize out of solution, which increases the amount of secondary phase formation[82]. The sintering temperature of the Zn-doped NASICON was lowered to 1085°C and the time of sintering was increased to determine the optimum condition. The plot of conductivity vs. sintering time is given in **Fig. 4.4.5**. From the plot of conductivity vs sintering time, a maximum in both bulk and total conductivity occurred at a sintering time of 15 hours. The improvement in bulk conductivity is most likely a result of improved density. If there are large pores in the pellets for example, the resulting area of the actual sample will be less than measured. The inaccuracy in

measurement will decrease bulk conductivity since the true smaller area would produce a lower conductivity as detailed by Eq. 2.5.4.

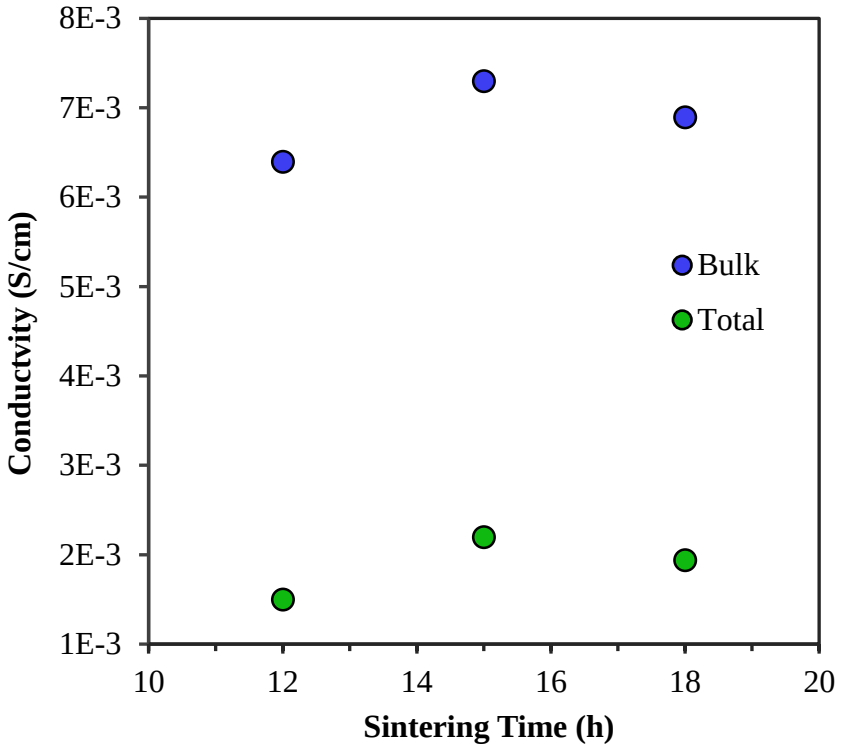


**Fig. 4.4.5**. Room temperature conductivity of 20% Zn-doped NASICON as a function of sintering time. Both the measured bulk conductivity and total conductivity are listed for the sample. The sintering temperature for the 12 hour hold is 1100°C, while the 15 and 18 hour hold occurred at 1085°C.

The increase in total conductivity is likely a result of the improved necking between grains, thus lowering the grain boundary resistance. Ultimately the 20% Zn-doped NASICON sample sintered for 15 hours at 1085°C exhibited the highest conductivity. In fact, the conductivity of the 20% Zn-doped NASICON sample was among the highest reported sodium ion conductivity of any solid state material to date. The bulk conductivity even rivaled that of liquid electrolytes. To illustrate its superior conductivity, the 20% Zn-doped NASICON is compared to other sodium ion

conductors in **Fig. 4.4.6**.

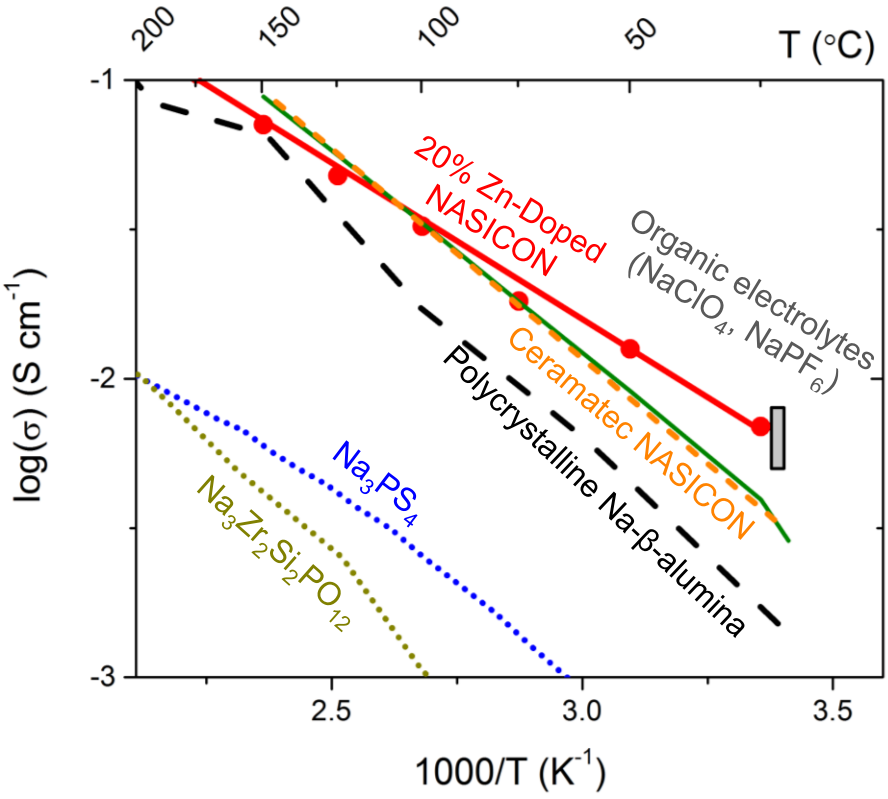


**Fig. 4.4.6**. Conductivity vs. temperature of multiple sodium ion conductors. The bulk conductivity of 20% Zn-doped NASICON is plotted here. Adapted from[15].

Overall the bulk conductivity of 20% Zn-doped NASICON is among the highest ever reported. The increased sodium concentration and decreased Coulombic repulsion helped increase the sodium ion transport. Furthermore, the aliovalent substitution caused higher phase stability of the symmetric rhombohedral phase, which lead to a decrease in activation energy and an improvement in room temperature conductivity. Finally, the optimization of the sintering profile provided better density and less volatility to benefit both the bulk and total conductivity.

# Chapter 5: Electrochemical Cell Development and Testing

## 5.1 Composite Cathodes and Bilayer SOFCs Using $Bi_2O_3$

Since the rhombohedral bismuth oxide sample exhibited a high and stable conductivity, it was important to test how the material behaved in an SOFC. As detailed earlier, a bilayer electrolyte design must be employed with $Bi_2O_3$ electrolyte. The second electrolyte layer effectively protects the bismuth oxide layer from decomposing in the extremely reducing conditions of the hydrogen fuel. Not only must a bilayer design be utilized with a $Bi_2O_3$ electrolyte, but a high functioning cathode that is unreactive with bismuth oxide is also essential. It was found that a mixture of the ion conducting cubic bismuth oxide material ESB and the electronically conducting $La_{0.8}Sr_{0.2}MnO_3$ (LSM) created a highly functional composite cathode[4,83,84]. Since LSM-ESB made an effective composite cathode, the rhombohedral La and Y double doped $Bi_2O_3$ material was also investigated.

The La5.1Y1.4 electrolyte exhibited the highest conductivity of any stable rhombohedral sample tested, so it was used in the composite cathode design. Initially symmetric cells with a La5.1Y1.4 electrolyte and a cathode comprised of a 1:1 volume ratio of La5.1Y1.4 and LSM was deposited on both faces of the cell. The EIS behavior of the symmetric cell was investigated at 500°C in air. The EIS behavior of the La5.1Y1.4 symmetric cell after 5 hours of aging at 500°C and 120 hours of aging at 500°C is given in Fig. 5.1.1.

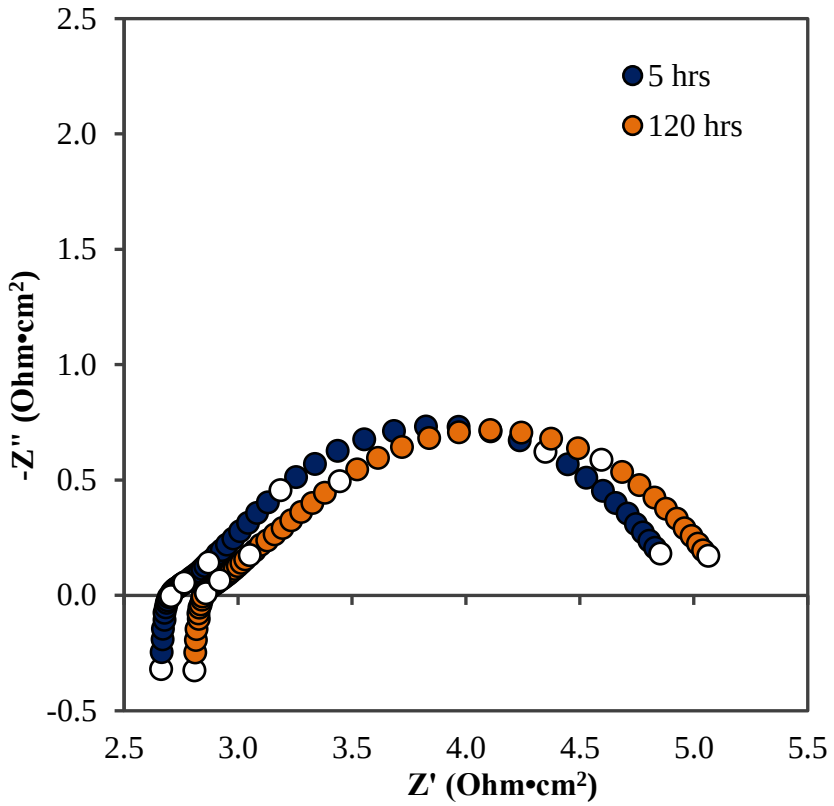


**Fig. 5.1.1**. EIS plot of the La5.1Y1.4 symmetric cell at 500°C. The symmetric cell is comprised of a La5.1Y1.4 electrolyte and a composite cathode with 1:1 volume ratio of La5.1Y1.4 to LSM. The blue curve is after aging for 5 hours 500°C while the orange curve is after 120 hours at 500°C. The white open circles signify every magnitude of frequency from $10^5$ Hz to $10^{-1}$ Hz.

After the EIS curves were recorded, the Z-view software was used to fit the data and analyze the curves. The low frequency arcs are attributed to the cathode response, and thus this portion of the plot was used to quantify the ASR of the composite cathode. The ASR of the La5.1Y1.4-LSM composite cathode as a function of aging time at 500°C is plotted in **Fig. 5.1.2a**. The ASR is compared to an LSM-ESB composite cathode at the same conditions. Furthermore, the calculated cathode degradation as a function of aging time at 500°C is plotted in Fig. **5.1.2b**.

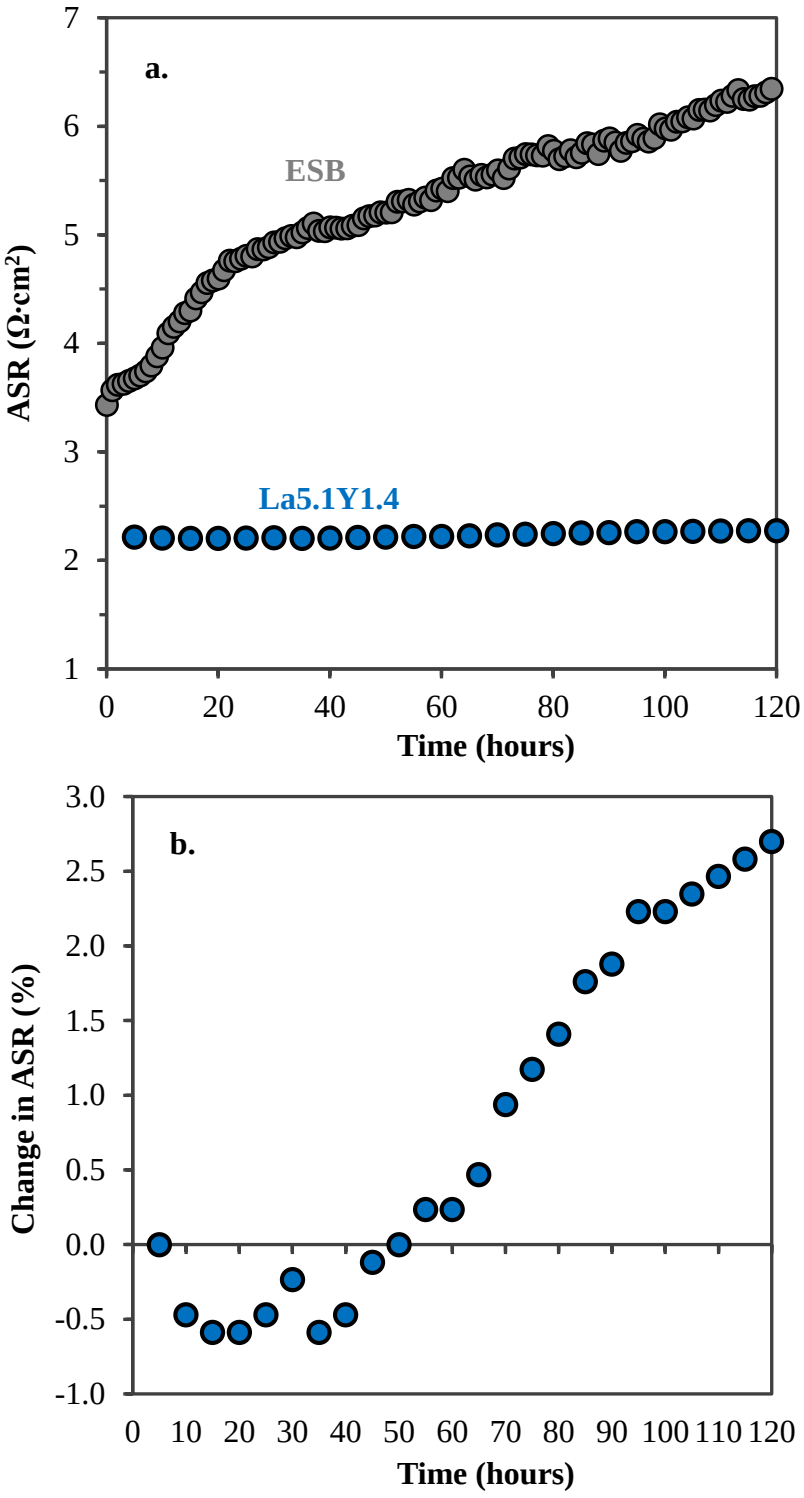


**Fig. 5.1.2 a**. ASR of a La5.1Y1.4-LSM cathode and an ESB-LSM cathode as a function of aging time at 500°C on a symmetric cell. Both bismuth oxide portions were synthesized by a standard solid state route. **b**. The total change in ASR of the La5.1Y1.4-LSM cathode as a function of aging time at 500°C.

It can be observed that there is some degradation of the La5.1Y1.4-LSM cathodic ASR over the entire 120 hour aging time at 500°C, but it is much less than the ESB-LSM cathode. The ESB undergoes an ordering process below 600°C that causes a drop in its ionic conductivity that also affects the mechanics of an ESB-LSM composite cathode. Since the ion conducting portion of the ESB-LSM composite cathode undergoes a severe drop in oxygen transport, there is consequently less incorporation into the lattice. The decrease of the oxygen reduction reactions on the ESB-LSM cathode results in an increase in ASR. The La5.1Y1.4 electrolyte meanwhile does not undergo an ordering phenomenon. Thus, the La5.1Y1.4-LSM cathode does not undergo the same degradation mechanism as the ESB-LSM cathode and is much more stable. The degradation of ASR in the La5.1Y1.4-LSM cathode is most likely a result of grain coarsening. As the grains grow in size, the total area triple of the phase boundary shrinks. The reduction in active sites at the triple phase boundary will therefore cause a decrease in ASR. Since the ASR is relatively low at 500°C and the degradation is slight, the La5.1Y1.4-LSM is a good candidate for an SOFC cathode.

While the initial performance of the La5.1Y1.4-LSM cathode was sufficient for use in an SOFC, the system was optimized to improve ASR. First, the ratio of La5.1Y1.4 to LSM was optimized. The cathodic ASR at 500°C vs. the amount of La5.1Y1.4 to LSM in the cathode is plotted in **Fig. 5.1.3a**. Additionally the sintering profile of the composite cathode was optimized. The ASR of the La5.1Y1.4-LSM cathode as a function of aging time for multiple sintering profiles is plotted in **Fig. 5.1.3b**.

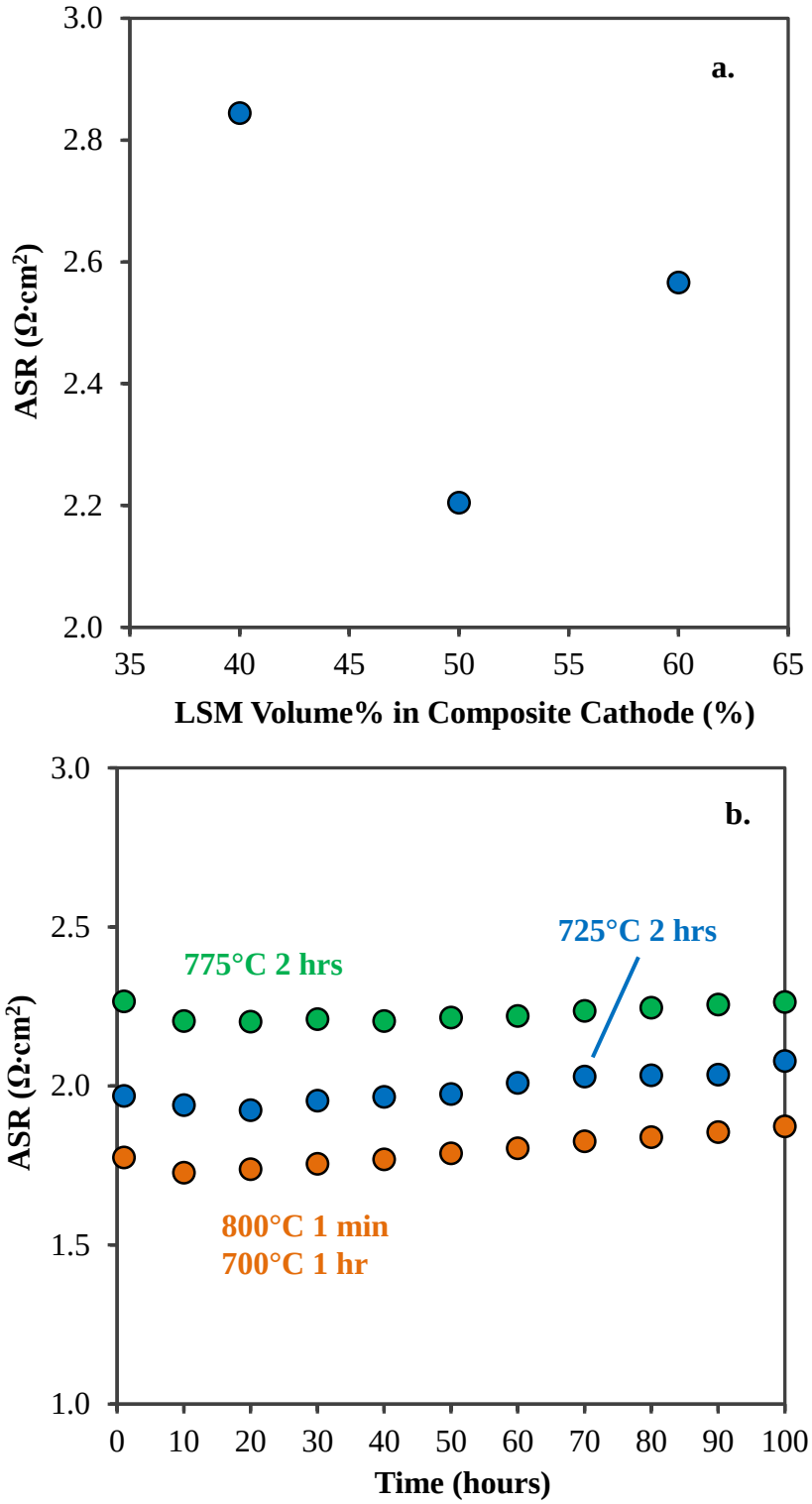


**Fig. 5.1.3a**. ASR of a La5.1Y1.4-LSM composite cathode at 500°C as a function of the volume% of LSM in the cathode. **b**. ASR of the La5.1Y1.4-LSM cathode as a function of aging time at 500°C. The sintering temperature and hold time is labeled on the plot.

It was clear that a 1:1 volume ratio of LSM to La5.1Y1.4 generated the highest functioning cathode. The volume was calculated based upon density and weight of the material. A 1:1 ratio produced the best performance because of the balance between the rhombohedral bismuth oxide that conducted the oxygen ions to the electrolyte and the LSM that catalyzed the reduction of gaseous oxygen. Additionally, the two step sintering profile caused the highest performance boost in cathodic ASR due to decreased coarsening of the grains. A quick ramp to 800°C followed by a one hour hold at 700°C allowed necking between the cathode and electrolyte, while also minimizing grain growth which helped to maximize the catalytic area. The microstructure of the symmetric cell is illustrated in **Fig. 5.1.4**.

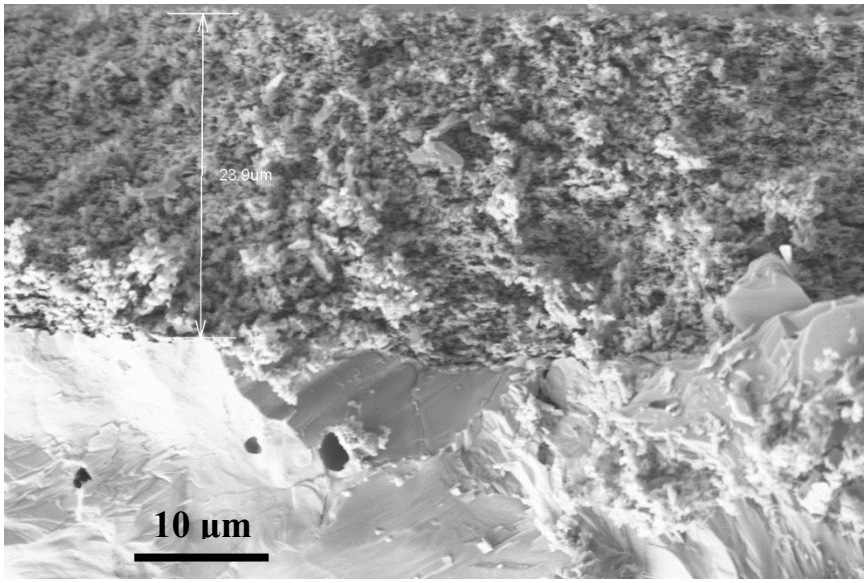


**Fig. 5.1.4**. SEM image of the La5.1Y1.4 symmetric cell. The bottom portion shows the La5.1Y1.4 electrolyte and the top half is the La5.1Y1.4-LSM composite cathode.

Overall the SEM image of the symmetric cell demonstrated that a two-step firing process was sufficient for generating the appropriate microstructure. The electrolyte portion of the symmetric cell was relatively dense, while the cathode side

was generally porous. Overall the solid state synthesis route provided adequate microstructure for testing the La5.1Y1.4 in a symmetric cell, but was not ideal for maximizing performance. Although the particle size for the cathode is submicron, it could be decreased even further. By employing a wet chemical synthesis detailed by other authors it is possible to achieve even better performance in a $Bi_2O_3$ and LSM composite cathode[4,84].

Since the cathode exhibited good, stable performance in a symmetric cell, it was moved up to a full SOFC button cell. The SOFC cell was comprised of a Ni-GDC anode, a 20-micron thick GDC electrolyte, as well as a thin La5.1Y1.4 electrolyte and finally a La5.1Y1.4-LSM cathode. Normally an SOFC with a Ni-GDC anode is taken to high temperature to reduce the cell. Unfortunately, temperatures above approximately 575°C caused a phase change in the rhombohedral bismuth oxide electrolyte as detailed by high temperature XRD. Therefore, to maintain the highly conductive and stable rhombohedral phase, it was important to reduce the cell at lower temperatures. To determine the effect of the phase change on the performance of the bilayer cell, one button cell was reduced at the typical 650°C, while the other was reduced at 550°C. From **Fig. 5.1.5a.** and **5.1.5b.** it is clear that taking the cell up to 650°C was detrimental to the performance when compare to the cell that was taken to 550°C. The button cell reduced at 550°C exhibited a very stable open circuit voltage and max power density. The steady performance of the SOFC is due in large part to the stable ohmic resistance of the rhombohedral electrolyte and the stable non-ohmic resistance of the composite cathode.

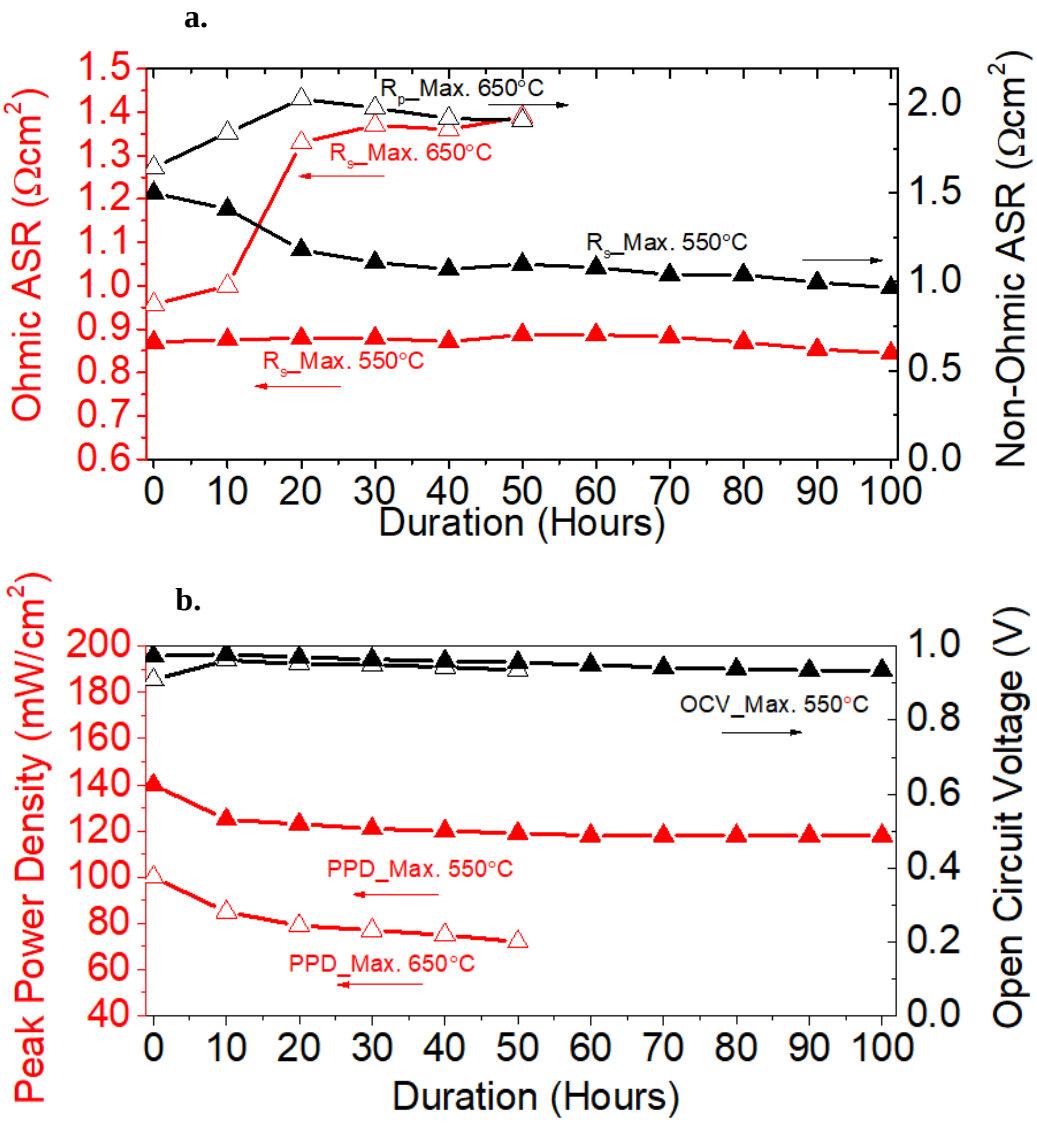


**Fig. 5.1.5** a. Ohmic (red) and non-ohmic (black) ASR as a function of aging time at 500°C. b. Peak power density (red) and open circuit voltage (black) as a function of aging time at 500°C. All metrics relate to an SOFC button cell with a bilayer design. The SOFC has a La5.1Y1.4 electrolyte and a La5.1Y1.4BO-LSM composite cathode. In all cases open triangle symbols signify a cell reduced at 650°C while closed symbols represent a cell reduced at 550°C.

Clearly the stable ionic conductivity of La5.1Y1.4 electrolyte and the stable ASR of the La5.1Y1.4-LSM cathode translated to a stable performing SOFC. To obtain stable performance, the maximum temperature of operation needed to be held below

the phase transition of the rhombohedral phase (~580°C). Above the phase transition temperature, there is a degradation of ionic conductivity in the bismuth oxide, causing a decay in the SOFC performance. Overall the max power density measured in this cell was comparable to other bismuth oxide based bilayer SOFCs at low temperatures[83]. The one distinct advantage that the rhombohedral phase had over the cubic phase though, is that it created a much more stable bilayer cell. The stable performance of the rhombohedral bilayer SOFC is ultimately what makes it suitable for low temperature operation. Although it has high stability, the performance of the rhombohedral bilayer cell could be improved even further by optimizing procedures such as decreasing the thickness of the GDC layer, improving the microstructure of the cathode, and ensuring complete reduction of the anode.

### *5.2 Fabricating a NASICON Scaffold for a Solid State Sodium Battery*

After optimization of the sintering profile, 20% Zn-doped NASICON exhibited both the highest bulk conductivity and total conductivity of any NASICON sample investigated. Thus it was the 20% Zn-doped NASICON that was chosen as the blueprint for an all-solid-state battery. The scaffold for the battery was fabricated using a tape casting method and the design was based on three-dimensional solid electrolyte triple layer demonstrated by others[85,86]. The triple layer is comprised entirely of NASICON with a thick porous layer, a thin dense layer, followed by another thick porous layer. The thick porous layers acts as mechanical support for the scaffold as well as the site for high loading of the cathode and sodium anode. The high porosity ensured more surface area for the cathode and anode layer, thus ensuring greater power density. The thin, dense middle layer acted as the ion conducting electrolyte. The

electrolyte layer was dense to block dendrite formation and shorting, while also being thin to decrease ohmic resistance. An SEM image of the 20% Zn-doped NASICON triple layer is given in **Fig. 5.2.1**.

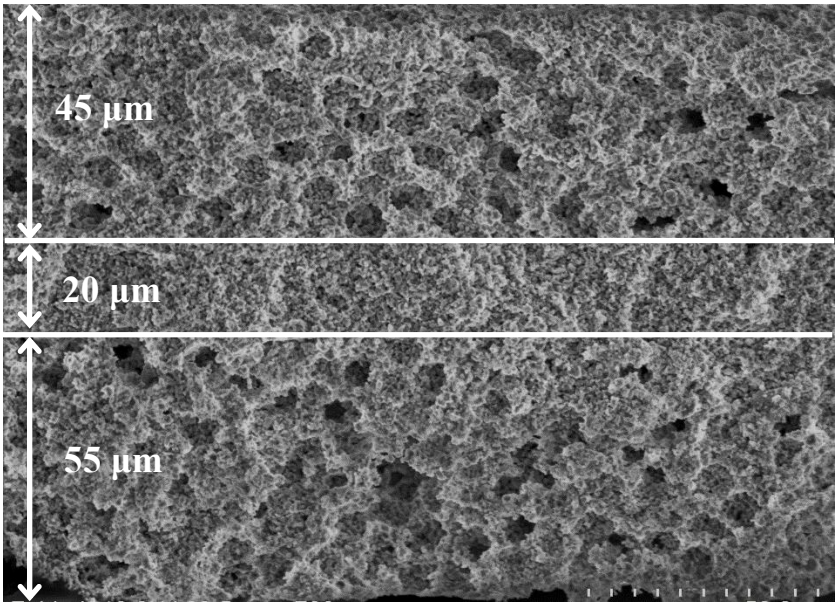


**Fig. 5.2.1**. SEM image of the 20% Zn-doped NASICON triple layer. The thickness of each layer is indicated.

While the three layers of the scaffold are distinct, the structure could still be improved. The middle layer should be denser, and the porous layer should have greater connectivity between grains. Improving the recipe for the tape casting, as well as optimizing the sintering temperature should be investigated further. Nevertheless, the 20 µm dense layer of 20% Zn-doped NASICON would provide very good ohmic ASR for a full cell. The EIS comparison of 20% Zn-doped NASICON vs undoped NASICON at 25°C is provided in **Fig. 5.2.2 a**. The resistance was extracted from the plots and used to project the ASR of a full cell with a 20 micron thick NASICON electrolyte. The extrapolation of ohmic ASR is plotted in **Fig. 5.2.2 b**.

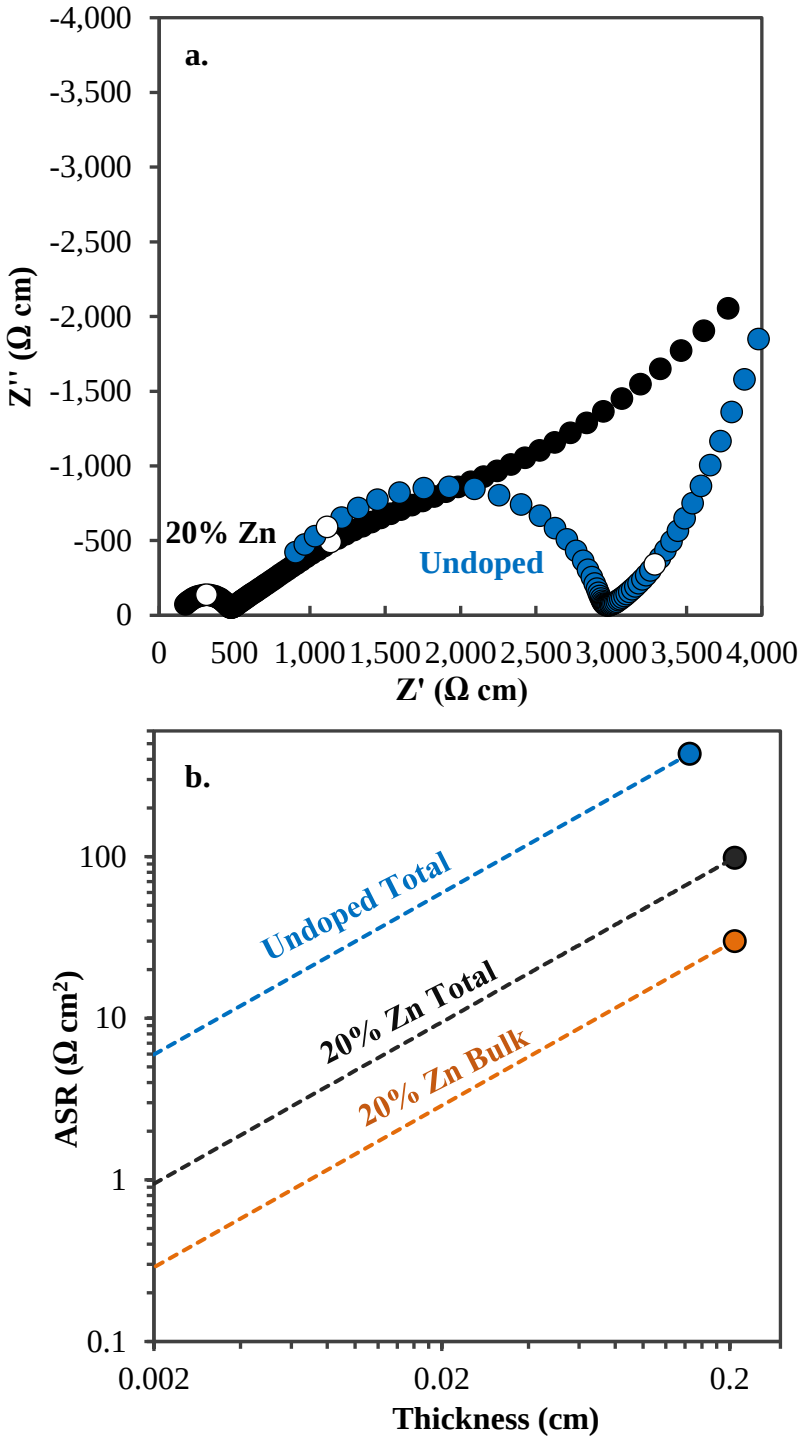


**Fig. 5.2.2 a.** Nyquist plot of 20% Zn-doped NASICON and undoped NASICON measured at room temperature. The first open circle on the plot represents a frequency of 1 MHz and the second open circle is 100 Hz. **b.** The ASR of 20% Zn-doped NASICON and undoped NASICON determined by EIS fitting. The dotted line represents the projection of the ASR down to a nominal thickness of a 20 μm electrolyte layer in a full cell. Total describes the total ASR and bulk describes the bulk ASR.

Overall the 20% Zn-doped NASICON makes a good scaffold for a solid state battery and would have much better performance than the undoped NASICON. The figure illustrates that a cell with a 20 μm thick electrolyte layer would have a total ASR less than 1 Ω $cm^2$. With further tuning, the grain boundary resistance of the 20% Zn-doped NASICON can be negated allowing for a theoretical ASR of the cell to decrease all the way to approximately 0.3 Ω $cm^2$. Unfortunately no symmetric cell or full cell data is presented because further work is required to infiltrate the sodium into the scaffold. Other authors have presented methods for minimizing interfacial resistance when incorporating a metal anode onto a solid electrolyte and these could be explored[87,88]. Ultimately the 20% Zn-doped NASICON and other aliovalent doped NASICON are worth pursuing to create a high performance solid state sodium battery.

# Bibliography


1. Boyapati, S., Wachsman, E. D. & Jiang, N. Effect of oxygen sublattice ordering on interstitial transport mechanism and conductivity activation energies in phase-stabilized cubic bismuth oxides. *Solid State Ionics* **140,** 149–160 (2001).
2. Irvine, J. T. S., Sinclair, D. C. & West, A. R. Electroceramics: Characterization by Impedance Spectroscopy. *Adv. Mater.* **2,** 132–138 (1990).
3. Sammes, N. M., Tompsett, G. A., Näfe, H. & Aldinger, F. Bismuth based oxide electrolytes— structure and ionic conductivity. *J. Eur. Ceram. Soc.* **19,** 1801–1826 (1999).
4. Lee, K. T. *et al.* Highly functional nano-scale stabilized bismuth oxides via reverse strike co-precipitation for solid oxide fuel cells. *J. Mater. Chem. A* **1,** 6199 (2013).
5. Verkerk, M. J. & Burggraaf, A. J. High Oxygen Ion Conduction in Sintered Oxides of the Bi[sub 2]O[sub 3]-Dy[sub 2]O[sub 3] System. *J. Electrochem. Soc.* **128,** 75 (1981).
6. Verkerk, M. J. & Burggraaf, A. J. High Oxygen Ion Conduction in Sintered Oxides. *Solid State Ionics* **3–4,** (1981).
7. Lee, K. T., Yoon, H. S. & Wachsman, E. D. The evolution of low temperature solid oxide fuel cells. *J. Mater. Res.* **27,** 2063–2078 (2012).
8. Jung, D. W., Duncan, K. L. & Wachsman, E. D. Effect of total dopant concentration and dopant ratio on conductivity of (DyO1.5)x–(WO3)y–(BiO1.5)1−x−y. *Acta Mater.* **58,** 355–363 (2010).
9. Aidhy, D. S., Sinnott, S. B., Wachsman, E. D. & Phillpot, S. R. Effect of ionic polarizability on oxygen diffusion in δ-Bi2O3 from atomistic simulation. *Ionics (Kiel).* **16,** 297–303 (2010).
10. Wachsman, E. D. & Lee, K. T. Lowering the Temperature of Solid Oxide Fuel Cells. *Science (80-. ).* **334,** 935–939 (2011).
11. Hueso, K. B., Armand, M. & Rojo, T. High temperature sodium batteries: status, challenges and future trends. *Energy Environ. Sci.* **6,** 734 (2013).
12. Fuentes, R. O., Figueiredo, F. M., Marques, F. M. B. & Franco, J. I. Processing and electrical properties of NASICON prepared from yttria-doped zirconia precursors. *J. Eur. Ceram. Soc.* **21,** 737–743 (2001).
13. Bukun, N. G. Superionic transitions in NASICON-type solid electrolytes. *Ionics (Kiel).* **2,** 63–68 (1996).
14. Jung, D. W. *et al.* Effect of Annealing Temperature and Dopant Concentration on the Conductivity Behavior in $(DyO_{1.5})_x$-$(WO_3)_y$-$(BiO_{1.5})_{1-x-y}$. *J. Am. Ceram. Soc.* **93,** 1384–1391 (2010).
15. Hayashi, A., Noi, K., Sakuda, A. & Tatsumisago, M. Superionic glass-ceramic electrolytes for room-temperature rechargeable sodium batteries. *Nat. Commun.* **3,** 856 (2012).
16. Yamamoto, O. Solid oxide fuel cells: fundamental aspects and prospects. *Electrochim. Acta* **45,** 2423–2435 (2000).
17. Stambouli, A. B. & Traversa, E. Solid oxide fuel cells (SOFCs): A review of an environmentally clean and efficient source of energy. *Renew. Sustain.*

*Energy Rev.* **6,** 433–455 (2002).
18. Steele, B. C. H. & Heinzel, A. Materials for fuel-cell technologies. *Nature* **414,** 345–352 (2001).
19. Bo, C., Yuan, C., Zhao, X., Wu, C.-B. & Li, M.-Q. Parametric analysis of solid oxide fuel cell. *Clean Technol. Environ. Policy* **11,** 391–399 (2009).
20. Chan, S. H., Low, C. F. & Ding, O. L. Energy and exergy analysis of simple solid-oxide fuel-cell power systems. *J. Power Sources* **103,** 188–200 (2002).
21. Brett, D. J. L., Atkinson, A., Brandon, N. P. & Skinner, S. J. Intermediate temperature solid oxide fuel cells. *Chem. Soc. Rev.* **37,** 1568 (2008).
22. Zhu, W. Z. & Deevi, S. C. Development of interconnect materials for solid oxide fuel cells. *Mater. Sci. Eng. A* **348,** 227–243 (2003).
23. Skinner, S. J. & Kilner, J. A. Oxygen ion conductors. *Mater. Today* **6,** 30–37 (2003).
24. Hideaki Inaba, H. T. Ceria-based solid electrolytes. *Solid State Ionics* **2738,** 1–16 (1996).
25. Arachi, Y., Sakai, H., Yamamoto, O., Takeda, Y. & Imanishai, N. Electrical conductivity of the ZrO2-Ln2O3 (Ln=lanthanides) system. *Solid State Ionics* **121,** 133–139 (1999).
26. Harwig, H. A. & Gerards, A. G. Electrical properties of the α, β, γ, and δ phases of bismuth sesquioxide. *J. Solid State Chem.* **26,** 265–274 (1978).
27. Takahashi, T., Iwahara, H. & Arao, T. High oxide ion conduction in sintered oxides of the system Bi2O3-Y2O3. *J. Appl. Electrochem.* **5,** 187–195 (1975).
28. Jiang, N., Wachsman, E. D. & Jung, H. S. A higher conductivity Bi2O3-based electrolyte. *Solid State Ionics* **150,** 347–353 (2002).
29. Fung, K. Z., Chen, J. & Virkar, A. V. Effect of Aliovalent Dopants on the Kinetics of Phase Transformation and Ordering in RE2O3-Bi2O3 (RE = Yb, Er, Y, or Dy) Solid Solutions. *J. Am. Ceram. Soc.* **76,** 2403–2418 (1993).
30. Joshi, A. V. *et al.* Phase stability and oxygen transport characteristics of yttria- and niobia-stabilized bismuth oxide. *J. Mater. Sci.* **25,** 1237–1245 (1990).
31. Wachsman, E. D., Boyapati, S. & Jiang, N. Effect of dopant polarizability on oxygen sublattice order in phase-stabilized cubic bismuth oxides. *Ionics (Kiel).* **7,** 1–6 (2001).
32. Jiang, N. *et al.* Anion ordering in aged stabilized bismuth oxide. *Mater. Lett.* **22,** 215–219 (1995).
33. Drache, M., Obbade, S., Wignacourt, J. P. & Conflant, P. Structural and Conductivity Properties of Bi0.775Ln0.225O1.5Oxide Conductors (Ln=La, Pr, Nd, Sm, Eu, Gd, Tb, Dy) with Rhombohedral Bi–Sr–O Type. *J. Solid State Chem.* **142,** 349–359 (1999).
34. Iwahara, H., Esaka, T., Sato, T. & Takahashi, T. Formation of high oxide ion conductive phases in the sintered oxides of the system Bi2O3Ln2O3 (Ln = LaYb). *J. Solid State Chem.* **39,** 173–180 (1981).
35. Takahashi, T., Iwahara, H. & Nagai, Y. High oxide ion conduction in sintered Bi2O3 containing SrO, CaO or La2O3. *J. Appl. Electrochem.* **2,** 97–104 (1972).
36. Jiang, N. & Wachsman, E. D. Structural Stability and Conductivity of Phase-Stabilized Cubic Bismuth Oxides. *J. Am. Ceram. Soc.* **82,** 3057–3064 (2004).

37. Ahn, J. S. *et al.* High-performance bilayered electrolyte intermediate temperature solid oxide fuel cells. *Electrochem. commun.* **11,** 1504–1507 (2009).
38. Takahashi, T., Esaka, T. & Iwahara, H. Conduction in Bi2O3-based oxide ion conductors under low oxygen pressure. I. Current blackening of the Bi2O3-Y2O3 electrolyte. *J. Appl. Electrochem.* **7,** 299–302 (1977).
39. Wachsman, E. D., Ball, G. R., Jiang, N. & Stevenson, D. A. Structural and defect studies in solid oxide electrolytes. *Solid State Ionics* **52,** 213–218 (1992).
40. Joh, D. W., Park, J. H., Kim, D., Wachsman, E. D. & Lee, K. T. Functionally Graded Bismuth Oxide/Zirconia Bilayer Electrolytes for High-Performance Intermediate-Temperature Solid Oxide Fuel Cells (IT-SOFCs). *ACS Appl. Mater. Interfaces* **9,** 8443–8449 (2017).
41. Park, J. Y., Yoon, H. & Wachsman, E. D. Fabrication and characterization of high-conductivity bilayer electrolytes for intermediate-temperature solid oxide fuel cells. *J. Am. Ceram. Soc.* **88,** 2402–2408 (2005).
42. Dunn, B., Kamath, H. & Tarascon, J.-M. Electrical Energy Storage for the Grid: A Battery of Choices. *Science (80-. ).* **334,** 928–935 (2011).
43. Yang, Z. *et al.* Electrochemical energy storage for green grid. *Chem. Rev.* **111,** 3577–3613 (2011).
44. Palomares, V. *et al.* Na-ion batteries, recent advances and present challenges to become low cost energy storage systems. *Energy Environ. Sci.* **5,** 5884 (2012).
45. Yabuuchi, N. *et al.* P2-type Nax[Fe1/2Mn1/2]O2 made from earth-abundant elements for rechargeable Na batteries. *Nat. Mater.* **11,** 512–517 (2012).
46. Slater, M. D., Kim, D., Lee, E. & Johnson, C. S. Sodium-ion batteries. *Adv. Funct. Mater.* **23,** 947–958 (2013).
47. Lalère, F. *et al.* An all-solid state NASICON sodium battery operating at 200??C. *J. Power Sources* **247,** 975–980 (2014).
48. Noguchi, Y., Kobayashi, E., Plashnitsa, L. S., Okada, S. & Yamaki, J. I. Fabrication and performances of all solid-state symmetric sodium battery based on NASICON-related compounds. *Electrochim. Acta* **101,** 59–65 (2013).
49. Park, C.-W., Ahn, J.-H., Ryu, H.-S., Kim, K.-W. & Ahn, H.-J. Room-Temperature Solid-State Sodium⁄Sulfur Battery. *Electrochem. Solid-State Lett.* **9,** A123 (2006).
50. Song, S., Duong, H. M., Korsunsky, A. M., Hu, N. & Lu, L. A Na+ Superionic Conductor for Room-Temperature Sodium Batteries. *Sci. Rep.* **6,** 32330 (2016).
51. Wang, A. *et al.* Processable and Moldable Sodium Metal Anodes. *Angew. Chemie Int. Ed.* **56,** 11921–11926 (2017).
52. Gao, R. *et al.* Nanofiber networks of $Na_3V_2(PO_4)_3$ as a cathode material for high performance all-solid-state sodium-ion batteries. *J. Mater. Chem. A* **5,** 5273–5277 (2017).
53. Bhide, A. & Hariharan, K. Physicochemical properties of NaxCoO2 as a cathode for solid state sodium battery. *Solid State Ionics* **192,** 360–363 (2011).
54. Perthuis, H. & Colomban, P. Well densified nasicon type ceramics, elaborated using sol-gel process and sintering at low temperatures. *Mater. Res. Bull.* **19,**

621–631 (1984).
55. Shimizu, Y., Azuma, Y. & Michishita, S. Sol–gel synthesis of NASICON discs from aqueous solution. *J. Mater. Chem.* **7,** 1457–1460 (1997).
56. Park, H., Jung, K., Nezafati, M., Kim, C. S. & Kang, B. Sodium Ion Diffusion in Nasicon (Na3Zr2Si2PO12) Solid Electrolytes: Effects of Excess Sodium. *ACS Appl. Mater. Interfaces* **8,** 27814–27824 (2016).
57. Fergus, J. W. Ion transport in sodium ion conducting solid electrolytes. *Solid State Ionics* **227,** 102–112 (2012).
58. Wen, Z., Hu, Y., Wu, X., Han, J. & Gu, Z. Main challenges for high performance NAS battery: Materials and interfaces. *Adv. Funct. Mater.* **23,** 1005–1018 (2013).
59. Yu, X. & Manthiram, A. Room-temperature sodium-sulfur batteries with liquid-phase sodium polysulfide catholytes and binder-free multiwall carbon nanotube fabric electrodes. *J. Phys. Chem. C* **118,** 22952–22959 (2014).
60. Ponrouch, A. *et al.* Towards high energy density sodium ion batteries through electrolyte optimization. *Energy Environ. Sci.* **6,** 2361 (2013).
61. Goodenough, J. B., Hong, H. Y. P. & Kafalas, J. A. Fast Na+-ion transport in skeleton structures. *Mater. Res. Bull.* **11,** 203–220 (1976).
62. Hong, H. Y. P. Crystal structures and crystal chemistry in the system Na1+xZr2SixP3-xO12. *Mater. Res. Bull.* **11,** 173–182 (1976).
63. Boilot, J. P., Collin, G. & Colomban, P. Relation structure-fast ion conduction in the NASICON solid solution. *J. Solid State Chem.* **73,** 160–171 (1988).
64. Fuentes, R., Figueiredo, F. M., Marques, F. M. B. & Franco, J. I. Influence of microstructure on the electrical properties of NASICON materials. *Solid State Ionics* **140,** 173–179 (2001).
65. Saito, Y., Ado, K., Asai, T., Kageyama, H. & Nakamura, O. Ionic conductivity of NASICON-type conductors Na1.5M0.5Zr1.5(PO4)3 (M:Al3+, Ga3+, Cr3+, Sc3+, Fe3+, In3+, Yb3+, Y3+). *Solid State Ionics* **58,** 327–331 (1992).
66. Miyajima, Y., Saito, Y., Matsuoka, M. & Yamamoto, Y. Ionic conductivity of NASICON-type Na1+xMxZr2-xP3O12 (M: Yb, Er, Dy). *Solid State Ionics* **84,** 61–64 (1996).
67. Cava, R. J., Vogel, E. M. & Johnson, D. W. Effect of Homovalent Framework Cation Substitutions on the Sodium Ion Conductivity in Na3Zr2Si2PO12. *J. Am. Ceram. Soc.* **65,** c157–c159 (1982).
68. Takahashi, T., Kuwabara, K. & Shibata, M. Solid-state ionics - conductivities of Na+ ion conductors based on NASICON. *Solid State Ionics* **1,** 163–175 (1980).
69. Park, H., Jung, K., Nezafati, M., Kim, C. S. & Kang, B. Sodium Ion Diffusion in Nasicon (Na3Zr2Si2PO12) Solid Electrolytes: Effects of Excess Sodium. *ACS Appl. Mater. Interfaces* **8,** 27814–27824 (2016).
70. Alpen, U., Bell, M. & Wichelhaus, W. Phase-Transition in Nasicon (Na3Zr2Si2Po12). *Mater. Res. Bull.* **14,** 1317–1322 (1979).
71. Boilot, J. P., Collin, G. & Colomban, P. Relation structure-fast ion conduction in the NASICON solid solution. *J. Solid State Chem.* **73,** 160–171 (1988).
72. Colomban, P. & Mouchon, E. Phase transition in, thermal history and expansion of NASICON, solid solution and lithium derivative ceramics and of

SiC (mullite) fibers-NASICON composites. *Solid State Ionics* **73,** 209–220 (1994).
73. Wachsman, E. D. & Lee, K. T. Lowering the Temperature of Solid Oxide Fuel Cells. *Science (80-. ).* **334,** (2011).
74. Jiang, N., Wachsman, E. D. & Jung, S. H. A higher conductivity Bi2O3-based electrolyte. *Solid State Ionics* **150,** 347–353 (2002).
75. Fung, K. Z., Chen, J. & Virkar, A. V. Effect of Aliovalent Dopants on the Kinetics of Phase Transformation and Ordering in RE2O3-Bi2O3 (RE = Yb, Er, Y, or Dy) Solid Solutions. *J. Am. Ceram. Soc.* **76,** 2403–2418 (1993).
76. Wang, S., Wu, L., Gao, J., He, Q. & Liu, M. Oxygen ion transference number of doped lanthanum gallate. *J. Power Sources* **185,** 917–921 (2008).
77. Gasmi, N. *et al.* Comparison of different synthesis methods for nasicon ceramics. *J. Sol-Gel Sci. Technol.* **4,** 231–237 (1995).
78. Lloyd, I. K., Gupta, T. K. & Hall, B. O. Sintering and characterization of alkaline-earth-doped and zirconium-defficient Na3Zr2Si2PO12. *Solid State Ionics* **11,** 39–44 (1983).
79. Colomban, P. Orientational disorder, glass/crystal transition and superionic conductivity in nasicon. *Solid State Ionics* **21,** 97–115 (1986).
80. Bohnke, O., Ronchetti, S. & Mazza, D. Conductivity measurements on nasicon and nasicon-modified materials. *Solid State Ionics* **122,** 127–136 (1999).
81. Jamnik, J. & Maier, J. Generalised equivalent circuits for mass and charge transport: chemical capacitance and its implications. *Phys. Chem. Chem. Phys.* **3,** 1668–1678 (2001).
82. Bell, N. S., Edney, C., Wheeler, J. S., Ingersoll, D. & Spoerke, E. D. The influences of excess sodium on low-temperature NaSICON synthesis. *J. Am. Ceram. Soc.* **97,** 3744–3748 (2014).
83. Zhang, Q. S., Hirano, A., Imanishi, N., Takeda, Y. & Yamahara, K. LSM Cathodes Infiltrated With Er[sub 2]O[sub 3] Stabilized Bi[sub 2]O[sub 3]. *J. Fuel Cell Sci. Technol.* **6,** 11001 (2009).
84. Lee, K. T., Lidie, A. A., Yoon, H. S. & Wachsman, E. D. Rational design of lower-temperature solid oxide fuel cell cathodes via nanotailoring of co-assembled composite structures. *Angew. Chemie - Int. Ed.* **53,** 13463–13467 (2014).
85. Xu, S., McOwen, D. W., Wachsman, E. D. & Hu, L. Quasi Solid State Li-S Battery Enabled By a Triple Layer Garnet Framework. in (Ecs, 2017). at <https://ecs.confex.com/ecs/232/webprogram/Paper103639.html>
86. Fu, K. (Kelvin) *et al.* Three-dimensional bilayer garnet solid electrolyte based high energy density lithium metal–sulfur batteries. *Energy Environ. Sci.* **10,** 1568–1575 (2017).
87. Han, X. *et al.* Negating interfacial impedance in garnet-based solid-state Li metal batteries. *Nat. Mater.* **16,** 572–579 (2016).
88. Zhou, W., Li, Y., Xin, S. & Goodenough, J. B. Rechargeable Sodium All-Solid-State Battery. *ACS Cent. Sci.* **3,** 52–57 (2017).